Bio-Impedance Spectroscopy Analysis: Measurement and Finite Element Based Cell Modelling

A thesis submitted to The University of Manchester for the degree of

Doctor of Philosophy

in the Faculty of Science and Engineering

2020

By

Jiawei Tang

School of Electrical and Electronic Engineering

The University of Manchester

ABSTRACT

Bio-impedance spectroscopy has been increasingly used for medical and food industrial applications as it provides information about cellular structure, composition and integrity of cell membranes of biological samples.

This study is focused on analysing how bio-impedance spectrum is affected by cellular structure (cell deformation, shape and orientation) and the integrity of cell membranes during the frozen-thaw injury process.

Two measurement systems were designed and built: contact-electrode measurement and non-contact induction measurement system. For the former, the frequency range of measurement is 10 kHz to 10 MHz while the frequency range for the latter is 400 kHz to 6 MHz. Both systems can detect the change in impedance spectrum of biological samples (potato and meat) caused by the poration of the cell membranes during the frozen-thaw injury process.

A finite element method (FEM) simulation solver was built and applied for the simulation of BIS. Specifically, the poration of the cell membrane was simulated and it was proved to cause the increase in equivalent conductivity of the cell membrane and this is in agreement with the experimental observation carried out in this thesis work and previous studies reported in literature. The shape and orientation effect of the cell was also simulated and the results were explained with physical insights.

In addition, a new acceleration method for simulating thin cell membrane based on FEM was proposed and implemented. The modelling method

accelerates the computing progress by reducing the number of meshing elements without reducing the accuracy of the simulation in a significant manner in comparison with analytical solutions. The accuracy of the acceleration modelling (reduced-mesh model) was also validated by the full-meshed FEM model to be within 0.4%-2% while the simulation time was reduced up to 25%.

TABLE OF CONTENTS

Total words: 22385

LIST OF FIGURES

LIST OF TABLES

NOMENCLATURE

Abbreviations and Acronyms

FEM	Finite Element Method
BIS	Bio-Impedance Spectroscopy
AC	Alternating Current
DC	Direct Current
2-D	Two-Dimensional
3-D	Three-Dimensional
DNA	Deoxyribonucleic Acid
PI	Propidium Iodide
PH	Pondus Hydrogenii
ECF	Extracellular Fluid
ICF	Intracellular Fluid

Lists of symbols

$\varepsilon_r(\infty)$	Permittivity at high frequency
$\varepsilon(0)$	Permittivity at a low frequency
ω	Angular velocity
f	Frequency
τ	Relaxation constant
$\mathrm{k_m}$	Conductivity of the cell membrane
$\mathrm{k_a}$	Conductivity of the extracellular fluid

k_c	Conductivity of intracellular fluid
ε_c	Relative permittivity of intracellular fluid
ε_a	Relative permittivity of extracellular fluid
ε_m	Relative permittivity of cell membrane
R	Radius of cell
d_m	Cell membrane thickness
ε_p^*	Complex relative permittivity of cell model
ε_m^*	Complex relative permittivity of membrane
ε_c^*	Complex relative permittivity of cytoplasm
P	Volume fraction
ε^*	Complex relative permittivity of cell suspension
ε_a^*	Complex relative permittivity of external medium
σ_r	Conductivity of cell suspension
ε_r	Permittivity of cell suspension
σ^*	Complex conductivity of cell suspension
ε_0	Permittivity of vacuum
j	Imaginary unit
L	Laplace operator
$\emptyset$	Unknown field function
g	Given exciting function
$\vec{D}$	Electric flux density
$\vec{E}$	Electrical field intensity

$j^{(i)}$	Current density of element on the chosen plane
$\sigma^{(n)}$	Conductivity of element on the chosen plane
$\vec{E}^{(i)}$	Background electrical field on the chosen plane
L_1	Distance between top and bottom electrode
Ω_n	Nonconductive region
Ω_c	Conductive region
H	Magnetic field intensity
B	Magnetic flux density
M_1	Full-mesh model membrane
M_2	Reduced-mesh model membrane
S	Surface area
Z	Impedance
ρ	Resistivity
ΔV	Detected electromotive force from receive coil
V	Excitation from the transmit coil
σ_e^*	Complex conductivity of the equivalent membrane
D	Displacement field
E	Electric field
$\sigma^{(i)}$	Complex conductivity of each tetrahedral element
$\vec{n}_{(i)}$	Current flow direction
I	Current
U	Electrical potential

DECLARATION

No portion of the work referred to in this thesis has been submitted in support of an application for another degree of qualification of this or any other university or other institution of learning.

COPYRIGHT STATEMENT

ACKNOWNLEDGEMENT

I would like to thank my supervisor Dr.Wuliang Yin for his patience, kindness and encouragement. He helped me a lot not only in academics but also guided me in my life during the past four years.

I would like to extend my appreciation to my co-supervisor Anthony Peyton for his advices.

Sincerely thanks to my colleagues and friends for their accompanying and support. Thanks to Dr Michael O'Toole who helped me a lot and gave me critical advices, and Dr.Mingyang Lu for his kind technical support. Thanks to Yuedong Xie, Hanyang Xu, Shupei Wang and Jorge Salas Avila, who helped me a lot in my research life.

Finally, I would like to thank my parents, Mr. Xiangdong Tang and Mrs. Juzhi Tan, for their support and loving encouragement through all these years. And thanks to my beloved wife, Dr. Yuyang Zhou, for her accompany and love, and for giving me great confidence all the time.

PUBLICATIONS

Journal Papers:

1. **Tang J**, Yin W, Lu M. Bio-impedance spectroscopy for frozen-thaw of bio-samples: Non-contact inductive measurement and finite element (FE) based cell modelling. Journal of Food Engineering, 2020, 272: 109784.
2. **Tang J**, Lu M, Xie Y, et al. A novel efficient FEM thin shell model for bio-impedance analysis. Biosensors, 2020, 10: 69.
3. **Tang J**, Lu M, Yin W, et al. Effect of frozen-thaw injury on cell membrane and bio-impedance. IEEE International Instrumentation and Measurement technology Conference, 2020, 1-6.
4. Yin W., **J. Tang**, M. Lu, H. Xu, R. Huang, Q. Zhao, Z. Zhang, and A. Peyton. An equivalent-effect phenomenon in eddy current non-destructive testing of thin structures. IEEE Access, 2019, 7: 70296-70307.
5. Zhao Q, Zhang L, **Tang J**, et al. Numerical modelling of single bubble rising in metal liquid based on electrical field change and boundary element method. Engineering Analysis with Boundary Elements, 2018, 96: 179-186.
6. Yin W, Lu M, **Tang J**, et al. Custom edge-element FEM solver and its application to eddy-current simulation of realistic 2M-element human brain phantom. Bioelectromagnetics, 2018, 39(8): 604-616.

1 Introduction

1.1 Motivation

Biological samples exhibit a frequency dependent impedance spectroscopy which indicates the structural and composition information of the samples [1]. The structural information is mainly contained in β-dispersion, a dispersion of the impedance spectroscopy which operates at a radio frequency ranging from 10 kHz to 10 MHz. Thus, analysing bio-impedance spectroscopy, especially β-dispersion, has been applied in many medical and industrial applications such as food quality inspection [2].

The quality and safety of food have increasingly attracted public concerns and attentions. The quality of food has been highly topical for many years in area of food industries, public debates and researches [3]. Although considerable previous work has been published in measuring and simulating the bio-impedance spectroscopy, there are still significant issues, such as the mechanism of frozen-thawed injury to biological food samples and the corresponding measurement systems and simulation models, which need further research and investigation.

This work is focused on analysing frozen-thaw effect which is considered as one of the most common factors that influence the quality of food including meats, vegetables and fruits. Bio-impedance spectroscopy (BIS) measurement is a fast and effective way to analyse the frozen-thaw effect. Two

different BIS systems, a contact-electrode system and a non-contact induction system, were built to measure the bio-impedance spectroscopy of the frozen-thawed food samples. In addition, a modelling based on finite element method (FEM) is proposed to validate the measurement results.

The conventional FEM modelling is a thin shell bio-cell model which requires a large number of meshing elements and leads to a massive calculation work. In order to simplify the calculation process and reduce the calculation time, a new acceleration method for the thin shell bio-cell model is proposed. This acceleration method is validated by analytical solutions. Further applications on other thin shell models are investigated and designed.

1.2 Aims and objectives

The aims of the study are to produce and analyse BIS of food samples by building measurement systems and modelling methods. The objectives of the study include:

1, To distinguish the frozen-thawed food samples from fresh food samples by analysing bio-impedance spectroscopy. This thesis intends to build up two measurement systems, one contact-electrode system and one non-contact induction system, to measure the BIS of biological food samples.

2, To seek a modelling method for frozen-thawed biological samples based on FEM. The modelling method is used to analyse the mechanism of how

frozen-thaw injury influence the BIS of food samples.

3, To develop an acceleration method for a thin shell cell model based on finite element method. This acceleration method can potentially be applied for other thin shell models.

4, To analyse the influence of the cell structure on the BIS of food samples, including the cell shape deformation, cell membrane thickness and cell orientation.

1.3 Technical difficulties

There are several research problems and technical difficulties to achieve the research aims.

1. A FEM solver based on Matlab code was built to produce the BIS of food samples. It requires a large amount of programming and computational work. In addition, there are challenges on building appropriate FEM model for frozen-thaw effect and deriving a calculation method to obtain the BIS of the designed FEM model.

2. Because the electrical signal detected from the food samples is small, the sensitivity and accuracy requirement for the measurement system are extremely high. The sensor needs to be elaborately designed to meet the sensitivity and accuracy requirement. The measurements need to be

repeated numerous times to eliminate the random error.

3. Designing an entire control-experiment for analysing the frozen-thaw effect requires meticulous works including food preparation, pre-treatment on food, slides preparation and BIS measurement. Every step needs to be rigorously designed and implemented (e.g. temperature and frozen-thaw time control for food preparation, micro-section of food samples, designing front-end circuit and sensitive sensors for the measurement system.)

1.4 Contributions

This thesis has made significant contributions in several areas of measurement and FEM simulation of BIS.

1. The influences of cell structure (including membrane thickness and cell shape) on the BIS were analysed with FEM. There was little research on the relationship between cell structure and BIS, hence this work has made a significant contribution on the bio-impedance analysis.

2. Proposed a FEM modelling technique for analysing the mechanism of how frozen-thaw injury influences the BIS of biological samples. The proposed model has been validated by impedance measurements and microscopic

experiments.

3. Proposed a modelling method based on 3-D FEM. This model is suitable for analysing the eddy current of non-contact induction measurement of bio-samples. The BIS can also be calculated using the proposed model.

4. Proposed an acceleration method for a thin shell FEM model. The acceleration method can reduce the meshing element and thus the computing time. This method is validated by simulations on a cell model and it can potentially be extended to other thin shell models.

1.5 Organization of the thesis

Chapter 1 introduces the motivation, aims, contributions and the novelty of the thesis. In addition, the outline of the thesis is presented.

Chapter 2 presents the background of BIS, including the basic mechanism of dielectric dispersion, the types of dispersion on bio-impedance spectroscopy, and the measurement system for measuring BIS. In addition, the application of bio-impedance spectroscopy on medical and food industrial is introduced in this section.

Chapter 3 describes the supporting theory of the analytical solution for cell suspension model, the basic theory of finite element method and simulation models for cell suspensions. It also introduces the basic theory of how to calculate the conductivity spectroscopy of a non-contact induction measurement system.

Chapter 4 demonstrates the simulation results of how cellular structure influences the bio-impedance spectroscopy. The cellular structure, including the cell shape, cell orientation and cell membrane thickness, is simulated based on finite element method. The simulation results are validated by the analytical solutions.

Chapter 5 introduces a contact electrode measurement system for measuring bio-impedance spectroscopy. The mechanism of the frozen-thaw injury that influences on bio-impedance spectroscopy is discussed in this section based on the measurement and simulation results. In addition, a microscopic experiment is carried out to validate the measurement and simulation results.

Chapter 6 describes a non-contact induction measurement system for measuring bio-impedance spectroscopy. A finite element based modelling method is proposed to simulate the frozen-thaw effect on biological samples.

Analytical solutions and microscopic experiments are carried out to validate the measurement and simulation results.

Chapter 7 introduces an acceleration method for thin shell bio-cell modelling based on finite element method. The acceleration method is applied to two-dimensional (2-D), three-dimensional (3-D) and cell shape deformation models. This method is validated by measurement result and analytical solution.

Chapter 8 concludes the findings and works accomplished in this thesis. The future work is recommended.

2 Background of bio-impedance spectroscopy

2.1 Introduction

It has been known for decades that the impedance spectroscopy of biological samples, while measured over a range of frequencies using time varying electromagnetic field, contains information about the physical, chemical or cellular properties of the samples [4] [5] [6]. Theoretically, the biological samples display a specific impedance spectroscopy based on the geometry structure and dielectric properties of cell membranes. The characteristics of BIS, in return, reflect geometry and electrical information of the biological samples. The biological impedance spectroscopy (BIS) [7] [8] [9] has been widely investigated for medical applications such as detection of tumour [10] and cerebral stroke [11] and electroporation treatment [12]. BIS has also been used for food industry applications. For example, it has been proposed for quality inspection of meat, vegetables and fruits [13] [14] [15]. In addition, it has also been used to monitoring the growth of yeasts [16] [17] [18] and the process of brewing [19].

BIS has mainly been performed by injecting current by electrodes placed on the biological samples but less so with inducing eddy currents in the biological samples by coils. The first method is to calculate the impedance of the biological samples by measuring the surface potential difference between electrodes and the current through them. This measurement method is fast

and effective. However, the polarisation of electrodes, which gathers charges on the surface of electrodes, produces an electrical field against the applied field lead to significant errors at a low frequency.

The second measurement method is a non-contact magnetic induction method. Eddy currents are induced in the biological samples by coils and the impedance spectroscopy is measured by detecting the resulting magnetic field / induced voltage.

2.2 The electromagnetic characteristics of cells

It has been found that the most bio-cells consist of three parts: cell membrane, cell nucleus and cytoplasm. The cell membrane primarily consists of phospholipid and proteins which are low-conductive. The cell membrane is used to separate the extracellular fluid from the intracellular fluid. The intracellular fluid consists of cell nucleus and cytoplasm which are the heredity and control centre of the cell. Every cell nucleus contains the genetic materials, deoxyribonucleic acid (DNA), which is enclosed by a nuclear membrane. The cell nucleus determines the function, shape and structure of the cell. The cytoplasm is a highly conductive fluid surrounded around the nucleus. It provides a platform for metabolism of the cell [21].

Every single cell is an integrated and complicated system. In order to simplify

the cell model for analysing its electromagnetic characteristics, a single cell model has been proposed by Asami [4] as shown in Figure 2-1. In Asami's model, the bio-cell consists of highly conductive intracellular (including cell nucleus and cytoplasm), extracellular fluid (consist of aqueous electrolytes) and low-conductive membranes as shown in Figure 2-1.

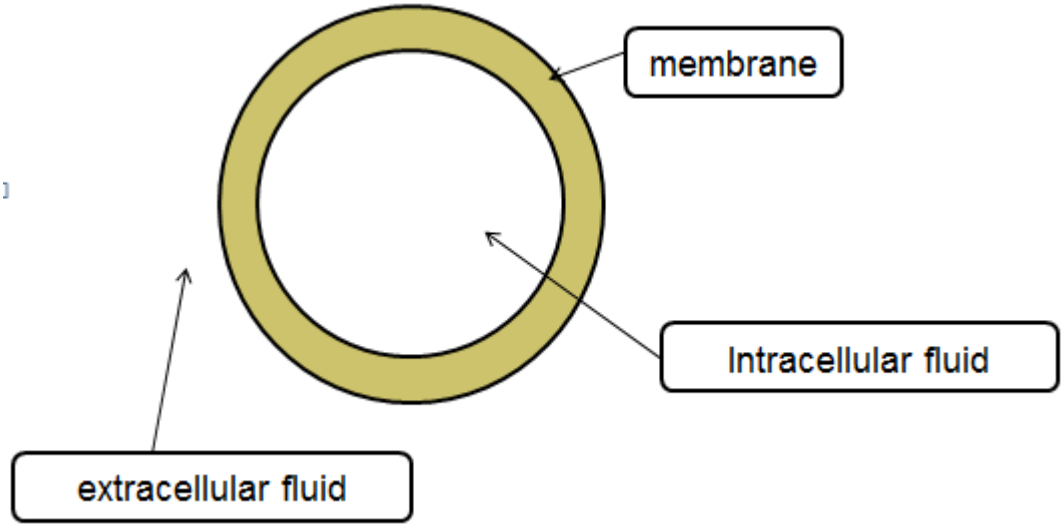

Figure 2-1: single-shell cell structure model

The single-shell cell model ignores the organelles since those have only little influence on the electrical behaviour. All the intracellular substances including cell nucleus and cytoplasm are considered as intracellular fluid which is highly conductive. The intracellular fluid mainly contains inorganic ion, water, amino acid and macromolecular protein which can be electrolysed into electric dipoles [22]. Since the cells cannot be exposed to the nature environment directly, the nutrition transfer is completed by the interaction between intracellular and extracellular fluid.

The extracellular fluid can be regarded as saline solution which consists of water, inorganic salt and other metabolite. Extracellular fluid provides the living environment for cells which refers to Pondus Hydrogenii (PH) value, saline concentration and so on.

Cell membranes separate the intracellular and extracellular fluid. However, water and some micro-molecular proteins can exchange between intracellular and extracellular fluid through membranes. This is because membranes are permeable selective due to the structure of itself [23]. Membranes primarily consist of phospholipid and proteins as shown in Figure 2-2.

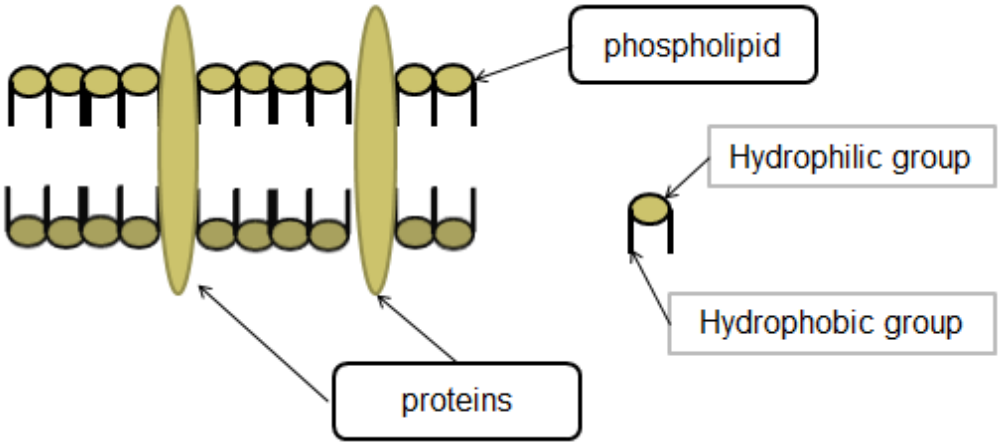

Figure 2-2: structure of membranes

Figure 2-2 illustrates that the phospholipids of cell membrane are arranged in sequence. Each phospholipid contains hydrophilic and hydrophobic groups. The hydrophilic groups are heading towards extracellular and intracellular fluid while hydrophobic groups are pointing to the inner side of membranes [24].

This refers to the basic function of membranes that separates the cells from external environment. The proteins shown in Figure 2-2 are inserted into the phospholipid. Those proteins work as channels that allow water and micro-molecular substance exchanging between extracellular and intracellular fluid. Some proteins only identify specific amino acid and nucleotide which makes the membranes permeable selective.

Due to the permeable selective characteristic of membranes, negative and positive ions can be accumulated around membranes as shown in Figure 2-3.

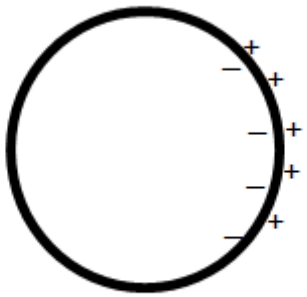

Figure 2-3: the charge distribution around membranes

Figure 2-3 shows that negative and positive ions are separated by cell membrane which is low-conductive. Therefore, the ions surrounded around the cell membrane behave as capacitance. The electrical characteristic of membrane is assumed to be large resistances in parallel with capacitances [25] [26] as shown in Figure 2-4.

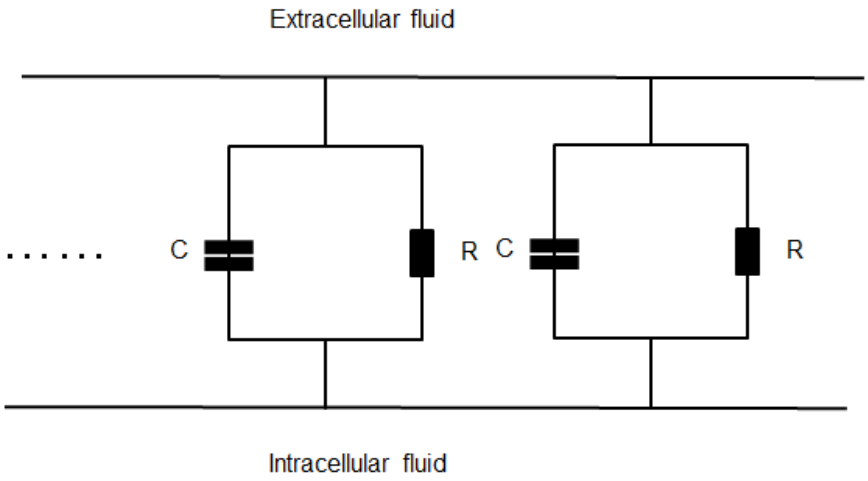

Figure 2-4: equivalent circuit of membranes

At a low frequency, the membranes have a significant large resistance compared with the fluid. So membranes can be viewed as isolator at a low frequency and blocks the current flow from the extra-cellular fluid to intra-cellular fluid. When the frequency becomes high, the capacitances function as a short circuit and the membranes becomes conductive and electrically invisible [27].

2.3 Dielectric relaxation of cells

There are many different kinds of electric dipoles in the intracellular and extracellular fluid. Proteins and DNA can be electrolysed into ionic groups or electric dipoles. Inorganic solutions contain inorganic ions that constitute dipoles.

Dielectric relaxation describes a phenomenon that the permittivity decreases when the frequency of applied electric field increases at a certain range. The relaxation occurs when the electric dipoles are not able to reverse at the same rate with the frequency of applied field [28], as shown in Figure 2-5.

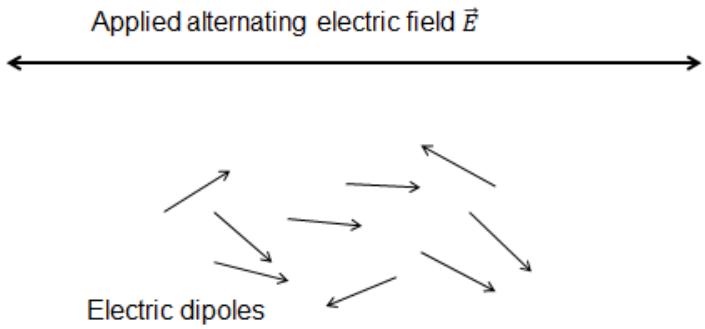

Figure 2-5: dipoles reversing with applied electric field

When applying a static electric field, the electric dipoles will point to a certain direction. Changing the direction of the applied field would reverse the electric dipoles. If the frequency of the applied field is low, there will not be dispersions since the dipoles can follow the change of applied field perfectly. However,

when the frequency of the field becomes higher, the electric dipoles cannot follow the rate of the field. And the electric dipoles would produce an induced electric field to reduce the applied field. The dielectric relaxation occurs and behaves as dispersions on the permittivity as shown in Figure 2-6. The electric dipoles will stop reversing when increasing the frequency of the applied field to infinity.

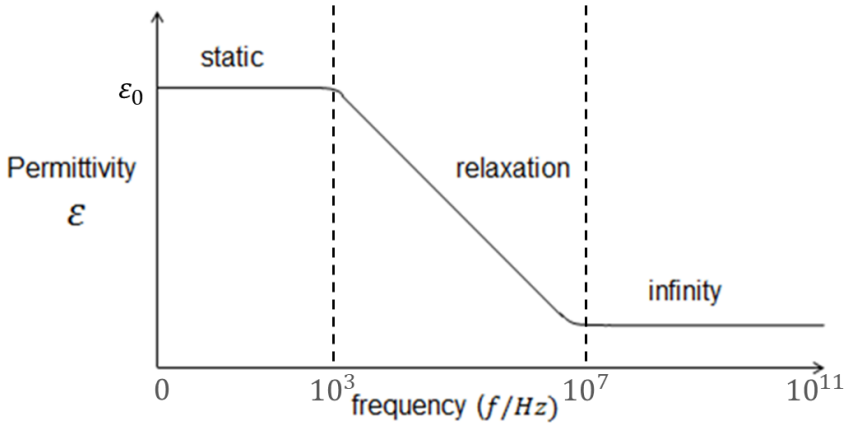

Figure 2-6: schematic illustration of relaxation on permittivity

The relaxation of permittivity $\varepsilon_r(\omega)$ in Figure 2-6 can be described by the Debye's equation [29]:

$$\varepsilon_r(\omega) = \varepsilon_r(\infty) + \frac{\varepsilon(0)-\varepsilon(\infty)}{1+i\omega\tau} \quad (2\text{-}1)$$

where $\varepsilon_r(\infty)$ stands for the permittivity at high frequency and $\varepsilon(0)$ is the permittivity at a low frequency. $\omega = 2\pi f$ where f is the frequency and τ is the relaxation constant. The equation describes how the permittivity changes with the frequency during a relaxation. There are different kinds of electric dipoles which exist in the intracellular and extracellular fluid. Therefore, when

an electric field applied, the permittivity and conductivity of cell exhibit relaxations over a wide range of frequency. This phenomenon is named bio-impedance dispersion.

2.4 Dispersions on bio-samples

According to the research carried out by Schwan, there are mainly three types of dispersion occurs on cells at different frequencies, as shown in Figure 2-7 [1].

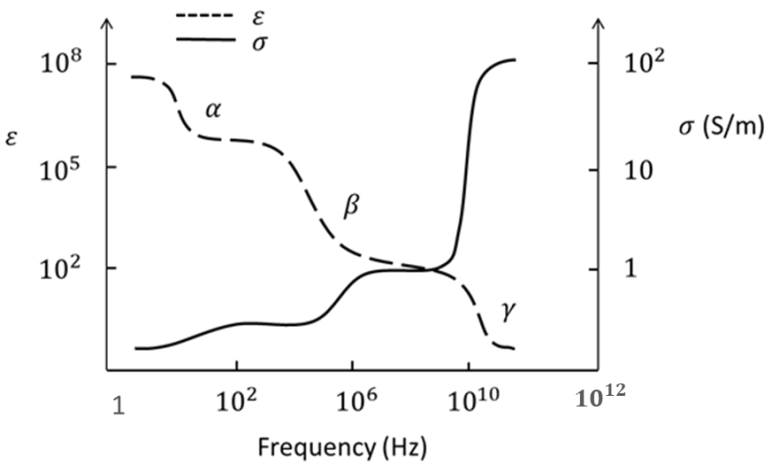

Figure 2-7: α, and γ dispersions (permittivity and conductivity related to frequency) [1].

2.4.1 α-dispersion

α-dispersion was found at low frequency ranging from 10-1000 Hz by Schwan [1]. The phenomenon was researched and illustrated by Pethig and Kell [2]. According to Schwan, α-dispersion is caused by the ions existing in ECF (extracellular fluid) and ICF (intracellular fluid). As described by Jean-Louis, Na^+ and Cl^- mainly exist in ECF while K^+ is in ICF [3]. Those ions can flow through the protein channels mentioned in Figure 2-2 which leads to the α-dispersion at a low frequency [30] [31].

2.4.2 β-dispersion

β-dispersion was observed from 10 kHz to 10 MHz. The dispersion was described by Schwan and can be explained by Maxwell-Wagner effect [1] [30] [32]. The effect occurs at the boundary of layered or inhomogeneous dielectrics. Applying electric field would build up charges at the boundaries created by different dielectrics. As shown in Figure 2-8, the double layer dielectrics system can be represented by one capacitance in parallel with another [33]. Applying a static electric field would charge both capacitances and creates charges at the boundary of the dielectrics. This phenomenon is also called interfacial polarisation. [33]

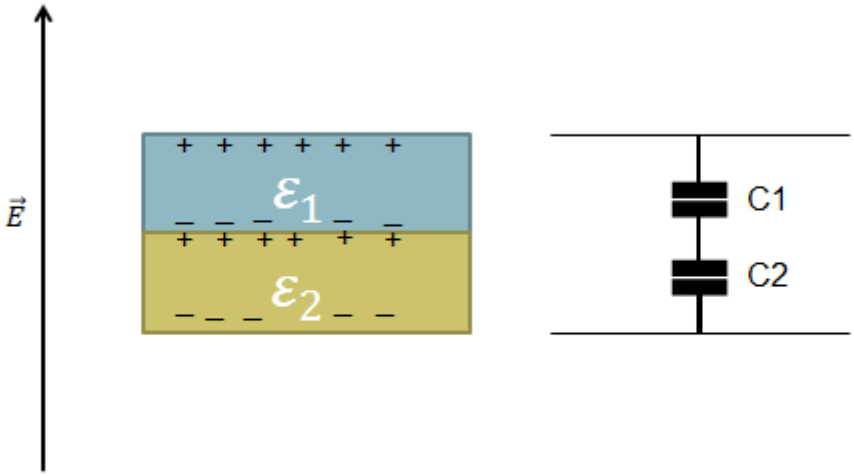

Figure 2-8: Equivalent diagram of double layer dielectrics

The ECF, membranes and ICF can be regarded as a triple layer system. The charging process is described by Figure 2-9.

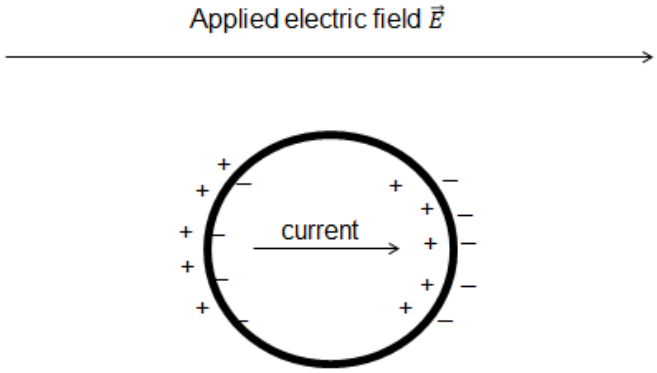

Figure 2-9: Maxwell-Wagner effect on single shell model of cell

The charges of the system inside the cell will move following the coulomb's law when applying a static electric field. Positive and negative charges accumulate

at different side of the cell. Changing the direction of the applied electric field will reverse the charges. β-dispersion occurs while the reverse rate of charges cannot follow the frequency of the applied electric field.

As the Maxwell-Wagner effect is related to the cellular structure, including geometrical information and electrical properties of cell, the β-dispersion in return reflects the information of cellular structure. So the β-dispersion has been widely investigated for cellular structure detection including bio-industrial and bio-medical applications.

2.4.3 γ-dispersion

γ-dispersion was found at frequency 1 GHz which was unexpected since the permanent dipoles like water relaxes at 20 GHz [34]. This was explained by Schwan [1] that the water bounded with proteins would have broad dispersion ranging from hundreds megahertz to several gigahertz. And the dipoles electrolysed from proteins and amino acid would have the same dispersion range around 1 GHz.

Since α-dispersion and γ-dispersion are irrelevant with the structural properties of cells, this thesis focuses on analysing β-dispersion which indicates how cellular structure and membrane properties influence the bio-impedance spectroscopy.

2.5 Simulation methods of BIS

2.5.1 FEM simulation

The idea of finite element was used centuries ago to estimate the perimeter of a circle by a polygon. The finite element method (FEM) was first introduced by Courant in 1943 to solve Saint Venant problem. However, it was successfully put in use until 1956 by Turner and Clough. Later in 1960, Clough defined and published the finite element method [43]. The main idea of FEM is to approach an entire continuous domain by finite discrete domains. The unknown function on the entire domain is represented by approximate functions on each subdomain. The approximate function usually expressed by interpolation function determined by unknown coefficients.

Sekine and Asami carried out FEM simulations on BIS to analyse the bio-impedance behaviour of biological samples [4] [22]. The electrical parameters of intracellular and extracellular fluid and cell membrane (i.e. conductivity and relative permittivity of intra and extra cellular fluid and cell membrane) were set according to the single cell model introduced by Asami [4]. In Sekine's model, β – dispersion of a custom single cell model was calculated based on FEM and it was verified by the Wagner's analytical solution with enough accuracy. The result shows that FEM model can be performed in multi-frequencies and therefore they are essentially applicable for analysing BIS. However, the Asami and Sekine's single cell model is restricted to the shape of the cell and the applied field. It can only be applied on spherical

cell model and electric field, which cannot describe the electrical characteristics of the cell suspension and food samples in real world.

This thesis proposed FEM models with variety of cell shapes and applied electro-magnetic field. The influence of cell structure (including cell shape, membrane thickness and orientation) on BIS has been analysed and a model for analysing frozen-thaw effect has been proposed in both 2-D and 3-D FEM simulations. The proposed models are the more realistic approach to frozen-thawed food samples and measurement systems.

2.5.2 Transport lattice method

The transport lattice method is to construct a transport lattice. Every element of the lattice consists of resistance and conductance to represent the permittivity and conductivity of the cell and the suspension.

As shown in Figure 2-10 [41], the elements are divided into three models: intracellular model, extracellular model and membrane model. Each model is represented by the combination of circuit elements such as resistance and capacitance. The cell and suspension system can be represented by a large electric diagram. The permittivity and conductivity can be calculated easily based on the electric diagram. This method is an estimation approach for the BIS of the cell model. The accuracy is relatively low comparing to the FEM simulation. The boundary conditions of cell membranes can be complex and

requires a more effective and accurate simulation method. Therefore, this thesis proposed models to simulate the BIS of biological cell suspensions based on FEM.

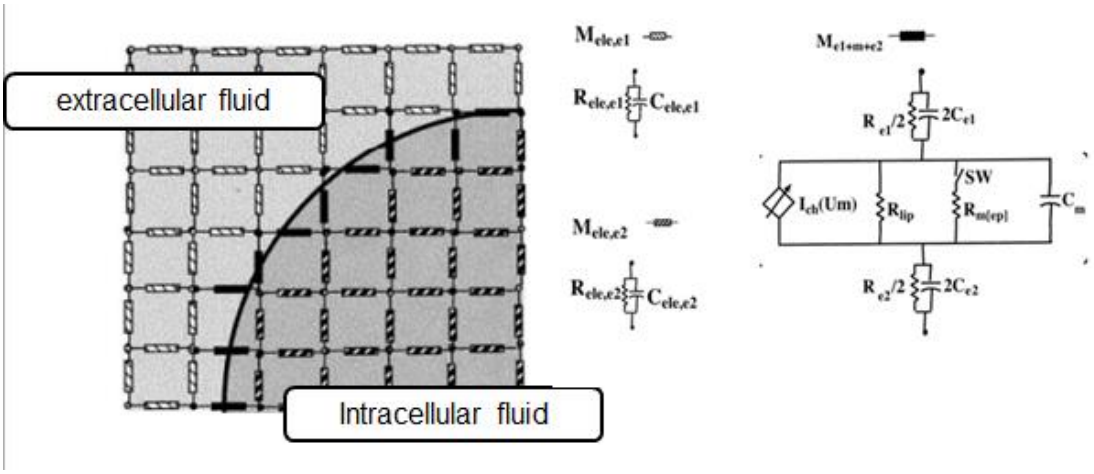

Figure 2-10: Cell model using transport lattice method [41]

2.6 Measurement methods of BIS

2.6.1 Electrode measurement method

Biological samples exhibit frequency dependent spectra caused by a dispersion mechanism. This dispersion mechanism demonstrates dielectric relaxation due to the interaction between electromagnetic field and biological samples at cellular levels. Hence, biological impedance spectroscopy may be used to reveal the electrical and geometrical properties of biological samples [52] [53] [54], in particular, frozen-thaw injury.

Frozen-thaw injury is known as one of the most common factors that can

influence the bio-impedance spectroscopy of biological samples [13] [55] [56]. However, the mechanism of how frozen-thaw injury influences the bio-impedance spectroscopy at cellular levels has not been analysed. The influence of frozen-thaw injury on β-dispersion was experimentally investigated using the AC conduction (contact electrode) method on potato and pork samples. From the results of the experiment, we assumed that frozen-thaw injury mainly influences the impedance spectroscopy of a potato and pork by breaking their cell membranes. In light of this assumption, a FEM model to simulate membrane breakage was developed and a microscopic experiment was then carried out to identify the membrane integrity.

The influence of frozen-thaw injury on dielectric properties of biological cells suspension was simulated using a custom developed FEM solver and an originally designed cell model. In its 2-D version, the AC conduction case was simulated. Then, in the attempt to confirm the assumption, a microscopic experiment was conducted to determine if the cell membrane was broken or not.

The measurement and simulation results suggest that bio-impedance measurements provide an indication of cellular structural changes of biological samples, which can be useful for biomedical [57] [58] [59] [60], pharmaceutical [61] [62] [63] [64] and food inspection applications [65] [66].

The biological samples exhibit a specific β-dispersion based on the geometric structure and dielectric properties of cell membranes. The characteristics of

β-dispersion reflect the geometric and electrical information of the biological samples. Geometric structure is considered to be one of the most important peculiarities of biological samples. FEM simulations were carried out to analyse the dielectric properties of bio-cell suspension by applying an alternating electric field in a contact manner. Sekine [22] and Asami [4] carried out FEM simulations regarding spherical biological cell suspension under an alternating electric field. These simulations can be performed in multi-frequencies and therefore they are essentially virtual biological impedance spectroscopy (BIS) [67].

BIS is a measurement that has mainly been performed by using electrodes, placed on the biological samples to inject current [68] [69]. The purpose of the measurement is to calculate the impedance of the biological samples by measuring the potential differences between the surfaces of the electrodes as well as the currents passing through the electrodes. This measurement method is fast and effective [70]. However, it only involves two electrodes, resulting in the polarisation of electrodes. This then causes charges to gather on the surface of electrodes, producing an electrical field against the applied field and this leads to significant errors at lower frequencies. A four-terminal measurement was performed to minimize the errors caused by electrode polarisation [20] and the measurement was simulated using the 2-D finite element method.

An electrode contact measurement was carried out in the chapter to verify the

effect of freeze-thaw injury on the impedance spectroscopy of potatoes. A microscopic experiment and an original FEM simulation model have been designed to identify the mechanism of how freeze-thaw injury influences the impedance spectroscopy of potatoes.

2.6.2 Non-contact induction method

In order to overcome the shortcoming of previous research method, contact-electrode method, a non-contact magnetic induction system was built, which contains a custom-designed front-end circuit and a Zurich lock-in amplifier for data acquisition. The system was used to measure the conductivity spectra of potato and fresh loin pork before and after frozen-thaw. The measurement accuracy of the system is 0.01 S/m over a bandwidth of 400 kHz to 6 MHz. In addition, a cell-level simulation model was built using finite element method to elucidate the measurement results and provide an explanation based on the structural change of cell membrane. The results from the non-contact magnetic induction measurement agree well with the observations from the microscopic experiments. The non-contact nature of the method is significant as it has the potential for use in real world applications for fast scanning of food products where contact method is not ideal.

Bio-impedance spectroscopy (BIS) measures the complex impedance of biological samples over a wide range of frequencies. The measured

impedance spectroscopy has been extensively used to characterize the physiological state of biological samples [11] [75].

BIS has been widely investigated for medical [76] [77] [78] and food industry applications such as quality inspection of meat [56] [79] [80], fruits and vegetables [65][81]. Food freezing is one of the factors that influence the quality of food including deterioration of nutrition and texture. However, some merchants mislabel their frozen-thawed food as fresh food illegally for higher profits [82]. Therefore, a rapid and effective method to differentiate the frozen-thawed and fresh food is indispensable. The electrode contact measurement method has been used to distinguish frozen-thawed food samples such as chicken breast [82]. The response of the electrode contact measurement method is fast and accurate. However, the contact method is hard to apply on industry applications. Furthermore, the direct contact of electrodes and the food samples can lead to unnecessary error of the measurement such as chemical reaction between food samples and electrode, electrode polarisation at low frequency and physical damage on the tissues of food.

A non-contact induction measurement system is introduced to measure the BIS. The non-contact measurement is more challenging than direct contact method and it has some difficulties on enhancing the sensitivity. However, the non-contact measurement is entirely non-destructive and eliminates the problems caused by direct contact electrodes [83] [84] [85]. This system is well

suited for industrial applications with accuracy of 0.01 S/m over a frequency range from 400 kHz to 6 MHz.

The bio-impedance spectroscopy of fresh and frozen-thawed food samples (potato and loin pork) has been measured using the non-contact system. In order to further expound the measurement results, a 3-D cellular model has been built using finite element method. The BIS of the cellular model is carried out by analysing eddy currents induced by alternating magnetic field in a non-contact manner. This is a more realistic approach to non-contact measurement comparing with existing models built by Asami and Sekine [4] [22]. Furthermore, a new method to calculate the equivalent conductivity and relative permittivity of the biological suspension in FEM eddy current simulation is introduced. These simulations can be performed in multi-frequencies and therefore they are essentially virtual biological impedance spectroscopy (BIS). In addition, a microscopic experiment has been carried out to analyse the frozen-thaw injuries on cell membranes.

2.6.3 Other measurement methods

2.6.3.1 Electro-rotation method

The electro-rotation method is to add two pairs of electrodes perpendicular to each other on one cell as shown in Figure 2-11. The electric field is applied on

each pair of electrodes with the same magnitude but 90 degree phase difference.

Suppose the applied electric fields are:

$$E_1 = E_0 \cos(\omega t) \tag{2-2}$$

$$E_2 = E_0 \sin(\omega t) \tag{2-3}$$

And the total electric field is:

$$\mathrm{E}^2 = E_0^2[cos^2(\omega t) + sin^2(\omega t)] = E_0^2 \tag{2-4}$$

This is equivalent to an electric field with magnitude E rotating with angular speed ω. The parameters of dielectric properties can be calculated according to the rotation moment and frequency [48]. This method has difficulties on measuring the rotation moment and it requires a system with high-precision set-up. It is designed for analysing the BIS of a single cell rather than cell suspensions and food samples, which is not applicable for the purport of this thesis - analysing the BIS of food samples.

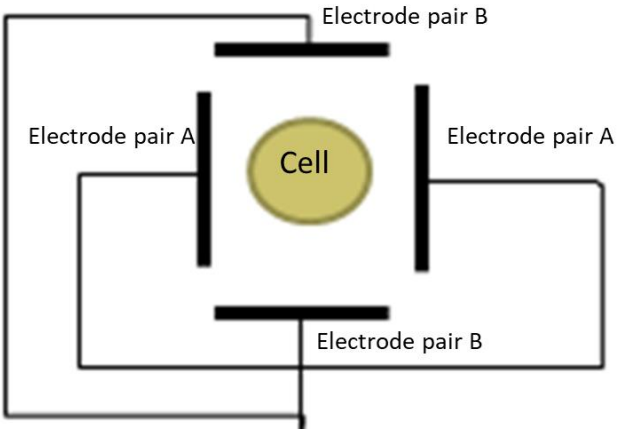

Figure 2-11: Electro-rotation method

2.6.3.2 Micropipette method

The micropipette method requires a system with high-sensitive and high-operational set-up. This method is achieved by inserting an electrode into the cell without destroying the cell structure. The schematic diagram is shown in Figure 2-12. The micropipette is used to open a micro pore on the membrane without damaging to the cell. Then an electrode can be inserted into the cell through the pore. The electrical characteristics of the membranes and intracellular fluid can be measured [69]. This method still has technical difficulties such as the accuracy of the electrode sensor, the sensitivity of the sensor and the polarisation on the electrode. It is designed to analyse the BIS of intracellular fluid and cell membranes rather than the BIS of cell suspensions and food samples. Alternatively, electrode measurement method and induction measurement method, which are more applicable on measuring cell suspensions and food samples, were used in this thesis to analyse the frozen-thaw effect of food samples.

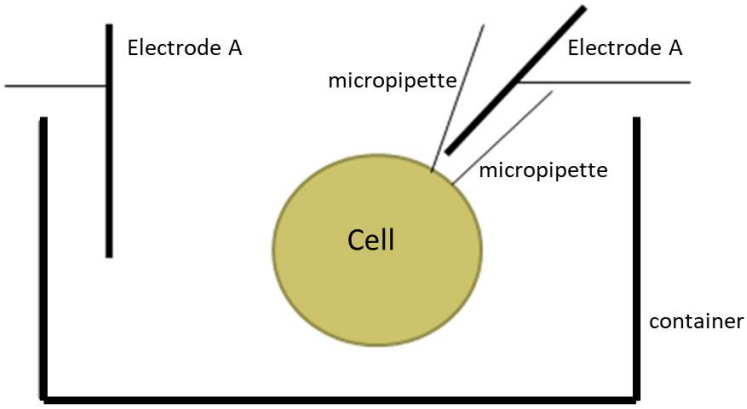

Figure 2-12: Micropipette method

3 Supporting theory

3.1 Analytical solution on relative permittivity of cell models

The single cell model introduced by Asami [4] [41] is shown in Figure 3-1. The parameters of the cell model are $k_m = 10^{-7}$ S/m, $k_a = k_c = 1$ S/m. $\varepsilon_c = \varepsilon_a = 80$, $\varepsilon_m = 5$, R = 5000 nm, $d_m = 5\text{nm}$. k_m is the conductivity of the cell membrane. k_a and k_c are the conductivity of the extracellular and intracellular fluid, respectively. ε_c and ε_a are the relative permittivity of the intracellular and extracellular fluid, respectively. ε_m is the relative permittivity of the cell membrane. R is the radius of the cell. d_m is the cell membrane thickness.

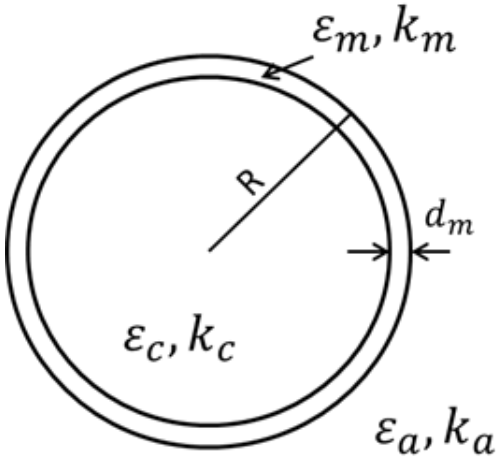

Figure 3-1: single shell model [4]

The equivalent complex relative permittivity of the cell model in Figure 3-1 can be calculated according to Asami [4]:

$$\varepsilon_p^* = \varepsilon_m^* \frac{2(1-v)\varepsilon_m^* + (1+2v)\varepsilon_c^*}{(2+v)\varepsilon_m^* + (1-v)\varepsilon_c^*} \quad (3\text{-}1)$$

where $v = (1 - \frac{dm}{R})^n$, dm is the membrane thickness, R is the radius of cell. When $n = 2$, the equation is applied to two-dimension analytical model. When $n = 3$, the equation is applied to three-dimension analytical model. ε_p^* is the complex relative permittivity of the cell model, ε_m^* is the complex relative permittivity of membrane and ε_c^* is the complex relative permittivity of cytoplasm. Then the complex relative permittivity of the suspension can be calculated by Wagner's equation [4] [22]:

$$\varepsilon^* = \varepsilon_a^* \frac{2(1-P)\varepsilon_a^* + (1+2P)\varepsilon_p^*}{(2+P)\varepsilon_a^* + (1-P)\varepsilon_p^*} \quad (3\text{-}2)$$

where P is the volume fraction. ε^* is the complex relative permittivity of cell suspension, ε_a^* is the complex relative permittivity of the external medium. The conductivity of the suspension can be derived:

$$\sigma^* = j\omega\varepsilon_0\varepsilon^* \quad (3\text{-}3)$$

where σ^* is the complex conductivity of the suspension. ε_0 is the permittivity of vacuum, $\omega = 2\pi f$ where f is the frequency of the applied field and j is the imaginary unit.

The dielectric properties of the cell suspension of the custom single cell model can be calculated based on equation (3-2). This is the analytical solution to calculate the BIS of the single cell model. The calculated result is used to verify the FEM simulation result.

3.2 Two-dimensional finite element

Normally, the finite element problems can be solved by two kinds of methods which are Galerkin's method and Ritz's method [42] [43]. In this thesis , the Galerkin's method is used to build up simulations.

For electro-magnetic problems, the system function is [43]:

$$L\emptyset = g \quad (3\text{-}4)$$

where L is the Laplace operator, $\emptyset$ is the unknown field function, g is the given exciting function.

According to the Gaussian equation,

$$\nabla \cdot \vec{D} = \rho \quad (3\text{-}5)$$

where $\vec{D} = \varepsilon\vec{E}$, $\vec{D}$ is the electric flux density, $\vec{E}$ is the electrical field intensity. $\varepsilon = \varepsilon_r\varepsilon_0$. ε_r is the relative permittivity of the material. ρ is the quantity of

electric charge which is zero in the cell model. So the equation can be rewritten as:

$$\nabla \cdot (\sigma + j\omega\varepsilon)\vec{E} = \nabla \cdot (\sigma + j\omega\varepsilon)\nabla U = 0 \quad (3\text{-}6)$$

where σ is the conductivity of the material and $\varepsilon = \varepsilon_r \varepsilon_0$. ε_r is the relative permittivity of the material. ε_0 is the permittivity of vacuum. U is the electric potential which is the objective value to be solved [43]. To obtain the equivalent conductivity of the total cell suspension, we calculate the total current flowing through the cell suspension from the top electrode to bottom electrode. According to the Kirchhoff's current law, the current flow through any plane which is in parallel with the electrodes is the same with the total current flow through the cell suspension. So the current *I* flow through a chosen plane in parallel with electrodes can be calculated as:

$$I = \sum j^{(i)} = \sum \sigma^{(n)} \vec{E}^{(i)} \quad (3\text{-}7)$$

where $j^{(i)}$ is the current density of the element on the chosen plane. $\sigma^{(n)}$ is the conductivity of the element on the chosen plane. $\vec{E}^{(i)}$ is the background electrical field on the chosen plane. Then the complex conductivity of the cell suspension can be calculated as:

$$\sigma^* = \frac{1}{\rho^*} = \frac{L_1}{S} * \frac{I}{U} \quad (3\text{-}8)$$

where σ^* and ρ^* are the complex conductivity and resistivity respectively. L_1 is the distance between the top electrode and the bottom electrode. S is the area of the electrodes. U is the electrical potential, I is the current.

3.3 Three-dimensional finite element

An induction model is built for the 3-D FEM simulation. As shown in Figure 3-2, the cylinder stands for the cell suspension and the spherical model stands for the cell. Imaginary transmitter and receiver coils are put on the top of the suspension to provide alternating magnetic field as an exciting signal and detect induced secondary magnetic field. The cell models were put randomly in the cell suspension model in order to simulate the realistic cell suspension.

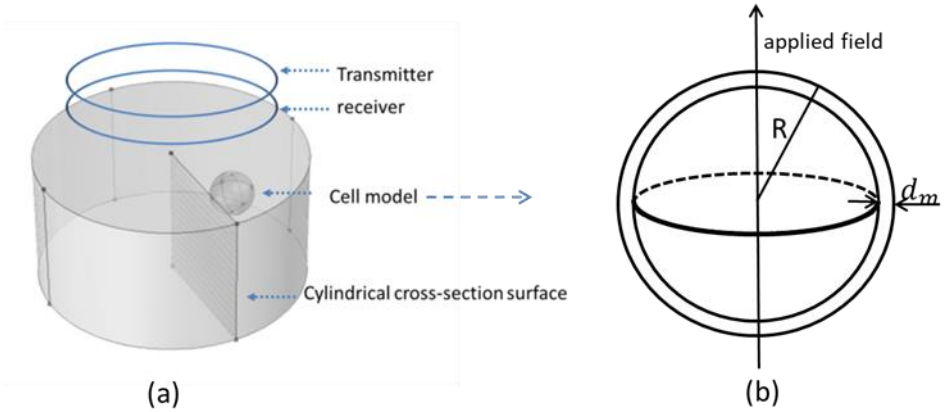

Figure 3-2: 3-D FEM simulation model (a) suspension model (b) cell model

The differential form of Maxwell's equation [43]:

$$\begin{Bmatrix} divD = 0 \\ divB = 0 \\ curlE = -\frac{\partial B}{\partial t} \\ curlH = j + \frac{\partial D}{\partial t} \end{Bmatrix} \quad (3\text{-}9)$$

where D is the displacement field. B is the magnetic field. H is the magnetizing field. E is the electric field.

In this FEM simulation, the system is regarded to be quasi-static which assumes the influence of displacement current is very small that it can be

ignored comparing with the eddy current induced by coil excitation. Time varying magnetic fields exist in nonconductive regions Ω_n and conductive regions Ω_c. So the Maxwell's equation can be written as:

$$\begin{Bmatrix} div\ B = 0 & in\ \Omega_n \\ curl\ E = -\frac{\partial B}{\partial t} & in\ \Omega_c \\ curl\ H = j_0 & in\ \Omega_n \\ curl\ H = j & in\ \Omega_c \end{Bmatrix} \quad (3\text{-}10)$$

where j_0 is the given current density in Ω_n excited by coil. j is the current density in Ω_c. H is the magnetic field intensity. B is the magnetic flux density. E is the electric field intensity.

And the field quantities are following the equations:

$$\mathrm{B} = \mu\mathrm{H}\ ,\ \mathrm{H} = vB \qquad in\ \Omega_n\ and\ \Omega_c \quad (3\text{-}11)$$

$$\mathrm{j} = \sigma\mathrm{E}\ ,\ \mathrm{E} = \rho\mathrm{j} \qquad \mathrm{in}\ \Omega_c \quad (3\text{-}12)$$

where μ denotes the permeability, v is the reluctivity, σ is the conductivity and ρ is the resistivity.

According to Oszkar Biro [44], the basic formulas for the three-dimension edge elements simulation of eddy current problems, Galerkin's equation is shown as following:

$$\int_{\Omega_c} curlN_i \cdot vcurlA^{(n)} d\Omega + \int_{\Omega_c} j\omega\sigma N_i \cdot A^{(n)} d\Omega + \int_{\Omega_c} \sigma N_i \cdot gradV^{(n)} d\Omega =$$

$$\int_{\Omega_c} curlN_i \cdot v_0 curlA_s d\Omega \qquad i = 1,2,\dots,6 \quad (3\text{-}13)$$

$$\int_{\Omega_c} j\omega\sigma gradL_i \cdot A^{(n)} d\Omega + \int_{\Omega_c} \sigma gradL_i \cdot gradV^{(n)} d\Omega = 0 \qquad i = 1,2,\dots,4 \quad (3\text{-}14)$$

where L_i is the elemental interpolation of i^{th} node corresponding to the nth

element of it; N_i stands for the vector interpolation of i^{th} edge relating to the n[th] edge element of it; $A^{(n)}$ stands for the excited edge vector potential of the n[th] element; A_s represents the original edge vector potential of the n[th] element; $V^{(n)}$ represents the electrical potential excited by the n[th] element on the receiving coil;v stands for the reluctivity of the model;v_0 is the reluctivity of the air;σ is the conductivity of the model [42] [45] [46].

The first component of equation (3-13) $\int_{\Omega_c} curlN_i \cdot vcurlA^{(n)} d\Omega$ stands for the fundamental formation of the vector potential. The second term of equation (3-13) $\int_{\Omega_c} j\omega\sigma N_i \cdot A^{(n)} d\Omega$ describes the diffusion effect. The third term of the equation (3-13) $\int_{\Omega_c} \sigma N_i \cdot gradV^{(n)} d\Omega$ relates to Maxwell-Wagner effect. The Maxwell-Wagner effect occurs on the surface of inhomogeneous materials, so the third component of equation (3-13) is strongly influenced by the shape of the measured objects.

The eddy current density is:

$$J^{(i)} = \sigma^{(i)} E^{(i)} \tag{3-15}$$

where $E^{(i)}$ denotes the vector sum of the electrical field on all the edges of each tetrahedral element. $\sigma^{(i)}$ is the complex conductivity parameter of the of each tetrahedral element.

The model is shown in Figure 3-2. Assume there is an equivalent model with uniform dielectric. The background suspension of the equivalent model has exactly the same shape with the simulation model in Figure 3-2. Since the normal component of electrical field relative to each cross-section surface of

suspension (shown in Figure 3-2) is identical, then

$$\sum \vec{n} \cdot E^{(i)} = \sum \vec{n} \cdot E_s^{(i)} \quad (3\text{-}16)$$

where, $E_s^{(i)}$ denotes the background electrical field of the of each tetrahedral element; $\vec{n}$ is the normal unit vector relative to the surface of target;

Since the equivalent model is uniform, the electrical background field $E_s^{(i)}$ is always vertical to every cylindrical cross-section surface of the suspension model shown in Figure 3-2. Then the equivalent complex conductivity of the original suspension (as shown in Figure 3-2) can be derived from (3-8) and (3-9) that

$$\sigma_s = \frac{\sum J_s^{(i)}}{\sum \vec{n}_{(i)} \cdot \frac{J^{(i)}}{\sigma^{(i)}}} \quad (3\text{-}17)$$

$\sigma^{(i)}$ is the complex conductivity of each tetrahedral element. $J_s^{(i)}$ is the eddy current density through each cylindrical cross-section of equivalent suspension model. $J^{(i)}$ is the eddy current density through each cylindrical cross-section of the original suspension model with arranged cells. $\vec{n}_{(i)}$ is the current flow direction.

3.4 Calculating conductivity of measurement result

According to A Barai[39], the measurement result is related to the conductivity and permittivity of suspension following the equation:

$$\frac{\Delta V}{V} = Pf\mu_0(2\pi f\varepsilon_0\varepsilon_r - j\sigma) + QX \quad (3\text{-}18)$$

where P is a constant of volume factor which is calibrated by saline solution with certain conductivity. f is the frequency. ε_0, μ_0 are the permittivity and permeability of vacuum respectively. σ, ε_r and X are the electrical conductivity, relative permittivity and magnetic susceptibility of the sample. ΔV is the detected electromotive force from the receive coil while V is the excitation from the transmit coil. It can be obtained from the equation that the conductivity is proportional to the imaginary part of $\frac{\Delta V}{V}$ and permittivity is proportional to the real part of $\frac{\Delta V}{V}$ [38]. The conductivity can be derived as:

$$\sigma = -\frac{Im\left(\frac{\Delta V}{V}\right)}{Pf\mu_0} = K\frac{Im\left(\frac{\Delta V}{V}\right)}{f} \quad (3\text{-}19)$$

where $K = \frac{-1}{P\mu_0}$ and K is a constant. The constant K can be calibrated by measuring saline solutions with certain conductivity.

3.5 Measurement and experimental set-up

3.5.1 Contact electrode measurement set-up

The contact electrode method has been well developed for measuring the bio-impedance spectroscopy [35] [36] [37]. It is a fast and effective way to measure the impedance of biological samples. The measurement set-up in this thesis is a simple system with two copper electrodes and four measurement terminals. The impedance analyser is Solartron 1260. The electrodes are copper electrodes with effective area of is $S = 2\ cm * 3\ cm = 6\ cm^2$, and the distance between the electric field measuring electrodes is $L = 6.6\ cm$. The conductivity can then be calculated by $\sigma = 1/\rho = L/RS$. R is

the real part of the measured impedance, ρ is the resistivity. The measurement sample is saline solution, potato and loin pork.

3.5.2 Non-contact induction measurement set-up

A front end circuit is designed to measure the change of conductivity and permittivity at frequency domain. There are mainly five parts of the circuit: a signal generator, a power amplifier, a transmitter and a receiver and a Zurich lock-in amplifier as shown in Figure 3-3 and Figure 3-4.

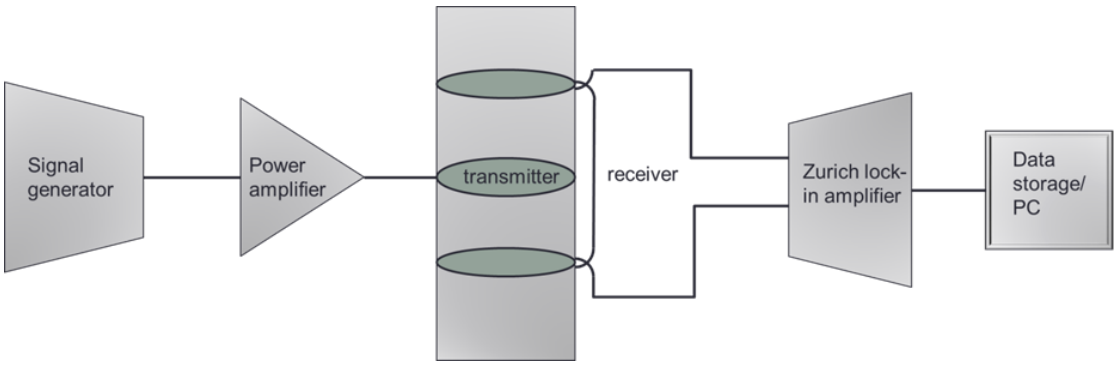

Figure 3-3: Flow diagram of measurement process

Figure 3-4: Non-contact measurement set-up.

The whole system is running at the following way: a sinusoidal wave is generated by the signal generator (Zurich lock-in amplifier) and amplified by the power amplifier. The amplifier input a high current to the transmit coil. And

the current generates a magnetic field which would induce eddy currents in the tested cell suspension. The eddy currents would generate a second magnetic field which is detected by the receiver coil [38] [39]. This signal is obtained by Zurich lock-in amplifier and stored into PC. The impedance of the cell suspension influences the magnitude and phase of the signal detected by the receive coil. And in turn, the equivalent impedance of the suspension can be calculated by comparing the signal detected by the receiver and the transmitter. The receive coil is connected in opposite directions so that the magnetic field induced by the same excitation is cancelled. And the receive coil only detects the magnetic field induced by cell suspension when the system is balanced [38].

The measurement at each frequency has been repeated 100 times to obtain the average value and increase the SNR of the results.

3.5.3 Microscopic experiments

Propidium Iodide (PI) is selected to be the chemical stainer for food samples. The characteristic of PI is that it can only stain dead cells with disintegrate membranes while integrate membrane can prevent living cells from the PI stainer [40]. Therefore, PI is an effective stainer to identify the integrity of cell membranes. The PI stainer is prepared by mixing Propidium Iodide with

distilled water (weight ratio 1:1). The food sample slides are prepared immediately after impedance measurement. The microscope is Zeiss-Axio scope A1 which is a fluorescent scope and it is capable to take snapshot during the microscopic observations.

4 Influence of cell structures on the BIS analysed by simulation result

4.1 Introduction

The simulated BIS of cell model is carried out based on the FEM. To analyse the influence of cell structure on BIS, the parameters including cell shape, cell membrane thickness and cell orientation are studied. The simulation results of the custom cell model are validated by analytical result.

4.2 Simulation of custom cell model

4.2.1 2-D simulation

The cell model used in this section is shown in Figure 3-1. The cell suspension model is shown in Figure 4-1. The square in Figure 4-1 stands for the cell suspension and the spheres are the cell models. Cell models are placed randomly in the cell suspension to simulate realistic suspension. A 10-volt electrical field is added to the top electrode and the bottom electrode is grounded. The size of the suspension is set at $100\mu m \times 100\mu m$, and the parameters of each cell are set according to Asami. The complex permittivity and complex conductivity of the cell suspension model can be derived as:

$$\varepsilon_m^* = \frac{\sigma_m^*}{j\omega\varepsilon_0} = \frac{k_m + j\omega\varepsilon_m\varepsilon_0}{j\omega\varepsilon_0} \quad (4\text{-}1)$$

$$\varepsilon_c^* = \frac{\sigma_c^*}{j\omega\varepsilon_0} = \frac{k_c + j\omega\varepsilon_c\varepsilon_0}{j\omega\varepsilon_0} \quad (4\text{-}2)$$

$$\varepsilon_a^* = \frac{\sigma_a^*}{j\omega\varepsilon_0} = \frac{k_a + j\omega\varepsilon_a\varepsilon_0}{j\omega\varepsilon_0} \quad (4\text{-}3)$$

where $\omega = 2\pi f$ and ε_0 is the permittivity of vacuum. f is the frequency of the applied electromagnetic field. k_m is the conductivity of cell membrane. k_a and k_c are the conductivity of extra and intra cellular fluid respectively. ε_m is the permittivity of membrane. ε_c and ε_a are the permittivity of extracellular and intracellular fluid respectively. ${\varepsilon_a}^*$ and ${\varepsilon_c}^*$ are the complex relative permittivity of extra and intra cellular fluid respectively. ${\varepsilon_m}^*$ is the complex relative permittivity of membrane.

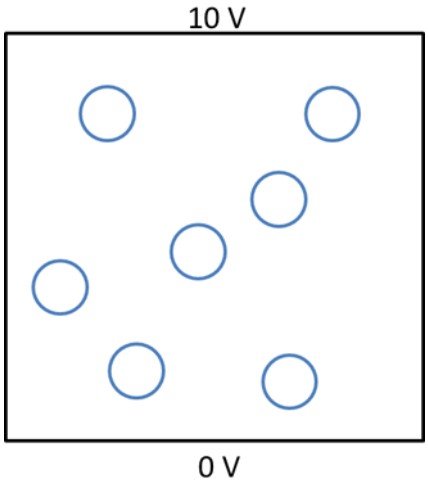

Figure 4-1: 2-D cell suspension model

The electric potential distributions of the cell suspension at low frequency (1 kHz) and high frequency (10 kHz) are shown in Figure 4-2 and Figure 4-3 respectively. The cell model behaves non-conductive and blocks current flow at the low frequency while the cell model behaves electrically invisible and conductive at the high frequency. This agrees with the expectations of published work [4] [27]. The spectroscopy of relative permittivity of the cell suspension is shown in Figure 4-4. The spectroscopy shows the β-dispersion

with the frequency ranging from 100 kHz to 10 MHz. Analytical solution of sphere cell model is carried out in Figure 4-4 to validate the FEM result. The frequency range and magnitude of the β-dispersion of analytical result based on supporting theory agree with the result of FEM simulation. There are 1% error between the analytical result and the FEM simulation result. This can be caused by the system error of finite element method itself and the meshing accuracy. Both the simulation and the analytical results agree with the published work that the cell model exhibits a β-dispersion when applied an alternating electric field [48] [49] [50]. Overall, the 2-D FEM simulation on the cell suspension model is accurate enough to show the progress of β-dispersion.

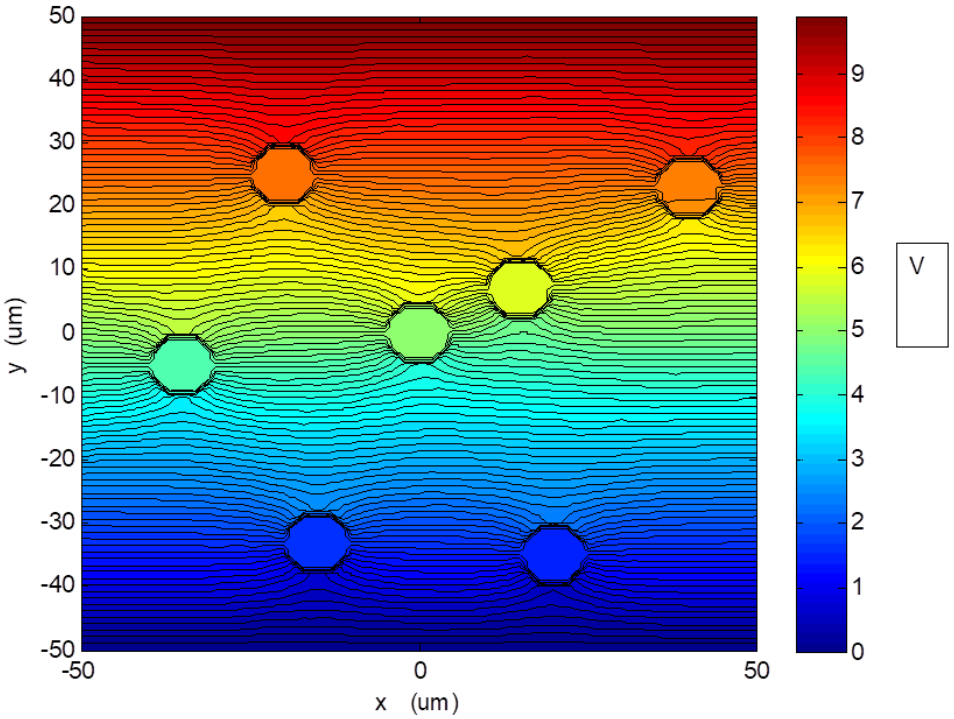

Figure 4-2: Electric potential distribution of 2-D cell suspension at low frequency (1kHz)

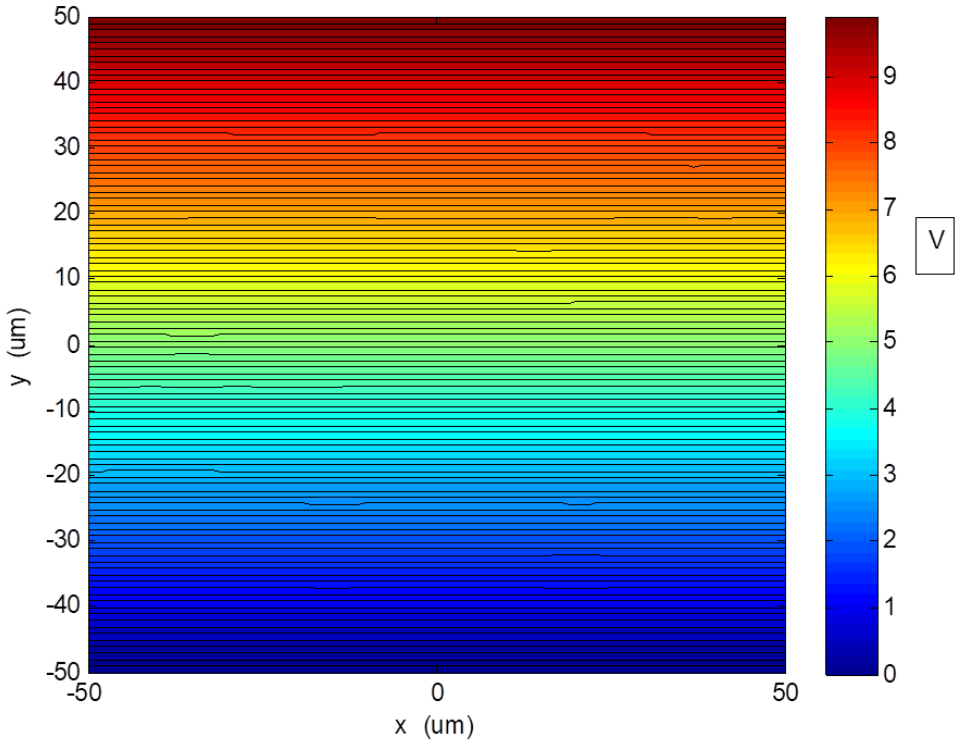

Figure 4-3: Electric potential distribution of 2-D cell suspension at high frequency (10MHz)

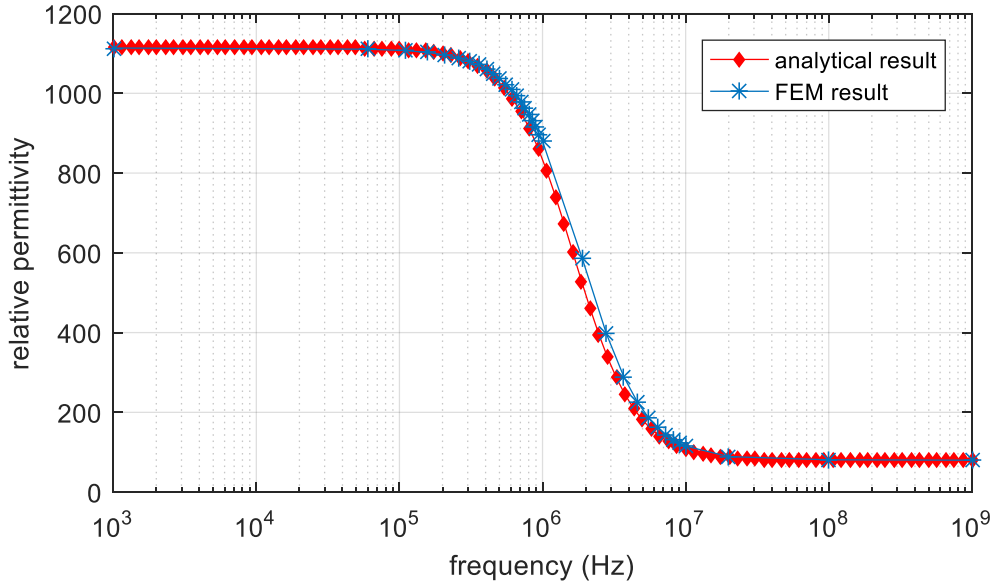

Figure 4-4: β-dispersion of 2-D cell suspension

4.2.2 3-D simulation result of custom cell model

The simulation model of 3-D cell suspension is shown in Figure 4-5. As shown in Figure 4-5, the cylinder represents the cell suspension (mixing of extracellular fluid and cells) and the spheres stand for the custom cell models. Alternating magnetic field is provided by the imaginary transmitter coils on the top of the cylinder. And induced secondary magnetic field is measured by the imaginary receiver coil. The cell models (spheres) are put randomly in the suspension to simulate realistic suspension.

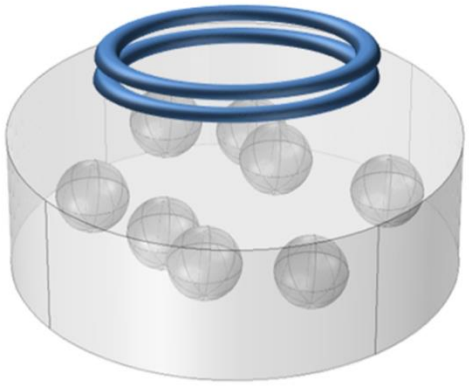

Figure 4-5: 3-D cell suspension model

The eddy current distribution of the cell suspension is shown in Figure 4-6. The eddy current distribution shows the same trend of the 2-D FEM simulation. The cell model blocks current flow at low frequency (10 kHz) and becomes conductive and electrically invisible at high frequency (10 MHz). The spectroscopy of the permittivity of cell suspension is shown in Figure 4-7. The permittivity spectroscopy shows the progress of β-dispersion and the result is validated by the analytical solution. The frequency range of β-dispersion is ranging from 100 kHz to 10 MHz. The simulation result agrees with the

expectations on the β-dispersion of published works [4] [49] [50]. The error of FEM result and analytical result is less than 1%. The error can be caused by the meshing accuracy and the system error of the finite element method.

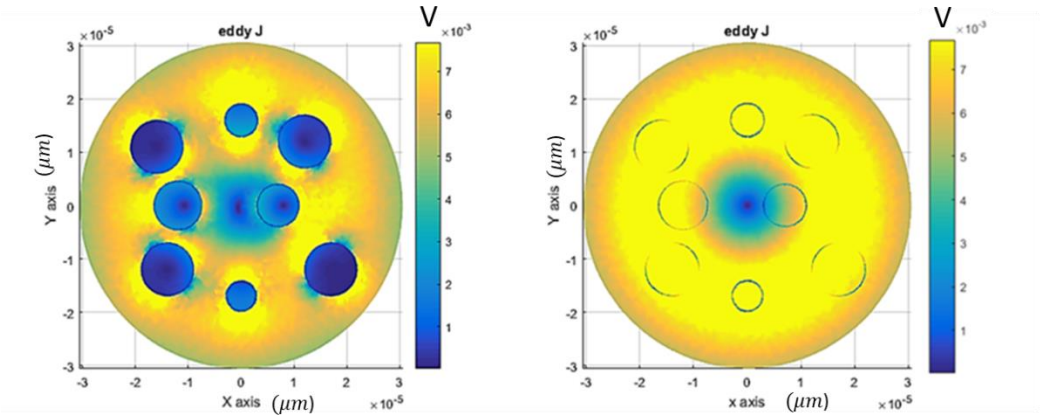

(a) Frequency 10 kHz (b) Frequency 10 MHz

Figure 4-6: Eddy current distribution of 3-D cell suspension model

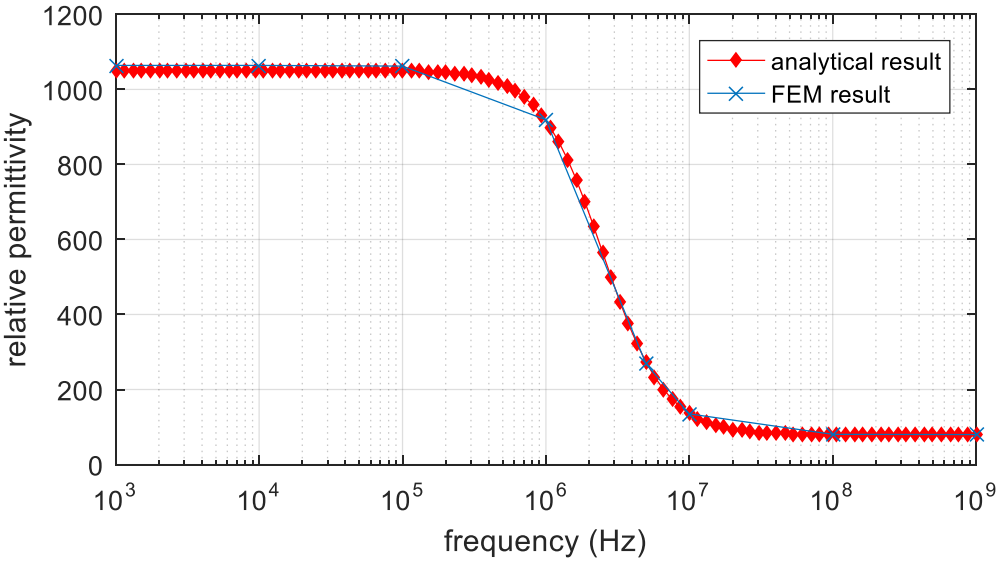

Figure 4-7: Permittivity spectroscopy of 3-D cell suspension

4.3 Cell shape deformation

According to Waxwell-Wagner equation, the volume fraction of cell in the cell suspension is a key factor that would influence the equivalent permittivity of

the suspension [4] [32] [41]. So when simulating the cell deformation, the volume fraction of the cell in cell suspension is assumed to be a constant. To keep the volume fraction as a constant, the volume of the cell is designed to be unchanged during the deformation process. Spherical model is deformed into an oval model while the volume of the cell keeps unchanged.

In two-dimension simulation, volume is represented by the area of the cell. The area of a circle is calculated by $S = \pi r^2$. The area of an oval is calculated by $S = \pi \mathrm{ab}$ where a is the length of the semi-major axis and b is the length of the semi-minor axis. Once the radius of cell is confirmed as r, the deformation just need to satisfy condition $r^2 = ab$.To eliminate the influence of position, all ovals and circles are centred at the same point. And all FEM simulations are carried out under the same meshing accuracy.

Because β-dispersion always occurs during the simulation and only the variation trend of the relative permittivity at low frequency is quite related to the shape of the cell model, a simulation about the cell model deformation is presented.

In 3-D simulation, cell shape should deform from sphere to ellipsoid, as shown in Figure 4-8. The volume still remains as a constant. The volume equation for sphere and ellipsoid model are: $V_{sphere} = \frac{4}{3}\pi r^3$ and $V_{ellipsoid} = \frac{4}{3}\pi abc$ where a, b and c are the axial length at x , y and z direction respectively. In order to simplify the deformation process, the axial length of y and z

directions are assumed to be the same ($b = c$). To keep the volume fraction a constant after the deformation, the axial length of x direction is: $a = \frac{r^3}{bc}$

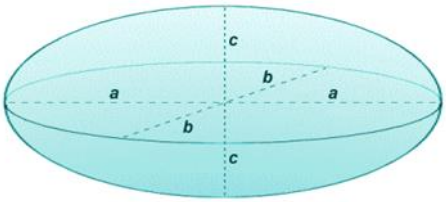

Figure 4-8: 3-D deformation model

4.4 2-D FEM simulations on deformations

In 2-D deformation simulations, the volume of spherical cell models and the deformed oval models are set to be the same to eliminate the influence of volume fraction. All cell models are centred at the same point in a cell suspension with applied electrical field on the top and bottom side of the cell suspension.

In order to observe how the deformation process influences the bio-impedance spectroscopy, the cell deformation progress is designed in two steps following the parameters in table 4.1. Firstly, the cell model deforms gradually from a sharp vertical oval to a sphere. Then it carried on deforming from the sphere to a horizontal sharp oval, as shown in Figure 4-9. The deformation parameters of the first and the second deformation process are symmetrical. The electric

potential distributions of the horizontal oval deformation model at low frequency (1 kHz) and high frequency (10MHz) are shown in Figure 4-10 and Figure 4-11 respectively.

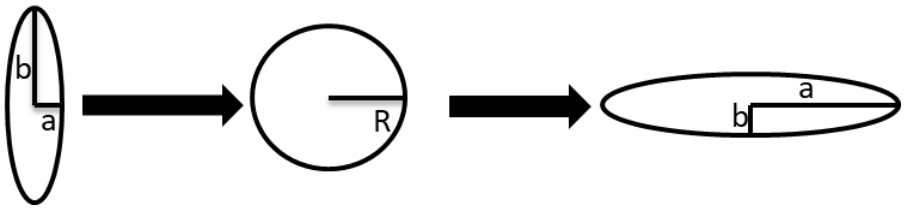

Figure 4-9 : Cell deformation progress

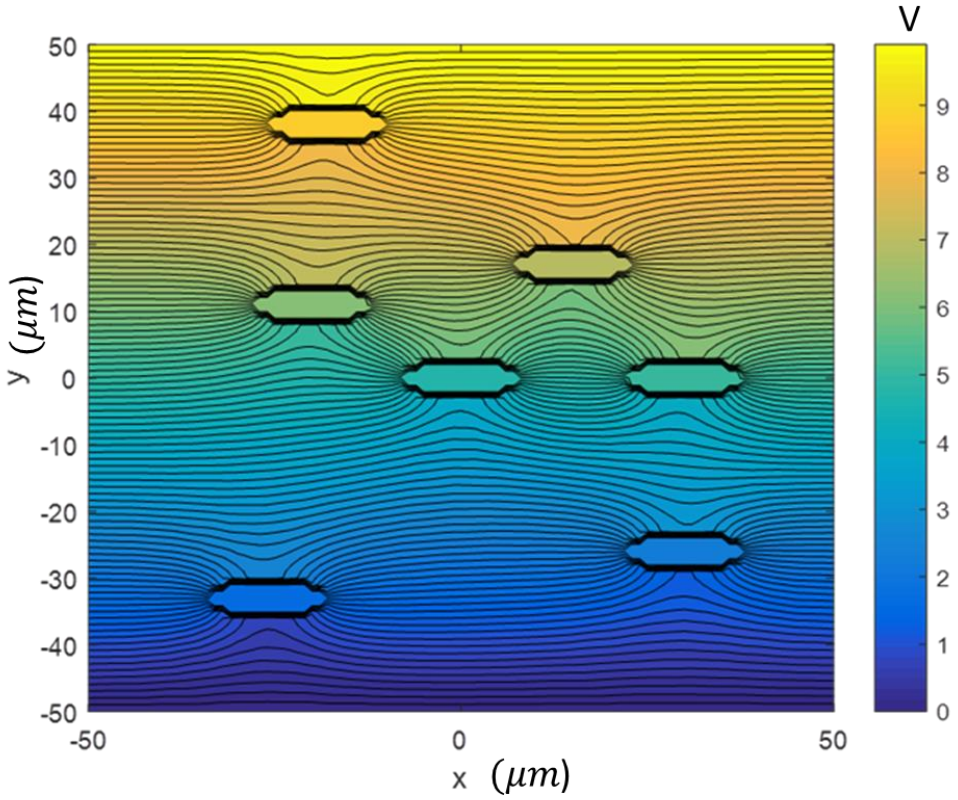

Figure 4-10: Electric potential distribution of deformation model at low frequency (1 kHz)

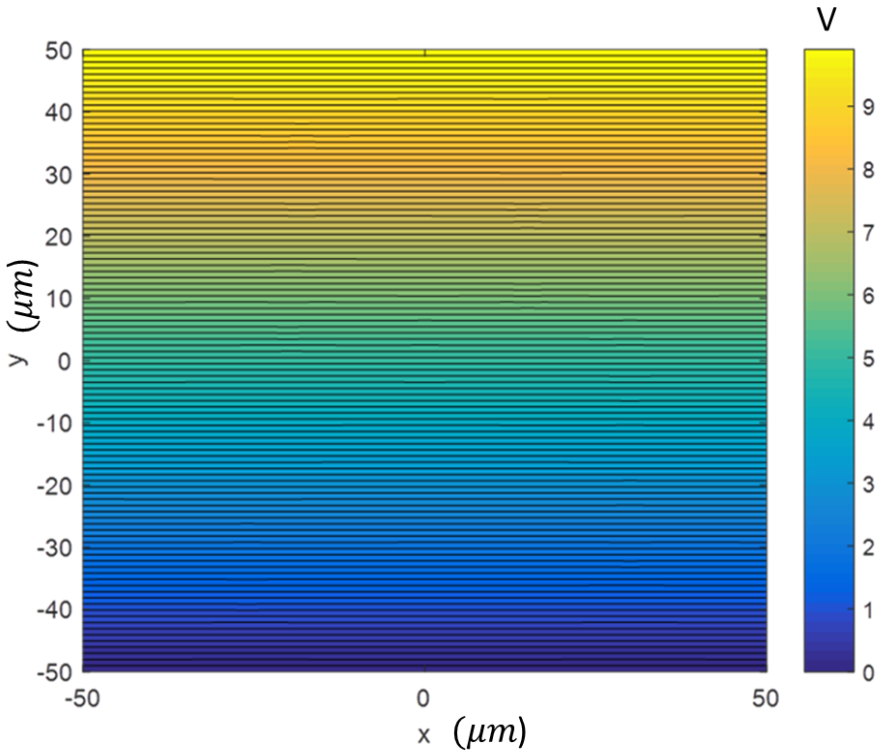

Figure 4-11: Electric potential distribution of deformation model at high frequency (10 MHz)

No matter what shape the cell is, it becomes electrically invisible at the high frequency and the relative permittivity converges to the same value at the high frequency as shown in Figure 4-11. For this reason, only the magnitude of β-dispersion (relative permittivity at the low frequency) is discussed for cell model deformation.

Table 4-1: 2-D deformation parameters (μm)

Deform order	1	2	3	4	5	6	7	8	9
Length of a	2	2.4	2.5	3	3.2	3.6	3.75	4	4.9
Length of b	12	10	9.6	8	7.5	6.67	6.4	6	4.9
Deform order	10	11	12	13	14	15	16	17	18
Length of a	4.9	6	6.4	6.67	7.5	8	9.6	10	12
Length of b	4.9	4	3.75	3.6	3.2	3	2.5	2.4	2

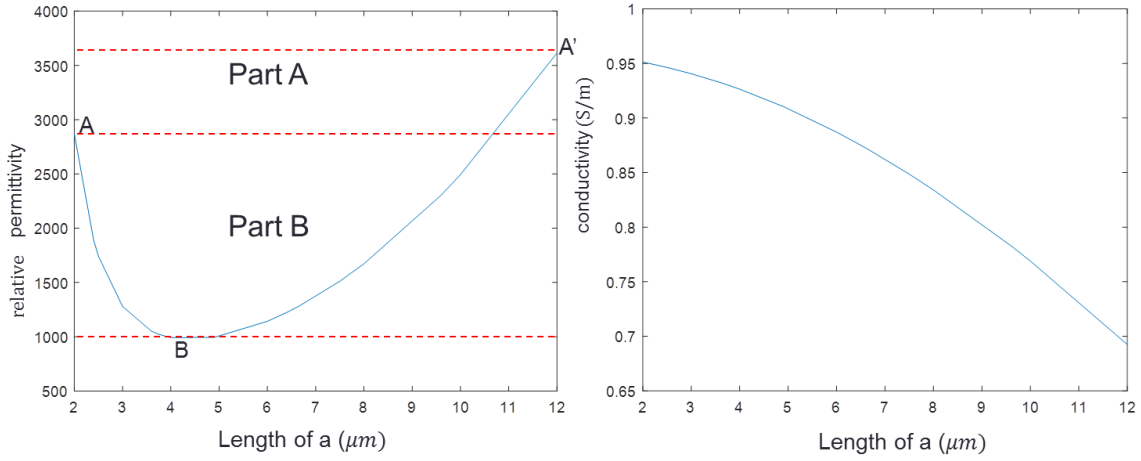

Figure 4-12: permittivity and conductivity at low frequency (1 kHz)

As shown in Figure 4-12, the conductivity decreases monotonically with increasing the length of a at the low frequency. This is easy to understand as the x-axis is vertical to the applied electric field, and with the longer x-axis length a is the more current will be blocked by the cells at the low frequency. However, the permittivity is not monotonic and not symmetric following the deformation process. In part A of Figure 4-12, comparing point A (a=2μm, b=12μm) and point A' (a=12μm, b=2μm), the relative permittivity of the vertical oval model (point A) is 2700 while the relative permittivity of horizontal oval model (point A') is 3600. The vertical and horizontal cell models have exactly the same shape parameters but different orientation. To validate the influence of the orientation on the magnitude of β-dispersion, further simulations were carried out. The simulation model was designed as a certain shape cell model centered at the same point. The only variate is the angle （θ）between the x-axis and the semi-major axis of the oval model.

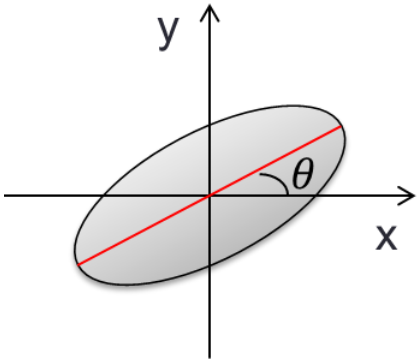

Figure 4-13: cell orientation model

The cell model rotates from horizontal to vertical with the angle θ between the x-axis and the semi-major axis of the oval model. The simulation result is shown in Figure 4-13, the value of angle θ is selected to be: $0^{\circ}, 30^{\circ}, 45^{\circ}, 60^{\circ}, 90^{\circ}$. It is obvious from the Figure 4-14 that the orientation of the cell would influence the magnitude of relative permittivity at low frequency. The relative permittivity decreases when θ increases. The orientation has little influence on the dispersion frequency range and magnitude of relative permittivity at high frequency. This simulation result verified and explained the difference between point A and A' in Figure 4-12.

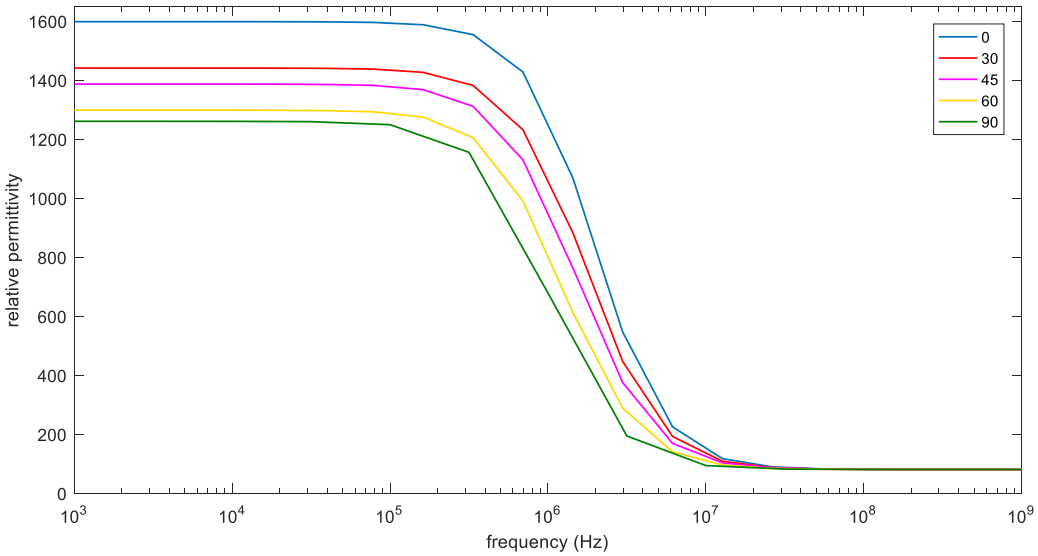

Figure 4-14: β −dispersion with different orientation ($\theta = 0^{\circ}, 30^{\circ}, 45^{\circ}, 60^{\circ}, 90^{\circ}$)

In part B of Figure 4-12, the magnitude of β-dispersion has large difference at point A (a=12μm, b=2μm) and point B (a=4.9μm, b=4.9μm). Asami introduced this phenomenon in his paper [51]. He considered the main factor that leads to magnitude difference of β-dispersion was the axial ratio (a/b). The oval model with large axial ratio (a/b) produces a β-dispersion with large magnitude. This agrees with our work that the magnitude of β-dispersion is large with a sharper oval model. However, in order to further analyse the mechanism of how axial ratio influence the magnitude of β-dispersion, we consider the influence of the membrane thickness (d) and the perimeter (c) of the cell model. To do so, a control group has been designed to investigate the influence of membrane thickness to perimeter ratio on the magnitude of β-dispersion. The control group is designed as the same shape of the cell while the membrane thickness was increased from 5nm to 10nm. As shown in Table 4-1, the

perimeter of the oval model increases with the increasing of axial-ratio a/b while the membrane thickness remains a constant during the deformation progress. As shown in Figure 4-12, the magnitude of relative permittivity increases with the increasing of perimeter to membrane thickness ratio c/d. The magnitude of relative permittivity is approximately proportional to the perimeter of deformed cell model, as shown in Figure 4-15.

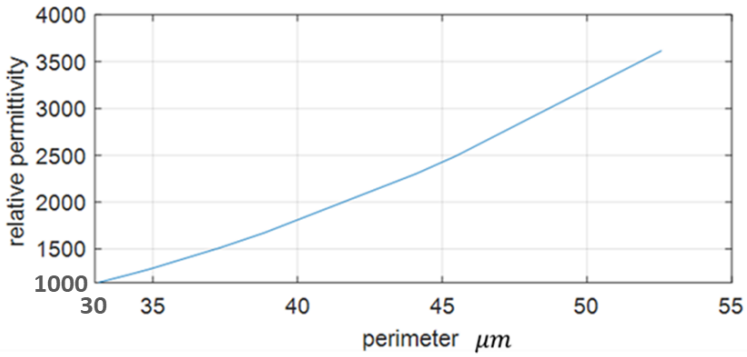

Figure 4-15: Magnitude of relative permittivity changes with perimeter of 2-D cell model

The result of control group is shown in Figure 4-16 and Figure 4-17. When the perimeter of cell model remain a constant and the membrane thickness increases from 5 nm to 10 nm, the magnitude of relative permittivity decreases to approximately 50%. It can be concluded that the magnitude of relative permittivity decreases with the decreasing of perimeter to membrane thickness ratio c/d.

The mechanism of how cell perimeter to cell membrane thickness ratio influences the magnitude of relative permittivity can be explained in the following discussion. The internal and external cell fluids are more conductive

than the membrane, so the membrane essentially forms a capacitance. Considering the basic function of capacitance:

$$C = \frac{\varepsilon S}{4\pi k d} \tag{4-4}$$

Here the perimeter of the cell can be regarded as the surface area S in two-dimension and the membrane thickness can be deemed as the capacitance plate distance d. So the cell perimeter to cell membrane thickness ratio can be equivalent to the ratio of S/d in the capacitance equation. When the cell perimeter to cell membrane thickness ratio increases, the whole cell model behaves more capacitive and thus the magnitude of relative permittivity at low frequency is increased.

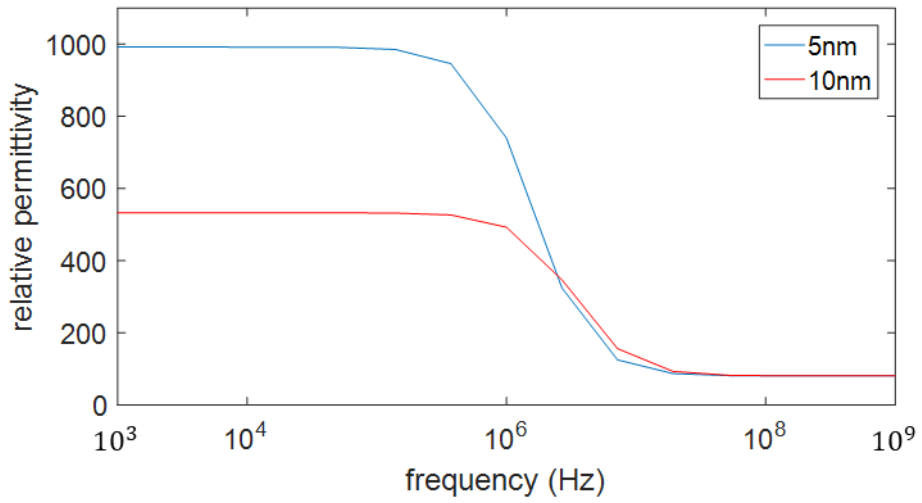

Figure 4-16: β-dispersion of shape Shape: a=4 μm , b=6 μm

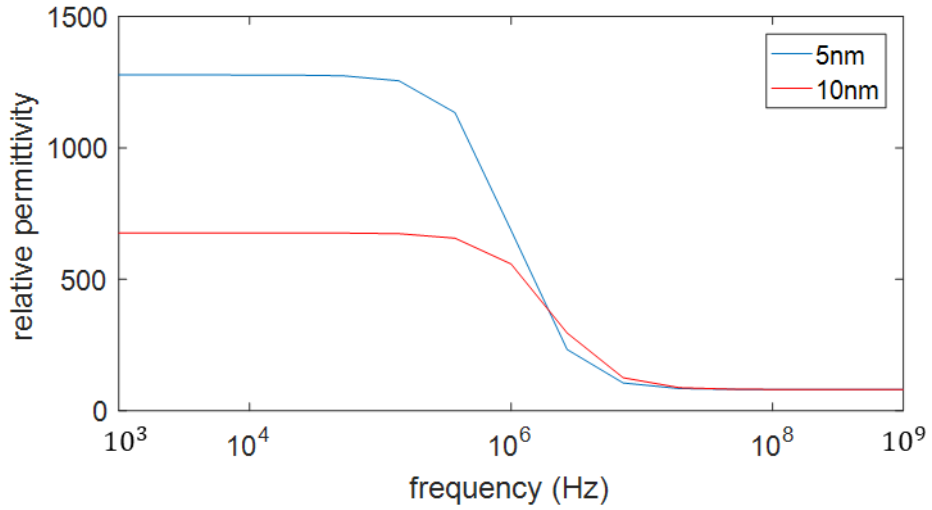

Figure 4-17: β-dispersion of shape Shape: a=3 μm , b=8 μm

4.5 3-D FEM simulation on deformation

As introduced in section 4.3, the deformation parameters of the 3-D ellipsoid model are designed as shown in Table 4-2. The original cell model is a spherical model with radius $\mathrm{R} = 5\ \mu\mathrm{m}$. To simplify the deformation process, the axis length of y and z direction are set to be the same ($b = c$), as shown in Figure 4-8. To keep volume fraction a constant after the deformation, the axial length of x direction is: $a = \frac{r^3}{bc}$.

Table 4-2: Deformation parameters for 3-D cell model

	a μm	b μm	c μm	Surface area (μm^2)
Sphere	5	5	5	314.0
Group1 (scale 1.5)	5*1.5	$5/\sqrt{1.5}$	$5/\sqrt{1.5}$	332.9

Group2 (scale 2)	5*2	$5/\sqrt{2}$	$5/\sqrt{2}$	365.8
Group3 (scale 3)	5*3	$5/\sqrt{3}$	$5/\sqrt{3}$	434.2

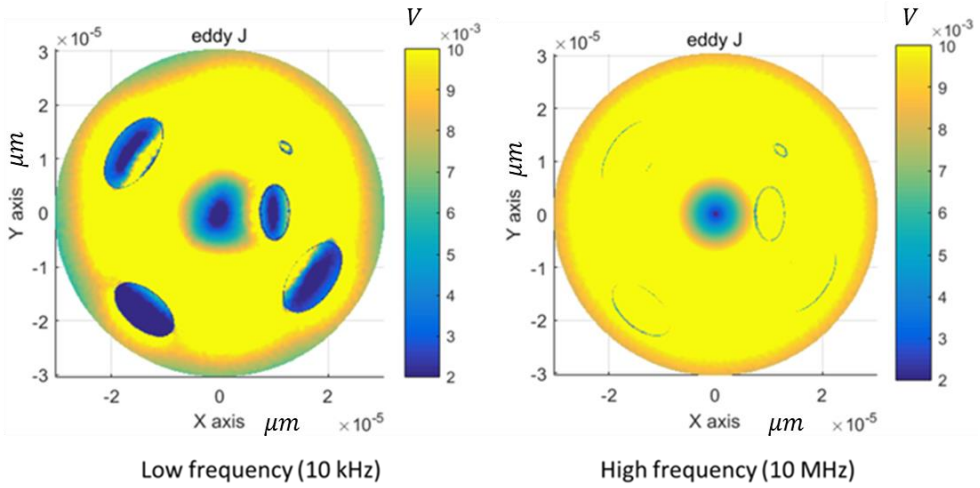

Figure 4-18: Eddy current distribution of 3-D ellipsoid deformation model

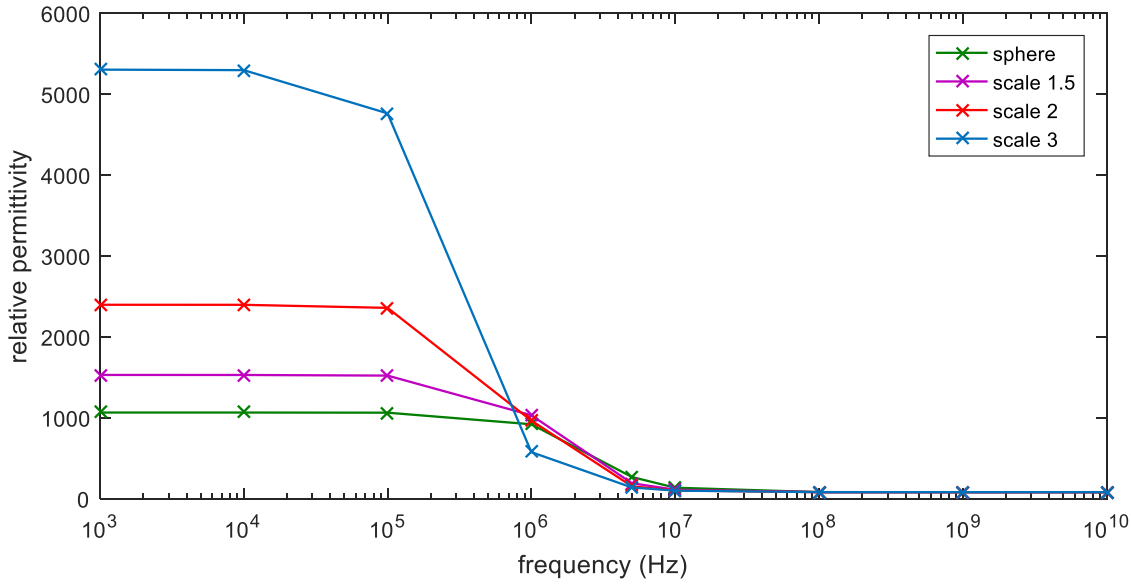

Figure 4-19：Relative permittivity of cell suspension with different deformation shape

The membrane thickness is constant d=5 nm. There are 4 groups of simulations with surface area (S) increasing from sphere to ellipsoid as shown

in Table 4-2. The axial length of x-axis direction is designed to be $a, 1.5a, 2a, 3a$ for each simulation group. The corresponding axial length of y and z direction is calculated to keep the volume of cell as a constant. The eddy current distribution of the second group in Table 4-2 (the axial length of x direction is $1.5a$) is shown in Figure 4-18. Figure 4-18 shows that the deformed cell model is non-conductive at low frequency and becomes electrically invisible at high frequency, which agrees with the previous simulation result in section 4.2. The spectroscopy of the relative permittivity of 4 deformation simulation groups is shown in Figure 4-19. The result in Figure 4-19 shows the same trend with the result of 2-D deformation simulation. As shown in Figure 4-19, with the sphere deformed to a sharper ellipsoid with a larger surface area, the magnitude of the relative permittivity is increased. Another two control group was set to validate the influence of the surface area to membrane thickness ratio. In the control group, the shape of the cell model is set to be the same and the membrane thickness increased from 5 nm to 10 nm. It can be obtained from Figure 4-20 and Figure 4-21 that the permittivity reduces with increasing membrane thickness. Because the number of mesh elements is too large (about $1.2 * 10^6$) and the calculation capacity of Matlab is limited, there are only 10 data points simulated over the frequency range of each dispersion. The 3-D membranes thickness simulation results match the 2-D results which indicate that the magnitude of the relative permittivity at low frequency increases with the increase of surface area to membrane thickness ratio. This

can be explained by the basic equation of capacitance $C = \frac{\varepsilon S}{4\pi k d}$. In 3-D cell model, the ratio of $\frac{S}{d}$ in the capacitance equation is the same with the surface area to the membrane thickness ratio. So when the surface area to the membrane thickness ratio increases, the cell model behaves more capacitance and thus the magnitude of relative permittivity increases.

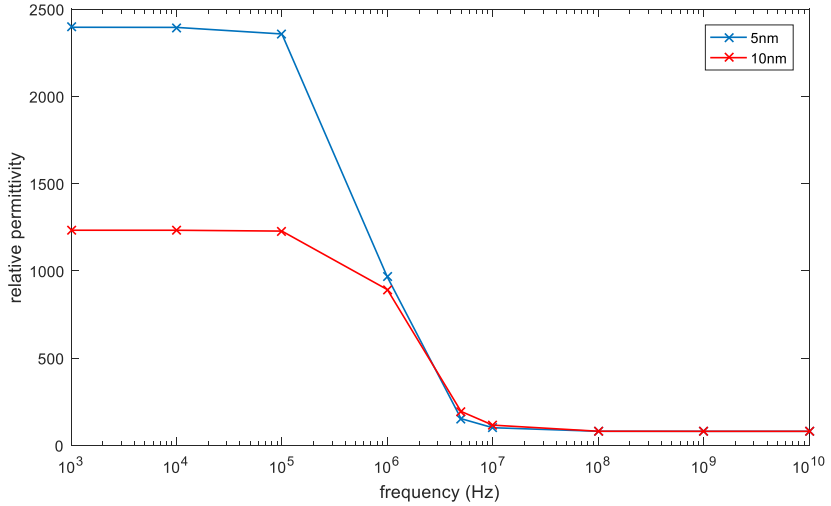

Figure 4-20: permittivity of parameter scale 2 with different membrane thickness

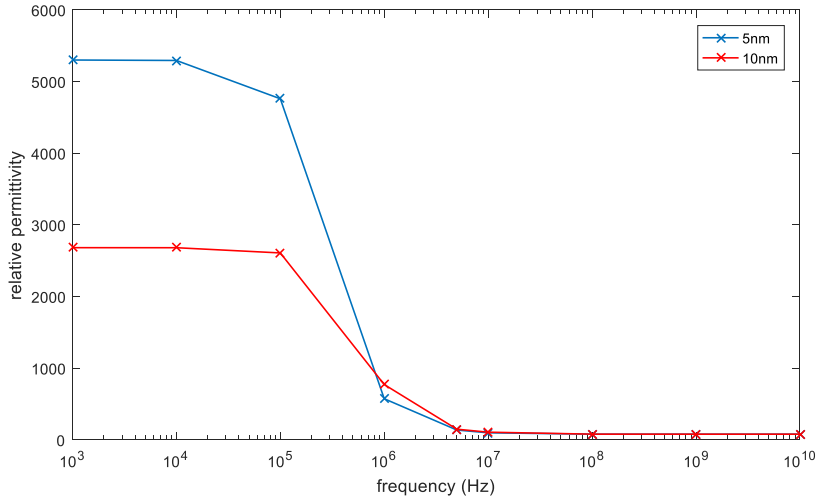

Figure 4-21: permittivity of parameter scale 3 with different membrane thickness

4.6 Summary

This Chapter discussed the influence of cellular structure, including cell shape, cell orientation and membrane thickness, on bio-impedance spectroscopy. The simulation works are based on finite element method. The results of simulation works can be concluded as:

1) The oval cell model with less orientation angle towards the applied field / current direction exhibits β-dispersion with smaller magnitude than that of the oval models with larger orientation angle towards the applied field/ current direction.
2) The magnitude of relative permittivity of β-dispersion increases with the increasing of cell perimeter / surface area to membrane thickness increases.

5 Mechanism of frozen-thawed effect analysed by contact electrode measurements and 2-D Finite Element Method

5.1 Simulation model

In this section, we designed a simulation model to simulate the integrity of cell membranes. The original model for the normal cell is the single shell model according to Asami [4]. The spherical cell model is shown in Figure 3-1.

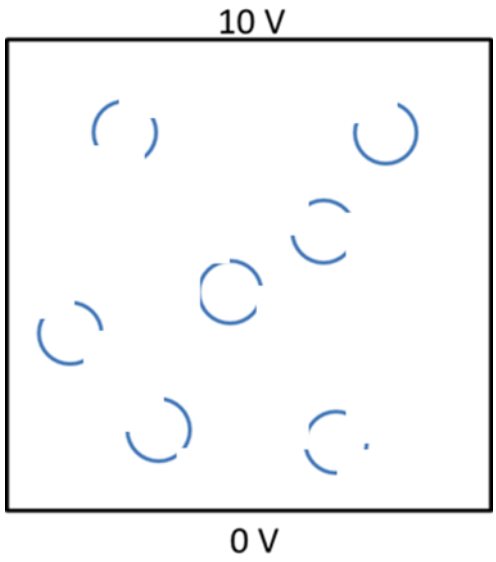

Figure 5-1: Disintegrate membrane modelling

As the membrane is composed of lipid bilayer, its conductivity is extremely low. However, cell membrane becomes permeable after cell death mainly due to pores on membrane (structure of the membrane), not the membrane in terms of its material property. The pores enable the current to flow, which makes the membrane of dead cell has an apparent high conductivity (equivalent conductivity). So the dead cell model in our study is designed as a low

conductivity membrane with pores which allows current flow through the break points on the membrane. The main idea of the designed simulation model is to add break points on the cell model to simulate ruptured membranes. The break points are placed randomly on the cell model. The electrical parameters of the intracellular and extracellular fluid are set to be the same values. The conductivity and permittivity of the membrane model remain unchanged. The designed simulation model is shown in Figure 5-1, some break points are added so that the results can be compared with the original model.

5.2 Sample preparation

5.2.1 Saline solutions

The saline solutions were prepared by mixing salt (NaCl) and distilled water. The conductivity of mixed saline solution was measured by a conductivity meter. Two sets of saline solutions were created with conductivity of 3 S/m and 5 S/m respectively. The container of the saline solution is a 2L vessel with internal height of 20 cm.

5.2.2 Biological samples

Fresh potato and fresh loin pork are selected as the biological samples for the BIS measurement. The potato and loin pork are tested temperature between 14 ˚C - 15 ˚C immediately after bought from the local store. The tested samples were frozen for 24 hrs between -5 ˚C - -6 ˚C and thawed for 12 hrs at

room temperature between 14 ˚C - 15 ˚C. The frozen-thawed food samples were tested under room temperature between 14 ˚C - 15 ˚C.

5.2.3 Microscopic slides

The microscopic slides of the frozen-thaw food samples (loin pork and potato) were prepared immediately after the measurement of the BIS. The thickness of the micro-section of food sample is 10 μm. The microscopic slides were stained by PI stainer and preserved in aseptic container. The microscopic observation experiment was conducted immediately after the preparation of the microscopic slides.

5.3 Methods

5.3.1 Impedance measurement set up

The four-terminal method was used to minimise electrode polarisation. Impedance analyser Solatron 1260 was used to measure the impedance. The effective area of the measurement electrodes is $S = 2\ cm * 3\ cm = 6\ cm^2$, and the distance between the electric field measuring electrodes is $L = 6.6\ cm$. The conductivity can then be calculated by $\sigma = 1/\rho = L/RS$. R is the real part of the measured impedance, ρ is the resistivity. The measurement samples are the saline solution, fresh potatoes, and frozen-thawed potatoes that have been stored in the freezer for 24 hrs. This measurement is to check the influence that freezing has on the impedance spectroscopy of potatoes.

5.3.2 Microscopic observation

Fresh potatoes and pork were obtained from local stores. The potatoes and pork were divided into two groups; one group is frozen for 24 hrs at -6℃ and then frozen-thawed for 12 hrs at room temperature 15℃ before use but the other group is not frozen. The potato and pork slide was made immediately before experimentation. PI (Propidium Iodide [Jones and Senft, 1985]) stain is prepared by mixing distilled water with weight ratio 1:1. As introduced in section 2.5.3, the PI stain was used to check the integrity of cell membranes as the integrated membranes of living potato cells can prevent the PI stain from dyeing the starch grain and DNA within the cell. The microscope type is Zeiss-Axio scope A1 which can take a snapshot of fluorescent images. The control experiment is also divided into two groups: the control group is fresh potato and fresh pork slides stained with Propidium Iodide and the experiment group is the frozen-thawed potato and frozen-thawed slides stained with Propidium Iodide. Snapshots were taken directly from the Zeiss-Axio scope A1.

5.4 Results and discussion

5.4.1 Electrode measurement of potato impedance

As shown in Figure 5-2, the conductivity of fresh potatoes presents a dispersion ranging from 10 kHz to 10 MHz, which is in the range of β-dispersion. However, the conductivity of the frozen-thawed potatoes shows a dispersion starting at 10 Hz, which is in the range of α-dispersion. According to Schwan, α-dispersion is caused by the relaxation of ion flows and β-dispersion is due to Maxwell-Wagner's effect [71] [72]. To identify the frequency range of the dispersion, a measurement of saline solution is carried out as shown in Figure 5-2 (a). The saline solution is made by mixing salt (from a local market) and tap water, and the concentrate of the solution is 5%. The saline solution only exhibits α-dispersion caused by ion flows. As shown in Figure 5-2 (a), the dispersion starts at 10 Hz and ends at around 10 kHz, which is the same as the results of the frozen-thawed potatoes. The spectroscopy of saline solution and frozen-thawed potatoes both show flat curves over the frequency range of 10 kHz to 10 MHz. This result agrees with the previous work on frozen-thawed samples [73] [74].

Given the measurement result can be influenced by many factors including measurement error, sample differences and operating error, the measurements were repeated several times to eliminate the accidental error.

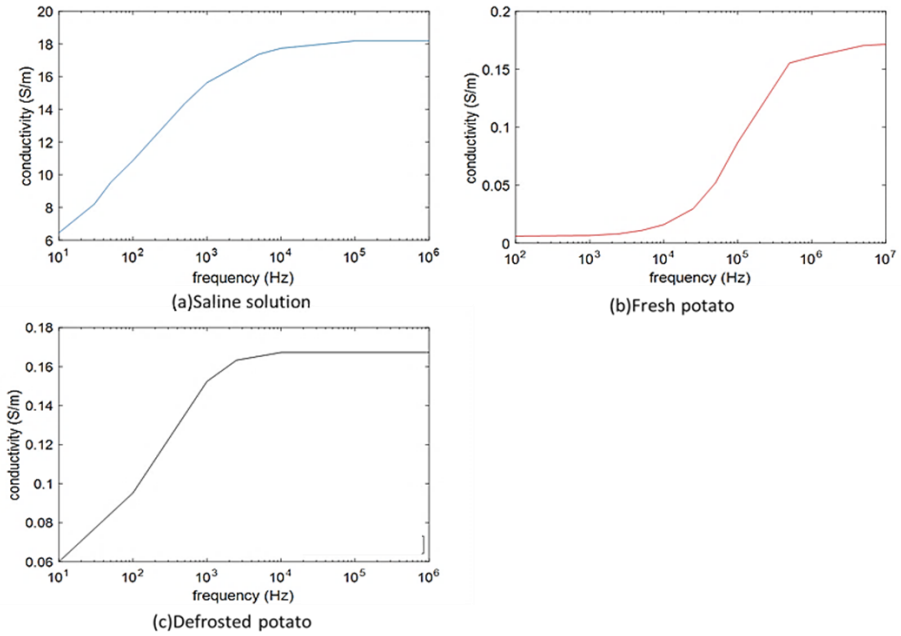

Figure 5-2: Measurement results of the contact electrode method

The results illustrate that the characteristics of the impedance spectroscopy of frozen-thawed potatoes mainly refers to ion flows, and that the Maxwell-Wagner effect caused by the low conductive membrane is significantly small. We can assume that the membranes of the frozen-thawed potatoes have been ruptured and can no longer block ion flows, so the conductivity of the frozen-thawed potatoes can only exhibit an α-dispersion. The Maxwell-Wagner effect, caused by the interfacial polarisation of cell membrane, is minimised due to the ruptured membranes. A microscopic experiment and an original FEM simulation model are designed to verify the assumption.

5.4.1.1 Microscopic experiment of potato cell

The stainer used is PI which can stain DNA inside cells. As living cell membrane is semipermeable and blocks PI, propidium Iodide is commonly used as a stainer to identify membrane integrity. The results of the microscopic experiment are shown in Figure 5-3. In Figure 5-3 (a), the shape and structures of fresh potato cell can be observed clearly including cell walls (dark lines) and vacuole (the blob with dark edge and bright centre). The radius of the cell is approximately 7.5 μm based on the scale shown in Figure 5-3 (a). However, in Figure 5-3 (b), there is no obvious boundary of the frozen-thawed potato cell since the cell wall and membranes are ruptured. The stained grains in Figure 5-3 (b) are the starch grains inside the potato cell and the radius of the starch grains is approximately 2.5 μm. There are obviously stained fluorescence grains in Figure 5-3 (b) while no visible stained objects can be observed in Figure 5-3 (a). This indicates that the fresh potato samples are not stained by PI while the frozen-thawed potato samples are distinctly stained. This is because a living and integrated potato cell membrane can block PI whereas a ruptured potato cell membrane cannot. And there are starch grains within the potato cells which can be stained by PI and observed under fluorescent microscope. The results show that the membranes of frozen-thawed potatoes are ruptured and can no longer prevent PI from dyeing the starch grains within the potato cells.

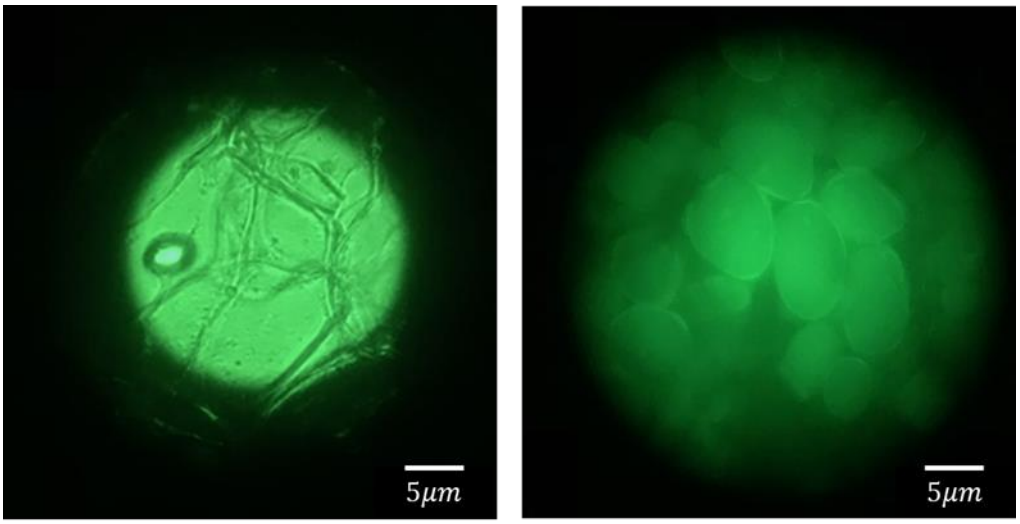

Figure 5-3: Microscopic result of (a) fresh potato (b) frozen-thawed potato

5.4.1.2 Ruptured simulation model of potato impedance

The conductivity of intra and extra cellular fluid is set to be 0.15 S/m according to the measurement result. The volume fraction of cell suspension is set to be 0.8. The parameters of membrane are selected according to Asami [4]. The simulation results are shown in Figure 5-4 and Figure 5-5(b). Figure 5-4 shows the electric field distribution of the system which indicates that the current can flow through the ruptured cells at a lower frequency.

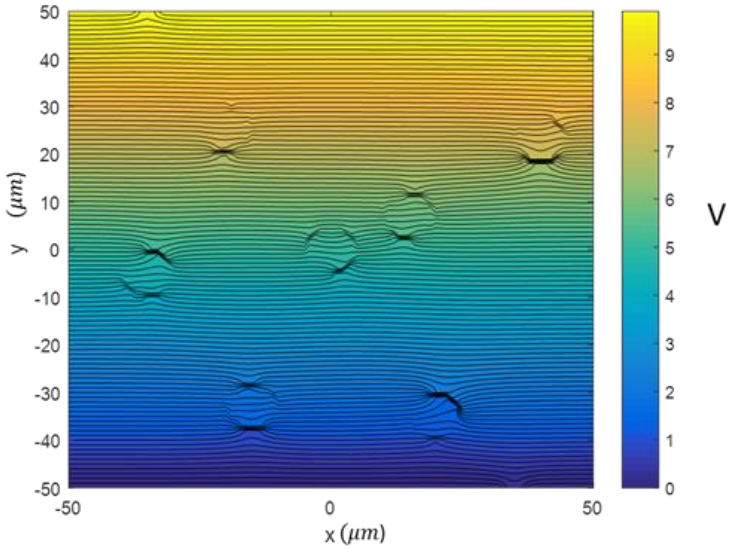

Figure 5-4: Electric potential distribution of frozen-thawed model

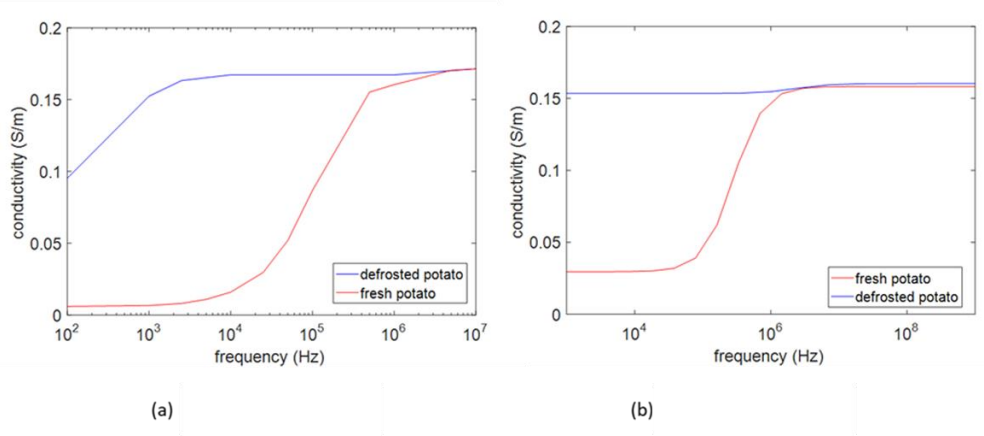

Figure 5-5: Conductivity spectroscopy of (a) Measurement result (b) Simulation result

In Figure 5-5, the conductivity of the ruptured potatoes is higher than fresh potatoes at a lower frequency. And the dispersion frequency of the ruptured potato is lower than that of the fresh potato. However, the conductivity of both ruptured and fresh potatoes converges to the same value at a higher frequency. These characteristics are the same as the results obtained from the electrode method measurement, which means that the designed FEM simulation model is suitable for the electrode method measurement. The

difference between the simulation and measurement results is that, due to the limitation of the FEM method, α-dispersion, caused by ion flows, cannot be simulated. So the impedance spectroscopy of ruptured potatoes cannot present α-dispersion at a lower frequency, as shown in Figure 5-5. However, the main characteristics of the simulation results are the same as the results obtained from the electrode method measurement. This means that the designed FEM simulation model is verified by the electrode method measurement.

5.4.2 Electrode measurement of pork impedance

5.4.2.1 Microscopic experiment of pork cell

Figure 5-6 (a) is the normal pork cell. The dotted line circles the approximate shape of a single cell. Inside this cell, there is no stained object. The shape is not distinct because the pork cell has no cell wall comparing to potato cell, therefore, the cell shape of pork is hard to be maintained in the microscopic view. Figure 5-6 (b) shows the stained frozen-thawed cell. The shape of the frozen-thawed cell cannot be distinguished since the membrane is ruptured and there is no obvious boundary for each cell. The bright spots inside the frozen-thawed cells are the stained DNAs. It is obvious that the fresh pork cell is not stained by PI while the frozen-thawed pork cell is distinctly stained.

These indicate that the membrane of frozen-thawed pork cell is ruptured and cannot block PI stainer while the membrane of fresh pork is integrate.

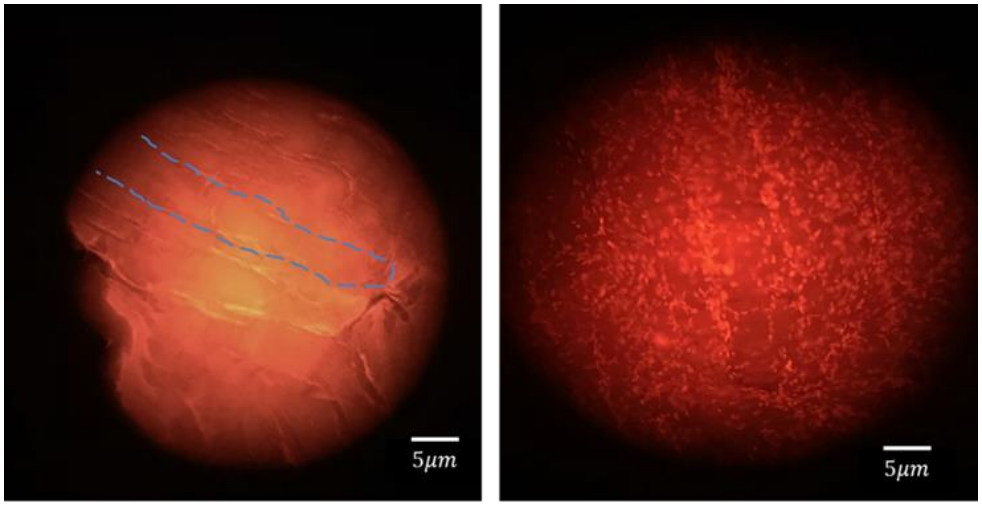

Figure 5-6: Microscopic result of (a) fresh loin pork (b) frozen-thawed loin pork

5.4.2.2 Measurement and simulation result of pork impedance

BIS measurements of fresh and frozen-thawed pork were carried out using four-terminal contact method. The electrodes were contacted with the fresh and frozen-thawed pork directly. Normal saline with 0.9% concentration was added between the electrodes and the pork to ensure good electrical connection. The impedance spectra were measured by Solatron 1260 impedance analyser.

The frozen-thawed pork only exhibits a α-dispersion starting at around 100 Hz and ending at 10 kHz (Figure 5-7(a)). After 10 kHz, the conductivity remains unchanged with frequency and there is no obvious dispersion. The impedance

spectra of saline solution (Figure 5-2 (a)), which theoretically only exhibits α-dispersion, shows a similar result with the frozen-thawed pork. However, for the fresh pork, the most significant conductivity dispersion frequency is ranging from 50 kHz to 10 MHz which is in the range of β-dispersion. The fresh pork exhibits a complete β-dispersion while the frozen-thawed pork only exhibits an α-dispersion. This indicates that the Maxwell-Wagner effect is eliminated on the frozen-thawed pork.

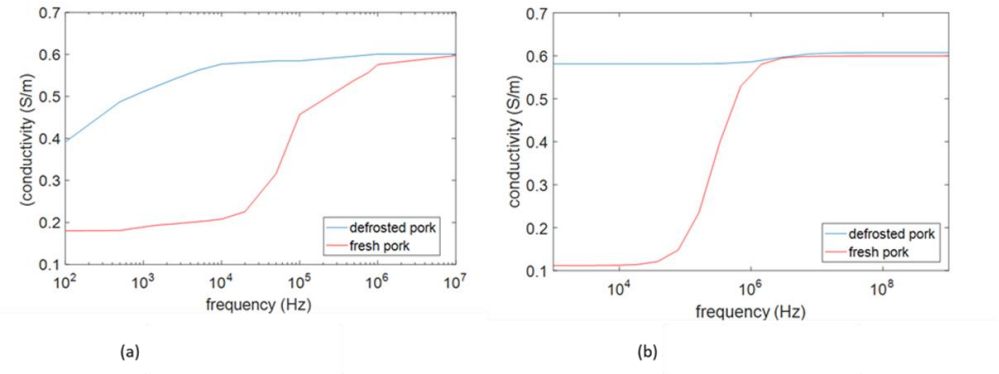

Figure 5-7: Conductivity spectroscopy of (a) measurement result (b) simulation result

The simulation results were carried out based on the model shown in Figure 5-1. The conductivity of intracellular and extracellular fluid is set to be 0.6 S/m which is close to the measurement result. The volume fraction is set to be 0.8. α-dispersion cannot be observed on the simulation result as α-dispersion cannot be simulated. However, the simulation result still shows the same characteristics with the measurement result. The conductivity of frozen-thawed pork is higher than fresh pork at low frequency and converges to the same value at higher frequency. The fresh pork exhibits β-dispersion ranging from 10 kHz to about 10 MHz while frozen-thawed pork shows no significant

dispersion on the frequency range. In conclusion, the ruptured cell model has successfully simulated the electrical characteristics of frozen-thawed pork.

In general, the measurement result verifies the simulation result of the ruptured cell model. The membrane of the frozen-thawed potato and pork is ruptured according to the microscopy experiment results. These indicate that the assumption is verified and can therefore be summarised as follows: the membranes of the frozen-thawed potato cells are ruptured; and the ruptured membranes reduce the influence of the Maxwell-Wagner effect. The effect of the frozen-thaw injury on impedance spectroscopy of potatoes is mainly caused by ruptured cell membranes.

5.5 Summary

This chapter analysed the mechanism of how frozen-thaw injury influences the impedance spectroscopy of potatoes. We assumed that the frozen-thaw injury mainly influences the impedance spectroscopy of a potato by breaking its cell membrane. In light of this assumption, an originally designed FEM model was identified and a microscopic experiment was then carried out, which successfully verified this assumption. The measurements were repeated several times to make sure there are no random results. We can therefore

conclude that frozen-thaw injury breaks the cell membrane of a potato, reducing the β-dispersion on the impedance spectroscopy of potatoes.

6 Mechanism of frozen-thaw effect analysed by non-contact induction measurements and 3-D Finite Element Method

6.1 Measurement set up and sample preparations

6.1.1 Measurement set up

6.1.1.1 Measurement system

A front end circuit is design to measure the change of conductivity and permittivity at frequency domain. There are mainly five parts of the circuit: signal generator, power amplifier, transmitter and receiver and a Zurich lock-in amplifier as shown in Figure 3-3 and Figure 3-4.

The whole system is running at the following way: a sinusoidal wave is generated by the signal generator (Zurich lock-in amplifier) and amplified by the power amplifier. The amplifier input a high current to the transmit coil. And the current generates a magnetic field which would induce eddy currents in the tested cell suspension. The eddy currents would generate a second magnetic field which is detected by the receiver coil [38] [39]. This signal is obtained by Zurich lock-in amplifier and stored into PC. The impedance of the cell suspension influences the magnitude and phase of the signal detected by the receive coil. And in turn, the equivalent impedance of the suspension can be calculated by comparing the signal detected by the receiver and the transmitter. The receive coil is connected in opposite directions so that the magnetic field

induced by the same excitation is cancelled. And the receive coil only detects the magnetic field induced by cell suspension when the system is balanced [38].

The measurement at each frequency has been repeated 100 times to obtain the average value and increase the SNR of the results. The measurement was repeated several times to eliminate the accidental error.

6.1.1.2 Electrical conductivity measurement

As introduced in chapter 3.4, the measurement result is related to the conductivity and permittivity of suspension following the equation [39]:

$$\frac{\Delta V}{V} = Pf\mu_0(2\pi f\varepsilon_0\varepsilon_r - j\sigma) + QX \quad (6\text{-}1)$$

P is a constant of volume factor which is calibrated by saline solution with certain conductivity. f is the frequency. ε_0, μ_0 are the permittivity and permeability of vacuum respectively. σ , ε_r and X are the electrical conductivity, relative permittivity and magnetic susceptibility of the sample. ∆V is the detected electromotive force from receive coil while V is the excitation from the transmit coil. It can be obtained from the equation that conductivity is proportion to the imaginary part of $\frac{\Delta V}{V}$ and permittivity is proportion to the real part of $\frac{\Delta V}{V}$ [O'Toole et al, 2015]. The conductivity can be derived as:

$$\sigma = -\frac{Im\left(\frac{\Delta V}{V}\right)}{Pf\mu_0} = K\frac{Im\left(\frac{\Delta V}{V}\right)}{f} \quad (6\text{-}2)$$

where $K = \frac{-1}{P\mu_0}$ and K is a constant. The constant K can be calibrated by measuring saline solutions with certain conductivity.

6.2 3-D simulation model

6.2.1 Custom cellular parameters for FEM simulations

The spherical cell model is shown in Figure 3-1. According to Asami [4] [47], the electrical parameters of the cell model are:

$$\varepsilon_m^* = \frac{\sigma_m^*}{j\omega\varepsilon_0} = \frac{k_m + j\omega\varepsilon_m\varepsilon_0}{j\omega\varepsilon_0} \quad (6\text{-}3)$$

$$\varepsilon_c^* = \frac{\sigma_c^*}{j\omega\varepsilon_0} = \frac{k_c + j\omega\varepsilon_c\varepsilon_0}{j\omega\varepsilon_0} \quad (6\text{-}4)$$

$$\varepsilon_a^* = \frac{\sigma_a^*}{j\omega\varepsilon_0} = \frac{k_a + j\omega\varepsilon_a\varepsilon_0}{j\omega\varepsilon_0} \quad (6\text{-}5)$$

6.2.2 Frozen-thawed cellular model

The frozen-thaw injury damages the cell membranes. Therefore, the frozen-thawed cellular model is designed as a original custom cellular model with disintegrate membranes as shown in Figure 6-1. The cylinder in Figure 6-1 stands for the cell suspension (mixing of cellular fluid and frozen-thawed cell). The membrane of the frozen-thawed cellular model is ruptured, the intra and extra cellular fluid are mixed as one fluid. The conductivity and permittivity of intra and extra mixing fluid of frozen-thawed are 1 S/m and 80 respectively. The other electrical parameters of the frozen-thawed cellular model are set to be the same with custom cellular model. This model is aimed at simulating the influence of disintegrate membranes on bio-impedance spectroscopy.

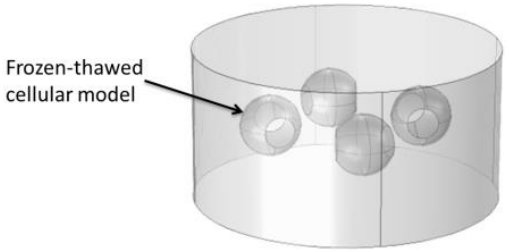

Figure 6-1: 3-D frozen-thawed cell suspension model

6.2.3 Calculation of equivalent complex conductivity

A new method of calculating equivalent complex conductivity of cell suspension along eddy current direction is introduced.

The eddy current density flows in the suspension should be

$$J^{(i)} = \sigma^{(i)} E^{(i)} \tag{6-6}$$

where $E^{(i)}$ denotes the vector sum of the electrical field on all the edges of each tetrahedral element. $\sigma^{(i)}$ is the complex conductivity parameter (with real part the conductivity and imaginary part related to the permittivity) of the of each tetrahedral element.

Assuming there is another background suspension with uniform dielectric and the suspension has exactly the same shape with simulated cell suspension. This uniform suspension is named equivalent model.

Since the normal component of E-field relative to each cylindrical cross-section surface is identical throughout the whole target, then

$$\sum \vec{n} \cdot E^{(i)} = \sum \vec{n} \cdot E_s^{(i)} \quad (6\text{-}7)$$

where, $E_s^{(i)}$ denotes the background E-field of the of each tetrahedral element (equivalent model); $\vec{n}$ is the normal unit vector relative to the surface of target; Since the equivalent suspension has uniform properties, the electrical background field $E_s^{(i)}$ is vertical to the cylindrical cross-section surface. Then the equivalent complex conductivity of the original suspension (arranged cells within the suspension) can be deduced from (12) and (13) that

$$\sigma_s = \frac{\sum J_s^{(i)}}{\sum \vec{n} \cdot \frac{J^{(i)}}{\sigma^{(i)}}} \quad (6\text{-}8)$$

$\sigma^{(i)}$ is the complex conductivity of each tetrahedral element. $J_s^{(i)}$ is the eddy current density through each cylindrical cross-section of equivalent suspension model. $J^{(i)}$ is the eddy current density through each cylindrical cross-section of the original suspension model with arranged cells. The current flow direction $\vec{n}$ on each cylindrical cross-section surface is shown in Figure 6-2. The direction can be easily derived:

$$\vec{n} = (\sin(\theta), -\cos(\theta)) \quad (6\text{-}9)$$

where $\theta = tan^{-1}\left(\frac{y}{x}\right)$. x and y are the coordinates of the nodes on x −axis and y −axis respectively.

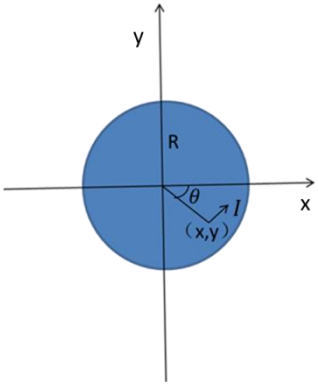

Figure 6-2: current flow direction (top view of cell suspension model)

Then the complex conductivity can be calculated based on equation (6-8) and the permittivity is simply dividing the imaginary part by $j\omega\varepsilon_0$.

6.3 Results and discussion

6.3.1 Measurement result of fresh samples

The biological samples are fresh loin pork and fresh potato (obtained from local store). The conductivity of the samples is calculated by equation (3-19). The value of constant K is calibrated by measurements with 3 S/m and 5 S/m saline solutions. Since the value of K has error on different frequencies, it is calculated at each sampling frequency to improve the accuracy of the conductivity measurement.

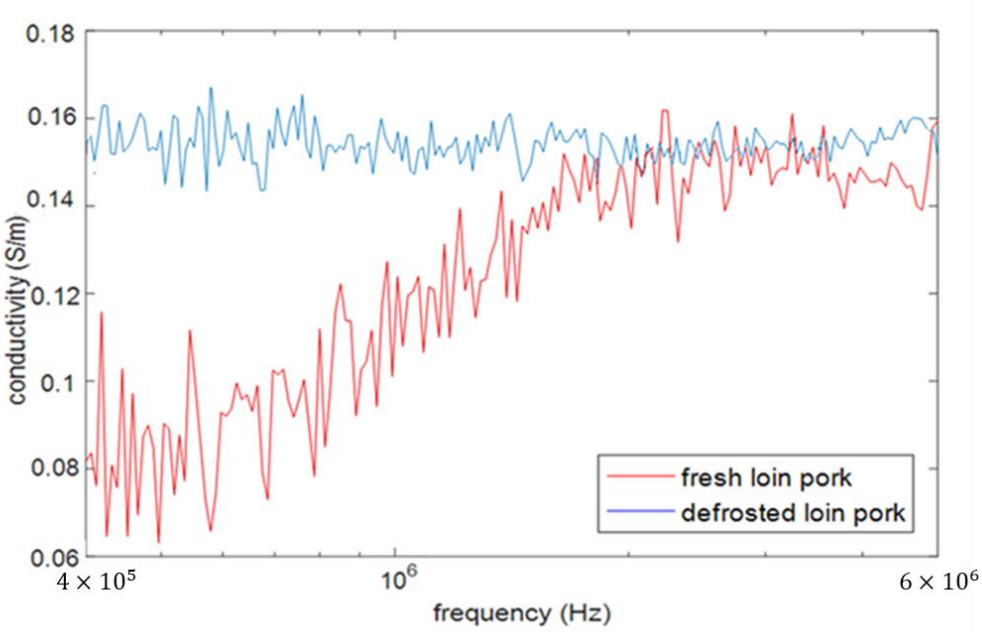

Figure 6-3: Conductivity spectroscopy of loin pork

In the first test we measured the fresh food group as a control group. The measurement at each frequency has been repeated 100 times and the average value is plotted in Figure 6-3 and Figure 6-4. The conductivity of fresh loin pork is stable at lower frequency and higher frequency and the dispersion frequency is ranging from 800 kHz to 3 MHz (Figure 6-3). The curve is in reasonable agreement with β-dispersion. For the conductivity spectra of fresh potato, the β-dispersion is ranging from 400 kHz to about 2 MHz (Figure 6-4). The measurement accuracy is 0.01 S/m and signal to noise ratio (SNR) is 15. Both fresh potato and fresh loin pork samples exhibit clear β-dispersion which is the basic electrical characteristic of living bio-tissues. The results agree with published works such as Barai and Michael [38] [39] .

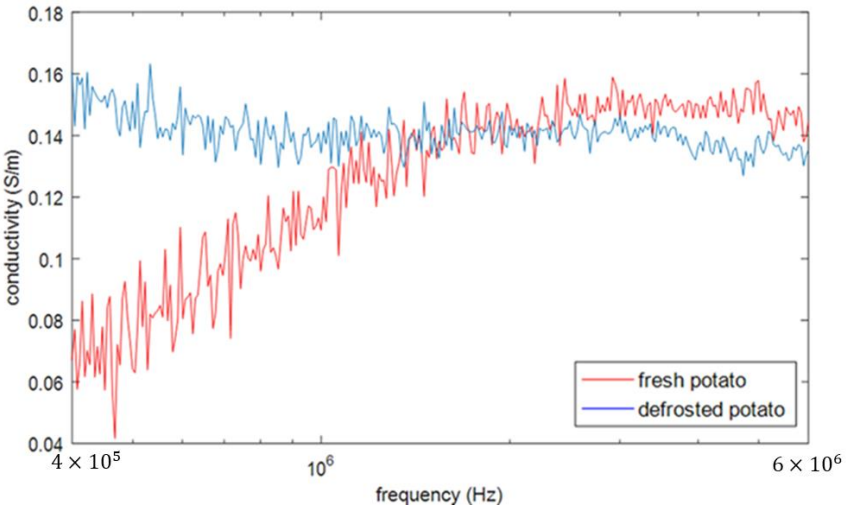

Figure 6-4: Conductivity spectroscopy of potato

6.3.2 Measurement result of frozen-thawed samples

The tested samples were frozen for 24 h between -5 ˚C - -6 ˚C and thawed for 12 h at room temperature between 14 ˚C - 15 ˚C. Frozen process ruptures the cell membranes of biological samples and eliminates the Maxwell-Wagner effect. Thus, the curve of conductivity spectra is expected to be flat and no β-dispersion can be observed.

The conductivity spectra of frozen-thawed loin pork and frozen-thawed potato are shown in Figure 6-3 and Figure 6-4 respectively. The curves are flat comparing with the conductivity spectra of fresh potato and fresh loin pork, and no dispersion can be observed from the results of frozen-thawed samples. β-dispersion is eliminated in the frosted samples. According to published works such as Chen and Wei [13] [15] [82], the frozen-thawed chicken breast

samples exhibit a flat resistivity over the frequency range of β-dispersion. The bio-impedance spectroscopy of other food products such as eggplant [79], grass carp, tilapia [80] and sea bass [74] has been carried out by previous published works. All the conductivity spectra of the fresh food products show a complete β-dispersion while the frozen-thawed food products exhibit flat conductivity spectra over the frequency range of β-dispersion [86] [87] [88] [89]. So our own measurement results agree with the expectations on the bio-impedance spectroscopy of frozen-thawed samples of the previous published works.

6.3.3 Finite element method result

As the volume fraction and membrane thickness is hard to measure for the measurement samples, the electrical parameters of the cell model are selected according to Asami [4]. Figure 6-5 and Figure 6-6 show the eddy current distribution of custom and frozen-thawed cellular model at low frequency and high frequency respectively. The custom cell membrane is not conductive at low frequency and the custom cell model becomes electrically invisible at high frequency since the membrane behaves conductive at higher frequency. However, the frozen-thawed cellular model allows current to flow through the cell at low frequency. The rupture membrane of frozen-thawed

cellular model becomes electrical invisible at high frequency as shown in Figure 6-6.

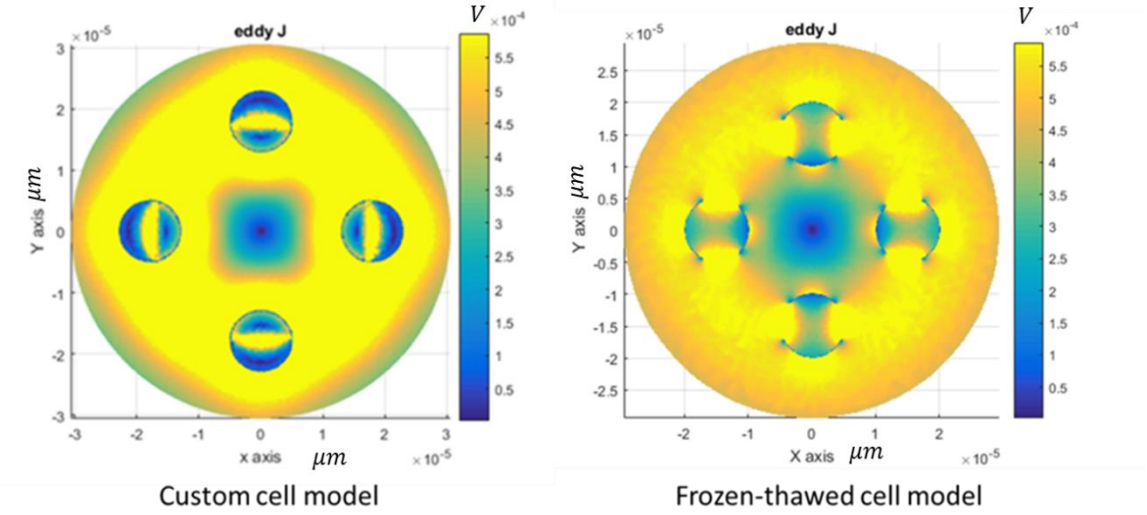

Figure 6-5: Eddy current distribution at low frequency 1 kHz.

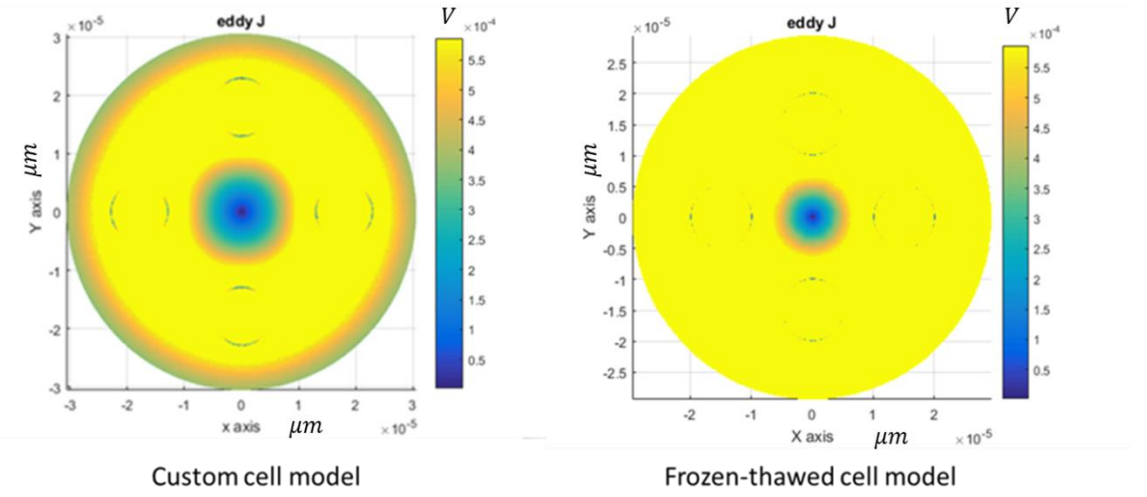

Figure 6-6: eddy current distribution at high frequency 10 MHz.

The equivalent conductivities of the cellular models are calculated according to equation (6-8). The conductivity spectra of fresh model show a β-dispersion at radio frequency while the curve of frozen-thawed model is flat over the frequency range of β-dispersion (Figure 6-7). Therefore, the simulation results

agree with the measurement results that the frozen-thaw progress eliminates the characterised β-dispersion of the bio-impedance spectroscopy. A microscopic experiment has been carried out to validate that the membranes of the frozen-thawed food samples are damaged.

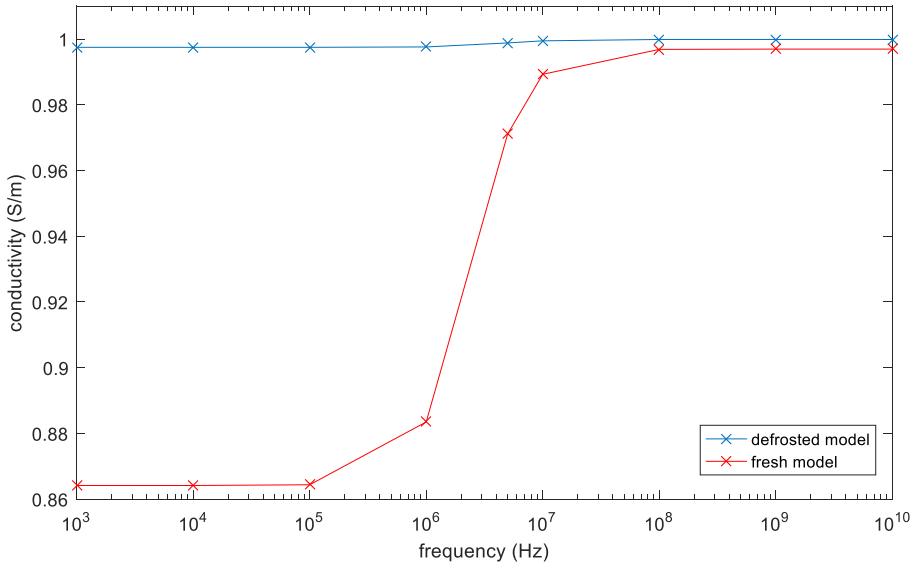

Figure 6-7: 3-D FEM simulation result for fresh model and frozen-thawed model

6.4 Validation methods

6.4.1 Analytical solution

The analytical solution to equivalent complex relative permittivity of the custom single cell model has been introduced in chapter 3.1.

The electrical parameters of the dead cell model are obtained according to Patel [16].

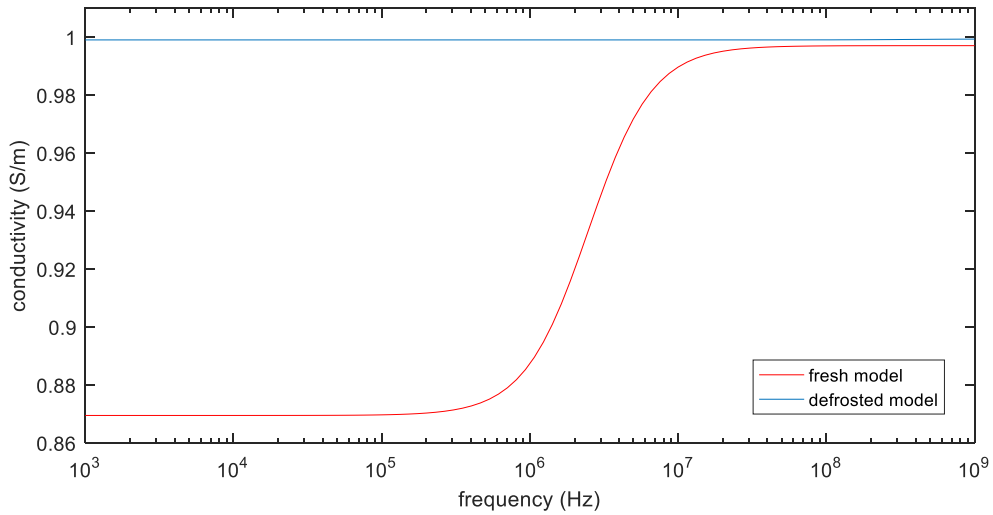

Figure 6-8: Analytical result of fresh model and frozen-thawed model

Since the parameters of fresh model are the same, the conductivity magnitude and dispersion frequency of analytical result are approximated the same with the FEM simulation result. The analytical result in Figure 6-8 agrees with the simulation result in Figure 6-7. Both fresh model results show a β-dispersion over a frequency range from 200 kHz to 10 MHz. However, both the frosted model results show a flat curve over the frequency range of β-dispersion. Thus, the analytical solution result is agreed with FEM simulation result.

6.4.2 Microscopic experiment

A microscopic experiment has been carried out to validate the frozen-thaw effect on the integrity of cell membranes. Propidium Iodide (PI) is selected to be the chemical stainer for food samples. The characteristic of PI is that it can

only stain dead cells with disintegrate membranes while integrate membrane can prevent living cells from the PI stainer. Therefore, PI is an effective stainer to identify the integrity of cell membranes. The PI stainer is prepared by mixing Propidium Iodide with distilled water (weight ratio 1:1). The food sample slides are prepared immediately after impedance measurement. The microscope is Zeiss-Axio scope A1 which is a fluorescent scope and it is capable to take snapshot during the microscopic observations.

The microscopic view of fresh and frozen-thawed potato is shown in Figure 5-3. For the fresh potato, the dark lines represent the cell walls and the bright spot is the vacuole of fresh potato cell. The shape of the fresh potato cell is distinct and the cell has not been stained by the PI. However, the frozen-thawed potato cell has no distinct cell walls and membranes and the cell has been stained by PI. The fluorescent grain in frozen-thawed potato cell is the stained starch grain stained by PI. This result validates that the membrane of the frozen-thawed potato cell has been ruptured and the membrane of fresh potato is integrate.

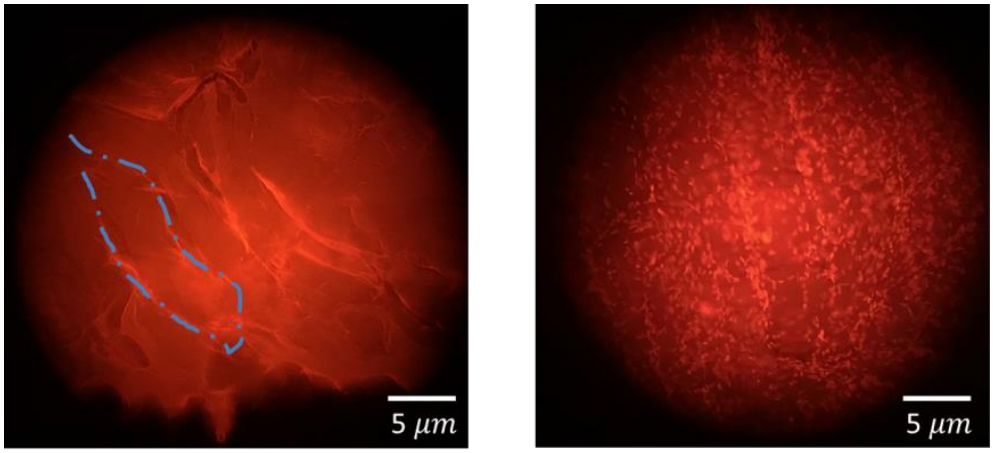

Figure 6-9: microscopic view of fresh and frozen-thawed loin pork cells.

Figure 6-9 shows the microscopic view of fresh and frozen-thawed loin pork cells. The cell shape of the fresh loin pork is marked by imaginary grey line in Figure 6-9. The fresh loin pork cell has not been stained by PI while the frozen-thawed loin pork cell has been stained. The fluorescent spots in frozen-thawed loin pork are the stained DNAs of the cell. The microscopic experiment results on potato and loin pork samples agree with the frozen-thawed cell model that the membrane of the cell has been ruptured after frozen-thaw injury.

6.5 Summary

A non-contact induction measurement method for biological samples is introduced which can be used to obtain the bio-impedance spectra of bio-samples with frequency ranging from 400 kHz to 6 MHz. The prominent

feature of the system is the high accuracy of 0.01 S/m, the rapid measurement speed and the entire non-destructive process, which is well suited for medical or industrial applications. The measurements are repeatable with high stability. An induction FEM model to simulate the non-contact measurement is presented and validated by analytical solutions and microscopic experiments. The induction simulation model is a more accurate approach to non-contact measurement comparing with the existing electric field simulation model. The result of FEM simulation agrees with the measurement result.

7 An acceleration method for thin shell finite element models

7.1 Introduction

In this section, a method for accelerating eddy current calculation on a cell model using the finite element method (FEM) is presented. Due to the tiny thickness of cell membrane, an accurate cell model requires a large number of mesh elements and hence intensive computation resources. An acceleration method is therefore proposed to reduce the number of mesh elements and thus reduce the computational time. It is based on the principle of replacing the thin cell membrane with an equivalent thicker structure. The method can reduce the number of mesh elements up to 20% and the computational time to a fraction with an error of less than 1%. The method is verified using 2-D and 3-D finite element methods and can potentially be extended to other thin shell structures. The simulation results are verified by measurement and analytical results.

Analytical solutions are well developed to calculate the β-dispersion [4] [41]. However, the analytical solution is only designed to analyse the models with regular shape (i.e. spherical cell model) [4], [67]. In reality, most cell shapes are anomalous. FEM is a feasible way to simulate the dielectric dispersions for models with irregular shapes [90].

The difficulty of FEM is that the number of meshing elements is significantly large due to the tiny thickness of cell membrane. It takes a long time to compute with numerous meshing elements. The FEM acceleration method is proposed to reduce the number of meshing elements and computing time by replacing the full-mesh membrane model with an equivalent reduced-mesh model. It is used to simulate spherical and oval cell model in 2-D and 3-D versions.

7.2 Custom cell models based on 2-D and 3-D FEM

7.2.1 CELL MODEL

The custom cell model is the single shell spherical mode, which has been introduced in chapter 3. The spherical cell model is shown in Figure 3-1 [4]. The 2-D simulation model is a single cell model as shown in Figure 3-1.The spherical cell is put in a suspension with applied alternating electric field. The cell membrane blocks the current flow between intra-cellular and extra-cellular fluid due to the low conductivity. This results in Maxwell-Wagner effect, an interfacial polarisation of the cell membrane blocking the ion-flow of intra and extra cellular dielectrics. The Maxwell-Wagner effect leads to a dispersion on conductivity and permittivity at frequency ranging from 100 kHz to 10 MHz. This dispersion is introduced as β-dispersion.

7.2.2 3-D FEM SIMULATION

An induction model is built for the 3-D FEM simulation. As shown in Figure 7-1, the cylinder stands for the cell suspension and the spherical model stands for the cell. Imaginary transmitter and receiver coils are put on the top of the suspension to provide alternating magnetic field as an exciting signal and detect induced secondary magnetic field.

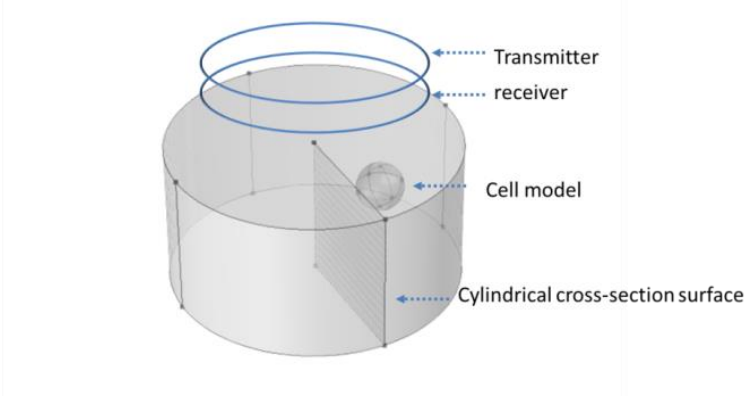

Figure 7-1: 3-D single cell model

In Figure 7-1, an alternating current is applied to the transmitter coil and an alternating magnetic field is induced [38]. The basic theory of finite element method was introduced in chapter 3.3.

7.3 Acceleration model

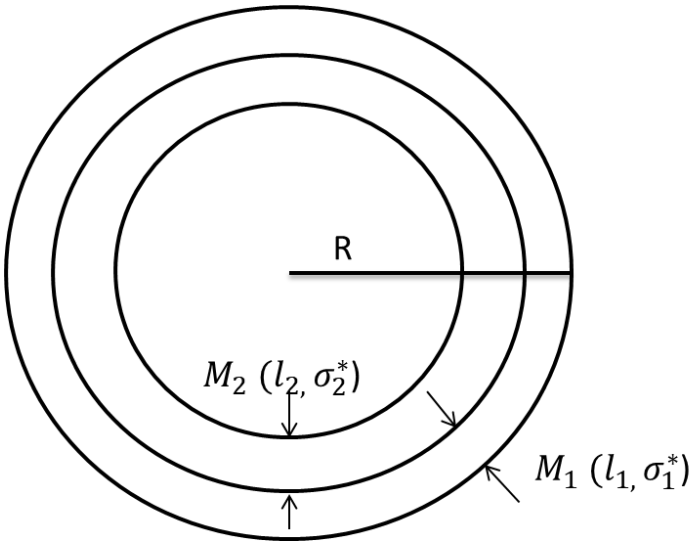

Figure 7-2: Acceleration model

The complicated calculation progress and the long computational time are caused by the large number of meshing elements around the thin membrane. The number of meshing elements can be reduced by enlarge the membrane thickness. However, changing the membrane thickness affects the conductivity spectrum of the cell suspensions. The aim of the proposed acceleration method is to keep the accuracy of simulation result while enlarge the membrane thickness (reducing number of elements). This acceleration method replaces the full-mesh model with an equivalent thicker membrane (reduced-mesh model) with an equivalent complex conductivity, as shown in Figure 7-2. In Figure 7-2 M_1 is the full-mesh model membrane with normal thickness l_1. M_2 is the enlarged part of the reduced-mesh model membrane with thickness l_2. R is the radius of the cell model. The electrical parameter of the membrane M_2 is exactly the same as that of the intra-cellular fluid. M_1 and M_2 combine as a thicker equivalent membrane (i.e. reduced-mesh model

membrane). The thickness of the reduced-mesh model membrane is $l_1 + l_2$. The equivalent complex conductivity of the reduced-mesh model membrane is calculated by equation (6-8). The number of meshing elements is reduced due to a thicker equivalent membrane. However, with the equivalent complex conductivity, the behaviour of Maxwell-Wagner effect which leads to β-dispersion remains the same.

The parameters of the membrane M_1 and M_2 can be expressed as:

$$\sigma_1^* = \sigma_1 + j\omega\varepsilon_1\varepsilon_0 \quad (7\text{-}1)$$

$$\sigma_2^* = \sigma_2 + j\omega\varepsilon_2\varepsilon_0 \quad (7\text{-}2)$$

where σ_1^* and σ_2^* are the complex conductivity of M_1 and M_2. σ_1 and σ_2 are the conductivity of M_1 and M_2 respectively. ε_1 and ε_2 are the relative permittivity of M_1 and M_2 respectively. ε_0 is the permittivity of vacuum. $\omega = 2\pi f$ where f is the frequency. j is the imaginary unit.

Considering the two membranes M_1 and M_2 are connected as two electrolytes in series. The total impedance Z is:

$$\mathrm{Z} = Z_1 + Z_2 = \frac{l_1}{\sigma_1^* S_1} + \frac{l_2}{\sigma_2^* S_2} \quad (7\text{-}3)$$

where Z_1 and Z_2 are the impedance of the M_1 and M_2 respectively. σ_1^* and σ_2^* are the complex conductivity of M_1 and M_2 respectively. l_1 and l_2 are the thickness of the M_1 and the M_2 in Figure 7-2 respectively. S_1 and S_2 are the area of M_1 and the M_2 respectively. As l_1 and l_2 are negligible comparing with radius R, the area $S_1 = S_2$.

Then the equivalent complex conductivity can be derived as:

$$Z = \frac{l_1}{\sigma_1^* S_1} + \frac{l_2}{\sigma_2^* S_2} = \frac{l_1\sigma_2^* + l_2\sigma_1^*}{\sigma_1^*\sigma_2^*}\ \frac{1}{S_1} = \frac{(l_1 + l_2)}{\sigma_e^*}\ \frac{1}{S_1} \quad (7\text{-}4)$$

$$\sigma_e^* = \frac{(l_1 + l_2)\sigma_1^*\sigma_2^*}{l_1\sigma_2^* + l_2\sigma_1^*} \quad (7\text{-}5)$$

σ_e^* is the complex conductivity of the equivalent membrane (reduced-mesh model membrane).

7.4 Results and discussion

7.4.1 2-D FEM cell models

7.4.1.1 Full-mesh model

The full-mesh model membrane thickness is 5 nm. There are two simulations with the equivalent membrane (reduced-mesh model) thickness of 10nm and 20nm respectively. The ratio between the full-mesh model membrane (M_1 in Figure 7-2) thickness and the enlarged part of reduce-model membrane (membrane M_2 in Figure 7-2) thickness is 1:1 and 1:3 respectively. The simulation results are the progress of β-dispersion which reflects dispersions on relative permittivity and conductivity, as shown in Figure 7-3 and Figure 7-4.

As shown Table 7-1, the number of elements of full-mesh model can be reduced to 24% when the equivalent membrane (reduced-mesh model) is four times as the thickness of the full-mesh model membrane (M_1 to M_2 thickness

ratio is 1:3). The computational time is reduced from 73 minutes to 13 minutes with only 0.2% relative error on the simulation result. The computing time of the reduced-mesh model is 18% of full-mesh model. The spectroscopy of conductivity and relative permittivity is shown in Figure 7-3 and Figure 7-4, the results of reduce-model and full-mesh model show the same magnitude over the same frequency range with a relative error less than 0.2%. The β-dispersion of the reduce-model and full-mesh model both starts at 100 kHz and both ends at 10 MHz. This shows that the reduced-mesh model can significantly accelerate the computing progress with only a tiny error on the result in 2-D-FEM spherical model simulation.

Table 7-1: Result of 2-D acceleration model

Ratio(full-mesh thickness /inserted thickness)	**Number of elements**	**Relaive Error (%)**	**Computing time(minutes)**
original	73092	N/A	73
1:1	35272 (reduced to 48.3%)	0.07	28
1:3	17342 (reduced to 23.7%)	0.2	13

Table 7-2: Result of 2-D deformation acceleration model

Ratio (full-mesh thickness /inserted thickness)	**Number of elements**	**Relative Error (%)**	**Computing time**
Original(a=12,b=2)	133184	N/A	2hrs 24minutes
1:1	64600 (reduced to 48.5%)	0.04	62 minutes
1:3	32097 (reduced to 24.1%)	0.11	25 minutes

Table 7-3: Result of 3-D acceleration model

Ratio (full-mesh thickness /inserted thickness)	**Number of elements**	**Relative Error (%)**	**Computing time**
original	205604	N/A	4hrs 37mins
1:1	141870(reduced to 69%)	0.4	3hrs 5mins
1:3	57934(reduced to 28%)	2	71mins

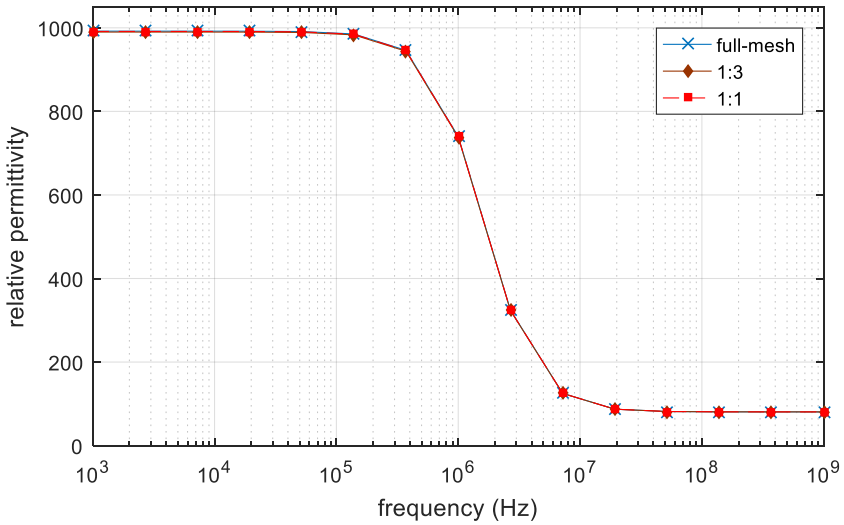

Figure 7-3: Relative permittivity of 2-D single spherical cell model

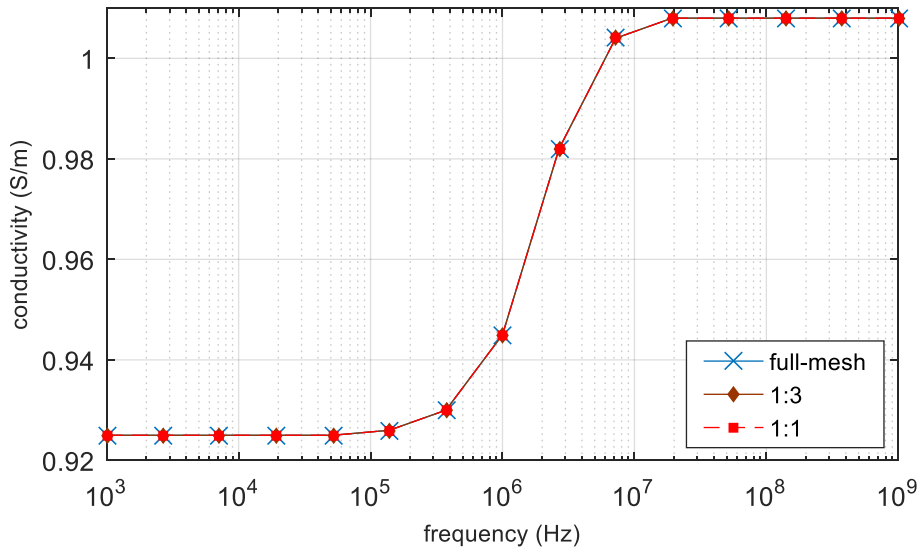

Figure 7-4: Conductivity of 2-D single spherical cell model

7.4.1.2 DEFORMATION MODEL

This simulation is to verify that the acceleration method works not only on spherical cell model but also a deformation model (oval model).

The deformation model is an oval model in order to simulation the cell deformation. The electrical parameters of the oval model are the same with that of the custom spherical model. The model is shown in Figure 7-5, where a and b are the length of the semi-major and semi-minor axis respectively. The length of semi-major axis is set to be $a = 12\ \mu m$ and the length of semi-minor axis is set to be $b = 2\ \mu m$. k_a and k_c are the conductivity of the extra-cellular and intra-cellular fluid respectively. ε_c and ε_a are the relative permittivity of the intra-cellular and extra-cellular fluid respectively. ε_m is the relative permittivity of cell membrane. $d_m$is the membrane thickness. The full-mesh model membrane thickness is still $5nm$ and the electrical properties are

calculated using equation (6-8). The simulation result of β-dispersion is shown in Figure 7-6, Figure 7-7 and the parameters of the computing time and error are shown in Table 7-2.

The number of elements of full-mesh model can be reduced to 24.1% as shown in Table 7-2 and the computational time is reduced from 2hrs 24mins to 25mins. The simulation error between reduced-mesh model and full-mesh model is only 0.11%. As shown in Figure 7-6 and Figure 7-7, the results of full-mesh model and reduced-mesh model exhibits β-dispersion with tiny error in the same frequency range. The results show that the acceleration method is feasible to simulate not only the spherical model but also the deformation model (oval model). The computational time is significantly reduced with an acceptable error.

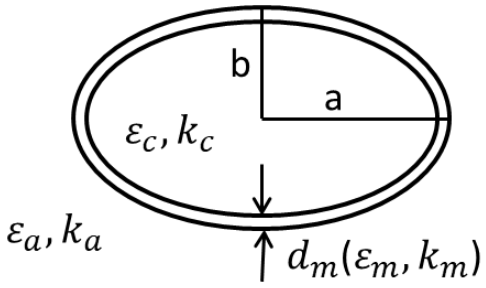

Figure 7-5: Deformation model

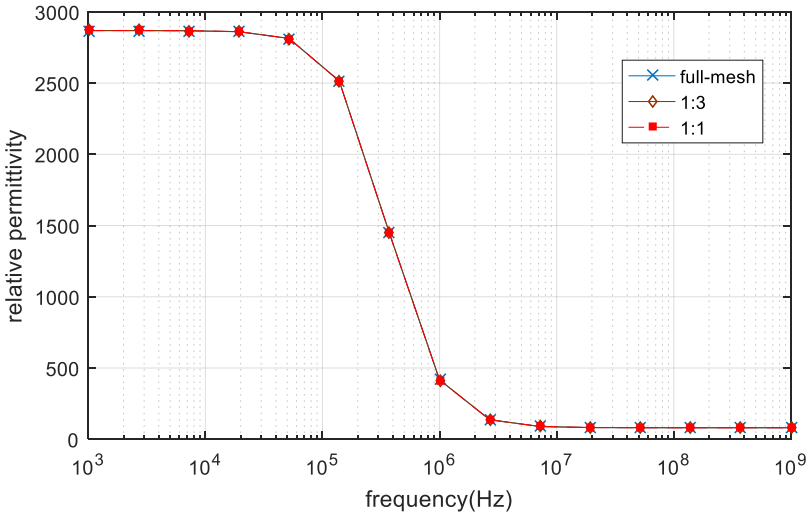

Figure 7-6: Relative permittivity of 2-D single deformation cell model

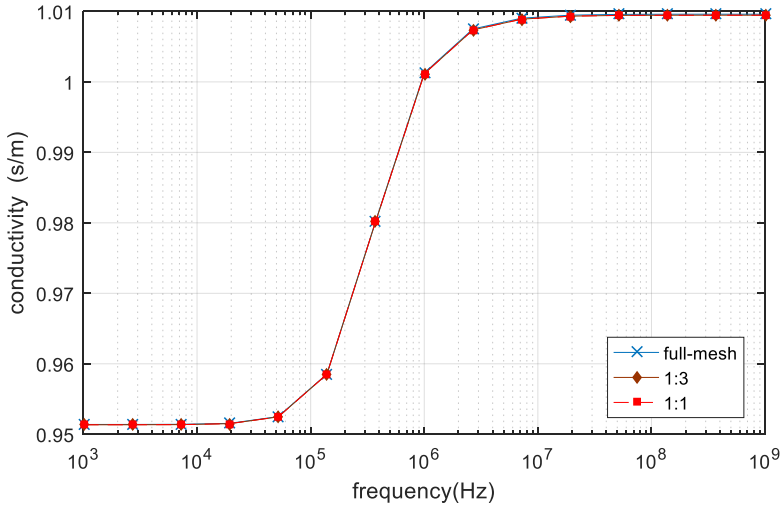

Figure 7-7: Conductivity of 2-D single deformation cell model

7.4.2 3-D FEM cell models

The simulation model used for 3-D FEM simulation is the 3-D single sphere cell model shown in Figure 7-1. The radius of the cell model is set to be 5 μm and the membrane thickness is 5nm. The top view of eddy current distributions at the low frequency of 1 kHz and the high frequency of 10 MHz are shown in Figure 7-8. The single cell model blocks eddy currents at the low frequency and becomes conductive at the high frequency which meets the expectations

of Maxwell-Wagner effect and other published work [32] [91].

The full-mesh model membrane thickness is 5 nm. There are two reduce-models with equivalent thicker membrane (reduced-mesh model) thickness of 10nm and 20nm respectively. The ratio between the full-mesh model membrane thickness and the reduced-mesh membrane thickness is 1:1 and 1:3 respectively. The relative permittivity and conductivity results are shown in Figure 7-9 and Figure 7-10. β-dispersion can also be observed in the figures. The β-dispersion of the full-mesh model and reduced-mesh model has a relative error of 2% on the magnitude. The frequency range of the β-dispersion of full-mesh model and reduced-mesh model are the same, ranging from 100 kHz to 10 MHz. The results, including the number of elements, the computational time and the error of full-mesh model and reduced-mesh model are shown in Table 7-3. The number of elements of full-mesh model can be reduced to 28% as shown in Table 7-3 and the computational time is reduced from 4hrs 37mins to 71mins. The simulation error between the reduced-mesh model and the full-mesh model is 2%. The error is larger than 2-D simulation result but it is acceptable for β-dispersion simulations. The results show that the acceleration method is feasible to simulate 3-D spherical model. The computational time is significantly reduced with an acceptable error.

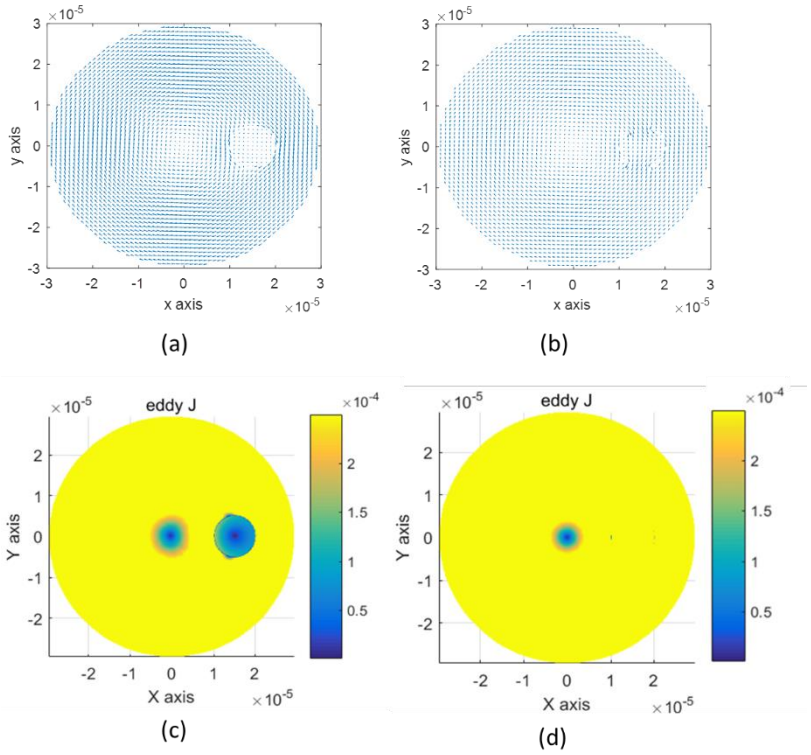

Figure 7-8: (a) Eddy current flow at the low frequency of 1 kHz (b) Eddy current flow at the high frequency of 10 MHz (c) Eddy current density at low frequency 1 kHz (d) Eddy current density at high frequency 10 MHz

The results show that the acceleration method is feasible to simulate three dimensional spherical model. The computing time is significantly reduced with acceptable error.

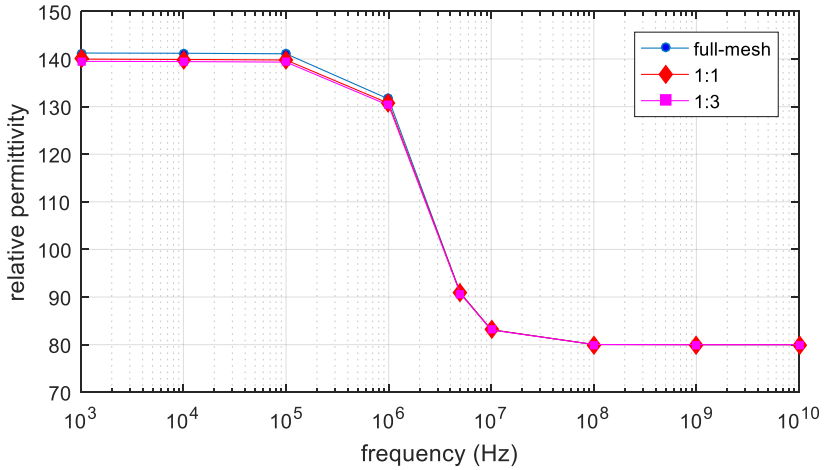

Figure 7-9: Relative permittivity of 3-D single spherical cell model

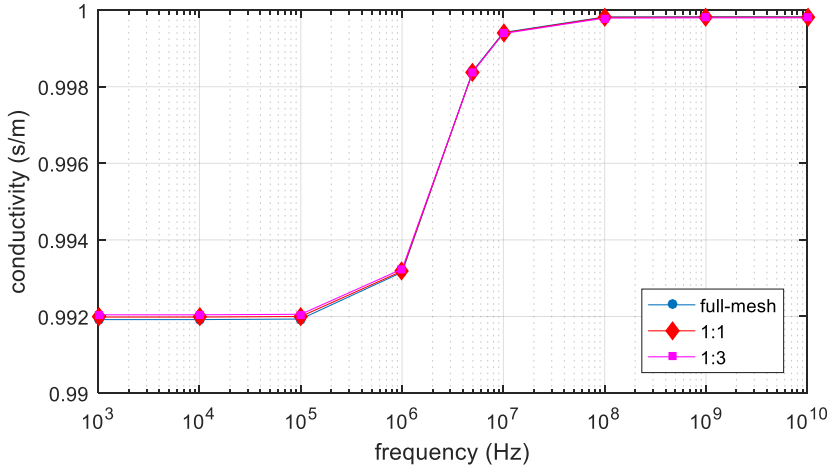

Figure 7-10: Conductivity of 3-D single spherical cell model

7.4.3 Validation methods

7.4.3.1 Contact electrode method

The contact electrode measurement method has been introduced in section 2.5.1. The electrode is contacted directly to the samples to measure the impedance over the samples using an impedance analyzer. The measurement sample is fresh potato (obtained from a local market). This measurement is to validate the FEM simulation results. All the FEM simulation parameters are set

to be the realistic values obtained from the measurement.

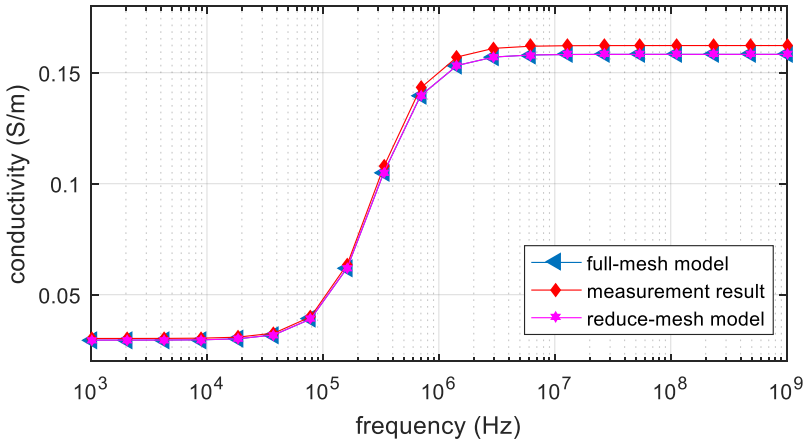

Figure 7-11: Impedance spectroscopy of the FEM and measurement results.

In Figure 7-11, the FEM and measurement results show similar β-dispersion with the same dispersion frequency range. There is some error on the magnitude of the conductivity between the measurement results and simulation results. However, the error is acceptable for the simulation approach. The conductivity of measurement and simulation results is low at the low frequency and the dispersion starts at around 50 kHz. The dispersion ends at around 2 MHz and the conductivity of measurement and simulation result is increased to 0.15 S/m. The spectroscopy curve is flat over the higher frequency range. The measurement results validated the full-mesh and reduced-mesh FEM simulation results and agreed with other published work [28] [91] [92].

7.4.3.2 Analytical solution

The analytical solution method has been introduced in section 3.1.

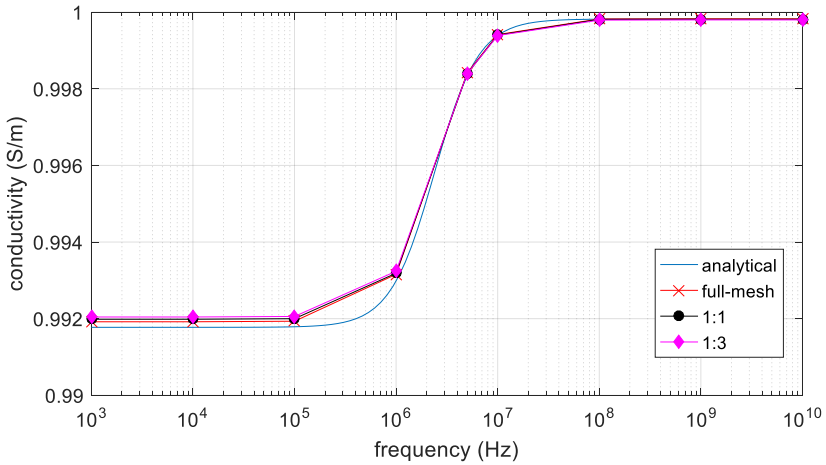

Figure 7-12: Calculated conductivity of the analytical solution and the FEM simulation

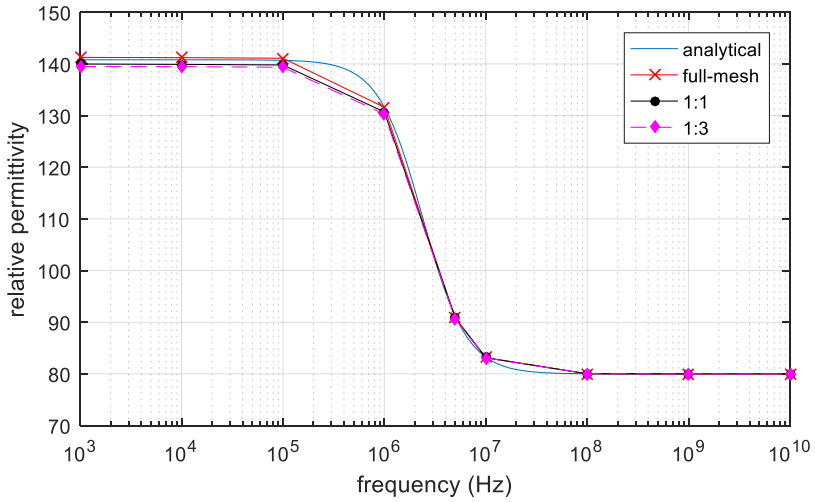

Figure 7-13: Calculated relative permittivity of the analytical solution and the FEM simulation

In Figure 7-12 and Figure 7-13 both the analytical and FEM results show the same magnitude and frequency range of beta dispersion with a relative error less than 0.1%. The volume fraction of the cell is set to be the same as P=3.5%. The magnitude and frequency range of β-dispersion on the full-mesh model and reduced-mesh model agree with the analytical results. The result

validates that the 3-D FEM simulation on cell suspension is accurate and the improved acceleration method is also validated. So the proposed acceleration method can be applied on further FEM simulations on irregular shape cell models and thin shell models.

7.5 Summary

This chapter proposed a method to accelerate FEM calculation with bio-cell models. The idea is to replace the thin membrane (full-mesh model) with an equivalent thicker membrane (reduced-mesh model). Then the number of meshing elements of full-mesh model is reduced and thus the computational time is reduced.

According to the simulation results, the reduced-mesh model can be used in both 2-D and 3-D FEM simulations. The amount of computational time is significantly reduced with a relative error no more than 0.5% in 2-D simulation. The relative error on 3-D simulation result is no more than 2%. All simulation results are validated by the measurements and analytical results.

The proposed acceleration method is validated to be fast and accurate on cell models. It also has potential for all other thin shell FEM models.

8 Conclusions and future work

8.1 Conclusions

This thesis focuses on analysing the bio-impedance spectroscopy based on the two measurement systems and finite element simulation method. The major work of this thesis was to build up two measurement systems, i.e. contact electrode system and non-contact induction system, to measure the bio-impedance spectroscopy of frozen-thawed food samples. In addition, a modelling method for frozen-thawed samples and an acceleration method for thin shell cell model are proposed for simulating the bio-impedance spectroscopy. The author further proposed simulation analysis about the influence of cellular structure, including cell shape and membrane thickness, on bio-impedance spectroscopy.

8.1.1 Cellular structure influence on bio-impedance spectroscopy

The influence of cellular structure, including cell shape and membrane thickness, on bio-impedance spectroscopy was further analysed based on finite element simulation method, as described in chapter 4. There are several conclusions drawn from the simulation results:

1) Deformed oval cell model exhibits β-dispersion with a larger magnitude than that of the sphere cell model.

2) The oval cell model with less orientation angle towards the applied field / current direction exhibits β-dispersion with a smaller magnitude than that of the oval models with a larger orientation angle towards the applied field/ current direction.
3) The magnitude of relative permittivity of β-dispersion increases with the increasing of cell perimeter / surface area to membrane thickness increases.

8.1.2 Frozen-thawed effect influence on bio-impedance spectroscopy

The mechanism of how frozen-thawed effect influences the bio-impedance spectroscopy of biological food samples was further analysed for building a simulation model and designing microscopic experiments, as described in chapter 5 and chapter 6. The findings are listed below:

1) The measurement results show that the fresh food samples with intact cell membrane exhibit a complete β-dispersion while the frozen-thawed food samples only exhibit a flat conductivity curve over the frequency range of the β-dispersion.
2) The β-dispersion caused by the Maxwell-Wagner effect occurs at the cell membrane. To verify the frozen-thawed injury to cell membrane, a microscopic experiment was designed to detect the integrity of the cell membrane of fresh food samples and frozen-thawed food samples. The

microscopic experiment shows that the cell membrane of fresh food samples is integrate while the cell membrane of frozen-thawed food samples is ruptured.

3) A simulation modelling of cell with disintegrate membrane was carried out to verify the measurement and microscopic experiment results.

Based on the measurement and simulation results, it can be concluded that the frozen-thawed effect influences the bio-impedance spectroscopy by damage the cell membrane.

8.1.3 Acceleration method for thin shell FEM models

An acceleration modelling method for thin shell finite element method was proposed, as described in chapter 7. The acceleration method is to reduce the meshing elements by building an equivalent model with thicker membrane. Based on this acceleration modelling method, the computation time of reduced-mesh model can be significantly reduced to 24% of the computation time of a full-mesh model. This method has been validated by the analytical solution and measurement results. Some conclusions are presented below:

1) When applied to a 2-D spherical model, the computational time of the reduced-mesh model decreased to 18% of that of the full-mesh model, with a relative error of 0.2%.
2) When applied to a 2-D oval model, the computational time of the reduced-mesh model is reduced to 17.3% of that of the full-mesh model,

with a relative error of 0.11%.

3) When applied to a 3-D spherical model, the computational time of the reduced-mesh model is reduced to 25.6% of that of the full-mesh model, with a relative error of 2%.

8.2 Summary of contributions

1) A FEM solver was built to analyse the influence of cellular structure (cell shape, membrane thickness and cell orientation) on the BIS. This work is of great significance in BIS area, since there was little research on how the cellular structure influences the result of BIS.
2) Proposed an acceleration method for FEM thin cell membrane modelling. This method can reduce the computational time up to 25% with only relative error within 0.4%-2%. It can be applied on not only BIS simulation but also other thin shell FEM models.
3) Two measurement systems (the contact-electrode method and non-contact induction method) were built for analysing the BIS of the food samples. The BIS of food samples can be measured by the two measurement systems accurately and effectively.
4) The mechanism of frozen-thaw effect was analysed by self-designed FEM modelling and measurement systems. The simulation and measurement results have been validated by the microscopic experiment. There was little

literature on discussing the mechanism of frozen-thaw effect. Hence, this work is of significant contribution to BIS area since.

8.3 Future work

To develop the measurement system for bio-impedance spectroscopy, further research is required based on the conclusions drawn from this study.

1) Measuring the bio-impedance spectroscopy of moving food samples (e.g. in a conveyer belt) in real time. One of the applications of the technique developed in this thesis can be real time monitoring of food quality and therefore real time measurement is necessary. Currently, the measurement setup requires sample to be fixed, volume to be defined, and the average of measurements in a relatively long duration. In addition, the size of the sensor is relatively large (with a diameter of ~20cm) currently and this should be reduced for practical applications. With these further developments, the technique can realise its huge potential and meet the requirements for real world food industrial applications.
2) For the non-contact induction measurement, the measurement frequency range currently is 400 kHz – 6 MHz. A larger frequency range of measurement is worth investigating by designing new sensors. This will further expand the materials the technique can inspect and provide clearer trend for β-dispersion.
3) Design measurements on how cell membrane thickness and cell shape

influence the bio-impedance spectroscopy. While the thesis has produced simulation evidence of this phenomenon given the time constraint of this PhD project, it would be a significant progress if these can be validated in experiments and this will pave the way for distinguishing different kinds of cells/ tissues in real applications.

4) For frozen-thaw effect, more time-control groups can be set to observe the change of bio-impedance spectroscopy with different frozen times and levels. This will further provide evidence and best practise for food preservation and possibly have implications for life/medical sciences.

REFERENCES

1. Schwan H P. Electrical properties of tissues and cell suspensions: mechanisms and models//Engineering in Medicine and Biology Society, 1994. Engineering Advances: New Opportunities for Biomedical Engineers. Proceedings of the 16th Annual International Conference of the IEEE. IEEE, 1994: A70-A71 vol. 1.

2. Pethig R, Kell D B. The passive electrical properties of biological systems: their significance in physiology, biophysics and biotechnology. Physics in medicine and biology, 1987, 32(8): 933.

3. Damez J L, Clerjon S, Abouelkaram S, et al. Dielectric behavior of beef meat in the 1–1500kHz range: Simulation with the Fricke/Cole–Cole model. Meat Science, 2007, 77(4): 512-519.

4. Asami K. Dielectric dispersion in biological cells of complex geometry simulated by the three-dimensional finite difference method. Journal of Physics D: Applied Physics, 2006, 39(3): 492.

5. Hanai T, Asami K, Koizumi N. Dielectric Theory of Concentrated Suspensions of Shell. Bull. Inst. Chem. Res., Kyoto Univ, 1979, 57(4).

6. Pauly H, Schwan H P. Über die Impedanz einer Suspension von kugelförmigen Teilchen mit einer Schale. Zeitschrift für Naturforschung B, 1959, 14(2): 125-131.

7. Zhu, F., Kuhlmann, M. K., Kaysen, G. A., Sarkar, S., Kaitwatcharachai, C., Khilnani, R., ... & Levin, N. W.. Segment-specific resistivity improves body fluid volume estimates from bioimpedance spectroscopy in hemodialysis patients. *Journal of Applied Physiology*,2006, *100*(2), 717-724.

8. Jaffrin, M. Y., Fenech, M., Moreno, M. V., & Kieffer, R. Total body water measurement by a modification of the bioimpedance spectroscopy method. *Medical and Biological Engineering and Computing*,2006, *44*(10), 873-882.

9. Fenech, M., & Jaffrin, M. Y. Extracellular and intracellular volume variations during postural change measured by segmental and wrist-ankle bioimpedance spectroscopy. *IEEE transactions on biomedical engineering*, 2004, *51*(1), 166-175.

10. Morimoto T, Kimura S, Konishi Y, et al.,.A study of the electrical bio-impedance of tumors. Journal of Investigative Surgery, 1993, 6(1):

25-32.

11. Romsauerova A, McEwan A, Horesh L, et al.,.Multi-frequency electrical impedance tomography (EIT) of the adult human head: initial findings in brain tumours, arteriovenous malformations and chronic stroke, development of an analysis method and calibration. Physiological measurement, 2006, 27(5): S147.

12. Dower W J, Miller J F, Ragsdale C W. High efficiency transformation of E. coli by high voltage electroporation. Nucleic acids research, 1988, 16(13): 6127-6145.

13. Chen T H, Zhu Y P, Wang P, et al. The use of the impedance measurements to distinguish between fresh and frozen–thawed chicken breast muscle. Meat science, 2016, 116: 151-157.

14. Mukhopadhyay S C, Gooneratne C P.A planar-type biosensor for noninvasive meat inspection. IEEE Sensors Journal, 2007, 7(9): 1340-1346.

15. Wei, R., Wang, P., Han, M., Chen, T., Xu, X., & Zhou, G. Effect of freezing on electrical properties and quality of thawed chicken breast meat. *Asian-Australasian journal of animal sciences*, 2017, *30*(4), 569.

16. Patel S, Showers D, Vedantam P, et al. Microfluidic separation of live and dead yeast cells using reservoir-based dielectrophoresis. Biomicrofluidics, 2012, 6(3): 034102.

17. Asami K, Hanai T, Koizumi N. Dielectric properties of yeast cells. The Journal of membrane biology, 1976, 28(1): 169-180.

18. Hölzel R, Lamprecht I. Dielectric properties of yeast cells as determined by electrorotation. Biochimica et Biophysica Acta (BBA)-Biomembranes, 1992, 1104(1): 195-200.

19. Lassota Z G.Brewing system with electrical controller and method. U.S. Patent,1999, 953,981[P].

20. Sone Y, Ekdunge P, Simonsson D. Proton conductivity of Nafion 117 as measured by a four‐electrode AC impedance method. Journal of the

Electrochemical Society, 1996, 143(4): 1254-1259.

21. Alberts B, Johnson A, Lewis J, et al. Cell movements and the shaping of the vertebrate body. Molecular Biology of the Cell,2002, 4th edition. Garland Science.

22. Sekine K. Finite-element calculations for dielectric relaxation of one-sphere systems in a parallel-electrode measuring cell. Colloid and Polymer Science, 1999, 277(4): 388-393.

23. Awayda M S, Van Driessche W, Helman S I.Frequency-dependent capacitance of the apical membrane of frog skin: dielectric relaxation processes. Biophysical journal, 1999, 76(1): 219-232.

24. Ishihara K, Ueda T, Nakabayashi N. Preparation of phospholipid polylners and their properties as polymer hydrogel membranes. Polymer Journal, 1990, 22(5): 355.

25. Gheorghiu E. Relating membrane potential to impedance spectroscopy. Journal of Electrical Bioimpedance, 2011, 2(1): 93-97.

26. Wang J R, Sun B Y, Wang H X, et al. Experimental Study of Dielectric Properties of Human Lung Tissue in Vitro. Journal of Medical and Biological Engineering, 2014, 34(6): 598-604.

27. Qing M A. Investigation on Dielectric Properties of Biological Cells with Impedance Technique in Frequency Domain. Chinese Journal of Medical Physics, 2004, 4: 000.

28. Nandi N, Bagchi B. Dielectric relaxation of biological water. The Journal of Physical Chemistry B, 1997, 101(50): 10954-10961.

29. Ciancio V. On the generalized Debye equation for media with dielectric relaxation phenomena described by vectorial internal thermodynamic variables. Journal of Non-Equilibrium Thermodynamics, 1989, 14(3): 239-250.

30. Grimnes S, Martinsen Ø G. Alpha-dispersion in human tissue. Journal of Physics: Conference Series. IOP Publishing, 2010, 224(1): 012073.

31. Prodan E, Prodan C, Miller J H. The dielectric response of spherical live cells in suspension: an analytic solution. Biophysical journal, 2008, 95(9):

4174-4182.

32. Stubbe M, Gimsa J.Maxwell’s Mixing Equation Revisited: Characteristic Impedance Equations for Ellipsoidal Cells. Biophysical journal, 2015, 109(2): 194-208.

33. rjan G. Martinsen, interface phenomena and dielectric properties of biological tissue. Encyclopedia of Surface and Colloid Science,2002

34. Ding Chong. progress of technology and application of dielectric spectroscopy of cell suspension. Beijing Biomedical engineering, 2014, Vol 33, No.1:01-0094-07

35. Jaffrin M Y, Morel H. Body fluid volumes measurements by impedance: A review of bioimpedance spectroscopy (BIS) and bioimpedance analysis (BIA) methods. Medical engineering & physics, 2008, 30(10): 1257-1269.

36. Armstrong L E, Kenefick R W, Castellani J W, et al.Bioimpedance spectroscopy technique: intra-, extracellular, and total body water. Medicine and science in sports and exercise, 1997, 29(12): 1657-1663.

37. Van Loan, Marta D., et al.Use of bioimpedance spectroscopy to determine extracellular fluid, intracellular fluid, total body water, and fat-free mass. *Human body composition*. Springer, 1993, Boston, MA, 67-70.

38. O'Toole M D, Marsh L A, Davidson J L, et al. Non-contact multi-frequency magnetic induction spectroscopy system for industrial-scale bio-impedance measurement. Measurement Science and Technology, 2015, 26(3): 035102

39. Barai A, Watson S, Griffiths H, et al. Magnetic induction spectroscopy: non-contact measurement of the electrical conductivity spectra of biological samples. Measurement Science and Technology, 2012, 23(8): 085501

40. Krishan A. Rapid flow cytofluorometric analysis of mammalian cell cycle by propidium iodide staining. The Journal of cell biology, 1975, 66(1): 188-193.

41. Gowrishankar T R, Weaver J C. An approach to electrical modeling of single and multiple cells. Proceedings of the National Academy of Sciences, 2003, 100(6): 3203-3208.

42. Georgii, Joachim, and Rudiger W. A streaming approach for sparse matrix

products and its application in Galerkin multigrid methods. Electronic Transactions on Numerical Analysis,2010, 37: 263-275.

43. Jin J M. The finite element method in electromagnetics. John Wiley & Sons, 2014, P1-875.

44. Bíró O. Edge element formulations of eddy current problems. Computer methods in applied mechanics and engineering, 1999, 169(3-4): 391-405.

45. Fritschy, J., et al., .Using the GRID to improve the computation speed of electrical impedance tomography (EIT) reconstruction algorithms. Physiological measurement,2005,26.2: S209.

46. Lu Mingyang, Anthony Peyton, and Wuliang Yin, “Acceleration of Frequency Sweeping in Eddy-Current Computation,” IEEE Transactions on Magnetics, 2017, 53.7 : 1-8.

47. Kyle A H, Chan C T O, Minchinton A I. Characterization of three-dimensional tissue cultures using electrical impedance spectroscopy. Biophysical journal,1999, 76(5): 2640-2648.

48. Mahaworasilpa T L, Coster H G L, George E P. Forces on biological cells due to applied alternating (AC) electric fields. I. Dielectrophoresis. Biochimica et Biophysica Acta (BBA)-Biomembranes, 1994, 1193(1): 118-126.

49. Shi J, Ma Q, Wang J. The finite element simulation of dielectric properties of blood//Piezoelectricity, Acoustic Waves, and Device Applications (SPAWDA) and 2009 China Symposium on Frequency Control Technology, Joint Conference of the 2009 Symposium on. IEEE, 2009: 135-135.

50. Gabriel C. Compilation of the Dielectric Properties of Body Tissues at RF and Microwave Frequencies. KING'S COLL LONDON (UNITED KINGDOM) DEPT OF PHYSICS, 1996.

51. Asami K, Yonezawa T. Dielectric behavior of non-spherical cells in culture. Biochimica et Biophysica Acta (BBA)-General Subjects,1995, 1245(3): 317-324.

52. Wabel P, Chamney P, Moissl U, et al. Importance of whole-body bioimpedance spectroscopy for the management of fluid balance. Blood purification, 2009,27(1): 75-80.

53. Earthman, C., Traughber, D., Dobratz, J., & Howell, W. Bioimpedance

spectroscopy for clinical assessment of fluid distribution and body cell mass. *Nutrition in Clinical Practice*, 2007, *22*(4), 389-405.

54. Hur, E., Usta, M., Toz, H., Asci, G., Wabel, P., Kahvecioglu, S., ... & Ok, E. Effect of fluid management guided by bioimpedance spectroscopy on cardiovascular parameters in hemodialysis patients: a randomized controlled trial. *American Journal of Kidney Diseases*, 2013, *61*(6), 957-965.

55. Zhang M I N, Willison J H M. Electrical impedance analysis in plant tissues: the effect of freeze-thaw injury on the electrical properties of potato tuber and carrot root tissues. Canadian Journal of Plant Science, 1992, 72(2): 545-553.

56. Ravicz M E, Merchant S N, Rosowski J J. Effect of freezing and thawing on stapes-cochlear input impedance in human temporal bones. Hearing research, 2000, 150(1-2): 215-224.

57. Van Loan M D, Kopp L E, King J C, et al.Fluid changes during pregnancy: use of bioimpedance spectroscopy. Journal of Applied Physiology,1995, 78(3): 1037-1042.

58. Passauer, J., Petrov, H., Schleser, A., Leicht, J., & Pucalka, K. Evaluation of clinical dry weight assessment in haemodialysis patients using bioimpedance spectroscopy: a cross-sectional study. *Nephrology Dialysis Transplantation*, 2009, *25*(2), 545-551.

59. Gibson, A. L., Holmes, J. C., Desautels, R. L., Edmonds, L. B., & Nuudi, L. Ability of new octapolar bioimpedance spectroscopy analyzers to predict 4-component–model percentage body fat in Hispanic, black, and white adults. *The American journal of clinical nutrition*, 2008, *87*(2), 332-338.

60. Fisch, B. J., & Spiegel, D. M. Assessment of excess fluid distribution in chronic hemodialysis patients using bioimpedance spectroscopy. *Kidney international*, 1996, *49*(4), 1105-1109.

61. Scharfetter, H., Monif, M., László, Z., Lambauer, T., Hutten, H., & Hinghofer-Szalkay, H. Effect of postural changes on the reliability of volume estimations from bioimpedance spectroscopy data. *Kidney international*, 1997, *51*(4), 1078-1087.

62. Cox-Reijven, P. L., Kooman, J. P., Soeters, P. B., van der Sande, F. M., & Leunissen, K. M. Role of bioimpedance spectroscopy in assessment of body water compartments in hemodialysis patients. *American journal of*

kidney diseases, 2001, *38*(4), 832-838.

63. Kaysen, G. A., Zhu, F., Sarkar, S., Heymsfield, S. B., Wong, J., Kaitwatcharachai, C., ... & Levin, N. W. Estimation of total-body and limb muscle mass in hemodialysis patients by using multifrequency bioimpedance spectroscopy. *The American journal of clinical nutrition*, 2005, *82*(5), 988-995.

64. York, S. L., Ward, L. C., Czerniec, S., Lee, M. J., Refshauge, K. M., & Kilbreath, S. L. Single frequency versus bioimpedance spectroscopy for the assessment of lymphedema. *Breast cancer research and treatment*,2009, *117*(1), 177.

65. Ando, Y., Mizutani, K., & Wakatsuki, N..Effect of blanching and freeze-thaw treatment on the drying rate and electrical impedance characteristics of carrots. *International Proceedings of Chemical, Biological & Environmental Engineering (IPCBEE), Food Engineering and Biotechnology IV*, 2013, 39-44.

66. Banach, J. K., & Żywica, R.The effect of electrical stimulation and freezing on electrical conductivity of beef trimmed at various times after slaughter. *Journal of food engineering*, 2010, *100*(1), 119-124.

67. Raicu V, Raicu G, Turcu G. Dielectric properties of yeast cells as simulated by the two-shell model. Biochimica et Biophysica Acta (BBA)-Bioenergetics, 1996, 1274(3): 143-148.

68. Zhao K. Some methods of dielectric study on small biological cells. Shengwu Wuli Xuebao, 1999, 16(1): 176-182.

69. Takashima S, Asami K, Takahashi Y. Frequency domain studies of impedance characteristics of biological cells using micropipet technique. I. Erythrocyte. Biophysical journal, 1988, 54(6): 995.

70. Harris C M, Kell D B. The radio-frequency dielectric properties of yeast cells measured with a rapid, automated, frequency-domain dielectric spectrometer. Journal of electroanalytical chemistry and interfacial electrochemistry, 1983, 156: 15-28.

71. Gnecchi J A G. Voltage Controlled Current Source (VCCS) for Electrical Impedance Tomography (EIT) Measurements in the alpha and beta Dispersion Frequency Ranges//Electronics, Robotics and Automotive Mechanics Conference (CERMA), 2010. IEEE, 2010: 677-681.

72. Fricke H. The electric capacity of suspensions with special reference to blood. The Journal of general physiology, 1925, 9(2): 137-152.

73. Fuentes, A., Masot, R., Fernández-Segovia, I., Ruiz-Rico, M., Alcañiz, M., & Barat, J. M.Differentiation between fresh and frozen-thawed sea bream (Sparus aurata) using impedance spectroscopy techniques. *Innovative Food Science & Emerging Technologies*,2013, *19*, 210-217.

74. Vidaček S, Janči T, Brdek Z, et al. Differencing sea bass (Dicentrarchus labrax) fillets frozen in different conditions by impedance measurements. International journal of food science & technology, 2012, 47(8): 1757-1764.

75. Crombie C, Gow N A R, Gooday G W.Influence of applied electrical fields on yeast and hyphal growth of Candida albicans. Microbiology, 1990,136(2): 311-317.

76. Kerner T E, Paulsen K D, Hartov A, et al. Electrical impedance spectroscopy of the breast: clinical imaging results in 26 subjects. IEEE transactions on medical imaging, 2002, 21(6): 638-645.

77. Zou Y, Guo Z. A review of electrical impedance techniques for breast cancer detection. Medical engineering & physics, 2003, 25(2): 79-90.

78. Czerniec, S. A., Ward, L. C., Lee, M. J., Refshauge, K. M., Beith, J., & Kilbreath, S. L. Segmental measurement of breast cancer-related arm lymphoedema using perometry and bioimpedance spectroscopy. *Supportive Care in Cancer*, 2011,*19*(5), 703-710.

79. Wu, L., Ogawa, Y., & Tagawa, A.Electrical impedance spectroscopy analysis of eggplant pulp and effects of drying and freezing–thawing treatments on its impedance characteristics. *Journal of Food Engineering*, 2008, *87*(2), 274-280.

80. Zhang L, Shen H, Luo Y. Study on the electric conduction properties of fresh and frozen–thawed grass carp (Ctenopharyngodon idellus) and tilapia (Oreochromis niloticus). International journal of food science & technology, 2010, 45(12): 2560-2564.

81. Dev S R S, Gariepy Y, Raghavan G S V. Measurement of dielectric properties and finite element simulation of microwave pretreatment for convective drying of grapes. Piers Online, 2009, 5(7): 690-695.

82. Chen, T. H., Zhu, Y. P., Han, M. Y., Wang, P., Wei, R., Xu, X. L., & Zhou, G. H.,2017. Classification of chicken muscle with different freeze–thaw cycles

using impedance and physicochemical properties. *Journal of food engineering*, *196*, 94-100.

83. Huang Y, Holzel R, Pethig R, et al. Differences in the AC electrodynamics of viable and non-viable yeast cells determined through combined dielectrophoresis and electrorotation studies. Physics in medicine and biology, 1992, 37(7): 1499.

84. Wakamatsu H. A dielectric spectrometer for liquid using the electromagnetic induction method. Hewlett Packard Journal, 1997, 48: 37-44.

85. Griffiths H. Magnetic Induction Tomography Electrical Impedance Tomography: Methods, History and Applications ed DS Holder. 2005.

86. Onik G, Cooper C, Goldberg H I, et al. Ultrasonic characteristics of frozen liver. Cryobiology, 1984, 21(3): 321-328.

87. Li W, Wang P, Chen T, et al. Classification of chicken breasts with different freezing-thawing cycles by impedance properties and artificial neural networks. Transactions of the Chinese Society of Agricultural Engineering, 2014, 30(7): 250-257.

88. Fernández-Segovia I, Fuentes A, Aliño M, et al. Detection of frozen-thawed salmon (Salmo salar) by a rapid low-cost method. Journal of Food Engineering, 2012, 113(2): 210-216.

89. OHNISHI S, SHIMIYA Y, KUMAGAI H, et al. Effect of freezing on electrical and rheological properties of food materials. Food science and technology research, 2007, 10(4): 453-459.

90. Mejdoubi A, Brosseau C，“Finite-element simulation of the depolarization factor of arbitrarily shaped inclusions，” Physical Review E, 2006,74(3): 031405.

91. Schwan, Herman P,"Electrical properties of tissues and cell suspensions: mechanisms and models." Proceedings of 16th Annual International Conference of the IEEE Engineering in Medicine and Biology Society,1994, Vol. 1. IEEE.

92. Schwan, Herman P, “Electrical properties of tissue and cell suspensions,” Advances in biological and medical physics,1957, Vol. 5. Elsevier: 147-209.